

UC Irvine

UC Irvine Electronic Theses and Dissertations

Title

Multidimensional spectroscopy of molecular polaritons

Permalink

<https://escholarship.org/uc/item/4rd0642q>

Author

Saurabh, Prasoon

Publication Date

2017

Peer reviewed|Thesis/dissertation

UNIVERSITY OF CALIFORNIA,
IRVINE

Multidimensional Spectroscopy of Molecular Polaritons

DISSERTATION

submitted in partial satisfaction of the requirements
for the degree of

DOCTOR OF PHILOSOPHY

in Chemistry

by

Prasoon Saurabh

Dissertation Committee:
Professor Shaul Mukamel, Chair
Professor Craig Martens
Associate Professor Eric Potma

2017

DEDICATION

To Pitaji, Ma, Didi, Prasanna, Prama and RG

TABLE OF CONTENTS

	Page
LIST OF FIGURES	v
LIST OF TABLES	vi
ACKNOWLEDGMENTS	vii
CURRICULUM VITAE	viii
ABSTRACT OF THE DISSERTATION	ix
1 Introduction	1
1.1 Background	3
1.1.1 Survey of spectroscopic signals for exciton-oscillator model	4
1.1.2 Optical Cavity	8
1.1.3 Light Harvesting Complex II	11
1.2 Outline	12
2 Quasiparticle representation of multidimensional signal	13
2.1 Model Hamiltonian	15
2.2 Coherent Nonlinear Polariton Equations	20
2.3 Response functions in terms of polariton Green's function	24
2.4 Polariton-Polariton scattering matrix	25
2.5 Third order response functions for polaritons	29
2.5.1 Time domain	29
2.5.2 Frequency domain	30
2.5.3 Heterodyne detected signals	32
2.6 Discussion and Conclusion	33
3 Molecular vibrational polaritons	36
3.1 Introduction	36
3.2 Vibrational polaritons and their DQC signal	38
3.3 A Single vibrational mode coupled to single cavity mode	40
3.4 Polaritons for two vibrational modes and their DQC signal	43
3.5 Conclusions	44

4	Interacting Deformed Molecular Polaritons	52
4.1	Introduction	52
4.2	Interacting deformed molecular polaritons	54
4.3	Effects due to deformations of molecular polaritons	61
4.3.1	Signal Enhancement	62
4.3.2	Effective Enhancement	64
4.3.3	Polariton-Polariton Scatterings	65
4.4	Concluding Remarks	68
5	Concluding Remarks	78
	Bibliography	80
A	Supplementary for Chapter 3	92
A.1	Multimode Molecular Vibration Hamiltonian	92
A.1.1	The molecular vibrational single-polariton (MVP) and double-polariton (MVBP) manifolds:	94
A.1.2	The DQC signal for molecular vibrational polaritons	95
A.2	Nomenclature	96
A.3	Absorptive and dispersive parts of DQC	96
A.3.1	Amide-I vibrations of NMA in IR cavity	96
A.4	Amide-I+II of NMA in IR cavity	100
A.5	Peak splitting for Amide-I vibrations of NMA in optical cavity	102
A.6	Peak splitting for Amide-I+II vibrations of NMA in optical cavity	102
B	Supplementary to Chapter 4	104
B.1	Introduction	104
B.1.1	Modification on energy terms dues to q	106
B.2	Useful relations for q -deformed algebras	108
B.3	Thermal distribution of q -deformed polaritons	112

LIST OF FIGURES

	Page	
1.1	The scaled energies of upper (UP, red solid line) and lower (LP, blue solid line) polaritons as a function of ω_n/ω_c where ω_n is molecular energy and ω_c is cavity energy (both black dashed lines) for a single molecule in single mode optical cavity. The ratio is equivalent to changing effective cavity coupling g . The closest gap between the UP and LP at avoided crossing gives the measure of rabi splitting $\sim 2g$	8
1.2	Schematic to illustrate possible experimental setup to measure nonlinear optical signals discussed in this thesis. The optical cavity with mirrors $\lambda/2$ distance apart can allow for strong coupling to the molecular vibrational and electronic degrees of freedom. Molecular aggregate with dephasing γ is placed in single mode optical cavity with photon is confined along \mathbf{k}_z^c . κ is cavity dephasing. $\mathbf{k}_i : i \in \{1, 2, 3, s\}$ are three incoming external field wave vectors and signal mode respectively. $t_i : i \in \{1, 2, 3, s\}$ is as described in text and assumed in Eqn. (1.7).	10
2.1	Coherent polariton dynamics represented by Feynmann diagrams (a) for \mathbf{k}_{III} c.f.Eqn. (2.53), (b) for \mathbf{k}_{II} c.f. Eqn. (2.52) and (c) for \mathbf{k}_I c.f. Eqn. (2.51) . . .	29
3.1	Amide-I ($C = O$ symmetric stretch) and Amide-II (CN symmetric stretch + NH bend) vibrations are represented using double sided arrow for $N - Methylacetamide$ in (a). Eigen-energies of Amide-I and coupled Amide-I and Amide-II motifs in local basis and polariton basis (see Sec.SI of supplementary information A.1 for detail) are given in (b) and (c) respectively. (d) schemes the FWM experiment, the yellow sample is the DBR Fabry-Perot cavity coupled to molecular vibrations (see text for detail) and, (e) shows the relevant ladder diagrams contributing to double quantum coherence (DQC) technique.	39
3.2	(a) Absolute value of DQC signal (Eq. A.8) for Amide-I vibrations of NMA, as we vary coupling strength (g) from no (green plane), weak (blue planes) and strong (red planes) coupling regimes. (b) Schematic representation of DQC signal (zoomed in the grey square at $g = 0cm^{-1}$) with all possible peaks identified as intersections of different lines. (c) Same result but for strong coupling and the last panel. The lines are: i) Ω_{fe} labelled as $f_i e_j$ (dashed blue lines), ii) Ω_{eg} labelled as e_j (black solid lines), iii) Ω_{fg} labelled as f_i and appropriate anharmonicities (Δ_{ij} in local basis or \tilde{V}_{ii} in polariton basis) respectively. We wish to spectrally resolve (b) to (c).	47

- 3.3 DQC signals for Amide-I vibrations in NMA using Eq. A.8 and ladder diagrams (Fig. 3.1e): (a) $|\mathcal{S}_i(\Omega_3, \Omega_2, 0)|$ with resonance at $\Omega_{eg} = 1625cm^{-1}$, (b) $|\mathcal{S}_{ii}(\Omega_3, \Omega_2, 0)|$ with resonance at $\Omega_{fe} = 1617cm^{-1}$ and (c) $|\mathcal{S}(\Omega_3, \Omega_2, 0)|$ with resonances at $\Omega_{eg} = 1625cm^{-1}$ and $\Omega_{fe} = 1617cm^{-1}$. The linear projections along each axis is shown in green. For simplicity, cavity field vector \mathbf{e}_c is assumed to be mostly parallel to molecular vibrational transition dipole μ_m . Amide-I vibrations (ω_1) is resonant to cavity cutoff frequency $\omega_0 = 1625cm^{-1}$. The anharmonicity are assumed $\Delta_{11} = 15cm^{-1}$ (Table 3.1). 48
- 3.4 DQC signals using Eq. A.8 and ladder diagrams (Fig. 3.2b): *Columns* (left-) $|\mathcal{S}_i(\Omega_3, \Omega_2, 0)|$ with resonance at Ω_{e1g} and Ω_{e2g} ; (middle-) $|\mathcal{S}_{ii}(\Omega_3, \Omega_2, 0)|$ with resonance at $\Omega_{f2,e2}, \Omega_{f2,e1}, \Omega_{f1,e2}, \Omega_{f3,e2}, \Omega_{f1,e1}, \Omega_{f3,e1}$; and (right-) $|\mathcal{S}(\Omega_3, \Omega_2, 0)|$ with respective resonances for Amide-I vibrations in NMA with cavity coupling *rows* : (a) $20cm^{-1}$ and (a) $50cm^{-1}$. The linear projections along each axis is shown in green. For simplicity, cavity field vector \mathbf{e}_c is assumed to be mostly parallel to molecular vibrational transition dipole μ_m . Amide-I vibrations (ω_1) is resonant to cavity cutoff frequency $\omega_0 = 1625cm^{-1}$. The anharmonicity are assumed $\Delta_{11} = 15cm^{-1}$ (Table 3.1) 49
- 3.5 Modulus of DQC signal for Amide-I+II vibrations in NMA with varying cavity coupling ($0cm^{-1} \rightarrow 60cm^{-1}$). Cavity field vector \mathbf{e}_c is assumed to be mostly parallel to molecular vibrational transition dipole μ_m . Amide-I vibrations (ω_1) is resonant to cavity cutoff frequency $\omega_0 = 1625cm^{-1}$ and $\omega_2 = 1540cm^{-1}$. The anharmonicities $\Delta_{11} = 15cm^{-1}$ and $\Delta_{22} = 11cm^{-1}$ (Table 3.1). 50
- 3.6 DQC signals for Amide-I+II vibrations in NMA using Eq. A.8 and ladder diagrams (Fig. 3.1e): *Columns* : (left-) $|\mathcal{S}_i(\Omega_3, \Omega_2, 0)|$ with resonance at $\Omega_{e1g}, \Omega_{e2g}$ and Ω_{e3g} ; (middle-) $|\mathcal{S}_{ii}(\Omega_3, \Omega_2, 0)|$ with resonance at $\Omega_{f1e3} \approx \Omega_{f1e2}, \Omega_{f3e4} \approx \Omega_{f4e2}, \Omega_{f2e3} \approx \Omega_{f2e2}, \Omega_{f1e1}, \Omega_{f3e3} \approx \Omega_{f3e2} = \Omega_{f4e1} = \Omega_{f6e3}, \Omega_{f6e2}, \Omega_{f5e3}, \Omega_{f2e1}, \Omega_{f5e2}, \Omega_{f3e1}, \Omega_{f6e1}, \Omega_{f5e1}$ and (right-) $|\mathcal{S}(\Omega_3, \Omega_2, 0)|$ with respective resonances and cavity couplings (*rows*) (a) $0cm^{-1}$, (b) $10cm^{-1}$, and (c) $60cm^{-1}$ along Ω_3 , while peaks at $\Omega_{f1g}, \Omega_{f2g}, \Omega_{f3g}, \Omega_{f4g}, \Omega_{f5g}$ and Ω_{f6g} along Ω_2 . The linear projections along each axis is shown in green. For simplicity, cavity field vector \mathbf{e}_c is assumed to be mostly parallel to molecular vibrational transition dipole μ_m . Amide-I vibrations (ω_1) is resonant to cavity cutoff frequency $\omega_0 = 1625cm^{-1}$ and $\omega_2 = 1540cm^{-1}$. The anharmonicities are assumed $\Delta_{11} = 15cm^{-1}$ and $\Delta_{22} = 11cm^{-1}$ (Table 3.1) 51
- 4.1 Typical double quantum coherence (DQC) using Eqn. (4.11) using parameters in Table 4.1 for light harvesting complex II (LHC-II) for coupling strength of $10cm^{-1}$ 60
- 4.2 Average deformation $\bar{q} = \frac{\sum q_i}{N_p}$ as function of κ and cavity coupling strength g for various polariton numbers N_p : a) $N_p = 2$; b) $N_p = 8$; and c) $N_p = 15$. The expression for q_i is calculated using Eqn. (4.9) and $\lambda_i = q_i$. The dashed black lines are at $\kappa = \sqrt{2}$ where $N_p \bar{q} \sim 1$. and Eqn.(4.1) to Eqn.(4.2) apart from factor of 2. Dashed red lines show possible values of κ where more interesting structural information can be extracted for varying coupling strengths. . . . 71

4.3	Signal enhancements, \mathcal{Q} (using Eqn. (4.14)) for DQC for $\kappa = 0.9$ for varying cavity coupling strength g vs increasing chromophore number in optical cavity is showed for a) Left: Lower Polariton Branch (LPB), b) Middle Polariton Branch (MPB) and c) Upper Polariton Branch (HPB) is done. (see text for details)	72
4.4	Effective signal enhancement $c\mathcal{Q}$ (using Eqn. (4.15)) for DQC for $\kappa = 0.9$ for varying cavity coupling strength g vs increasing chromophore number in optical cavity is showed for Top Row: Lower Polariton Branch (LPB, Left), b) Upper Polariton Branch (UPB, Middle) and c) Middle Polariton Branch (MPB, Right); Bottom Row: Middle Polariton Branch (MPB1, Left), and $\text{Log}(c\mathcal{Q}_{MP1} - c\mathcal{Q}_{MP1})$ are done. (see text for details)	73
4.5	Polariton-Polariton interactions varying number of chromophore using Eqn.(4.10). Top Row (for $\kappa = \sqrt{2}, q = 1$) a) $N_p=5$,b) $N_p=9$,a) $N_p=15$; Bottom Row (for $\kappa = 0.9, q \neq 1$) a) $N_p=5$,b) $N_p=9$,a) $N_p=15$ at $g = 0\text{cm}^{-1}$. See text for details.	74
4.6	Polariton-Polariton interactions varying number of chromophore using Eqn.(4.10). Top Row (for $\kappa = \sqrt{2}, q = 1$) a) $N_p=5$,b) $N_p=9$,a) $N_p=15$; Bottom Row (for $\kappa = 0.9, q \neq 1$) a) $N_p=5$,b) $N_p=9$,a) $N_p=15$ at $g = 150\text{cm}^{-1}$. See text for details.	75
4.7	Polariton-Polariton scattering $\Gamma(\omega)$ at typical chromophore bipolariton eigenenergy (Chlb) $\omega = 30000\text{cm}^{-1}$ for varying number of chromophore using Eqn.(4.13). Top Row (for $\kappa = \sqrt{2}, q = 1$) a) $N_p=5$,b) $N_p=9$,a) $N_p=15$; Bottom Row (for $\kappa = 0.9, q \neq 1$) a) $N_p=5$,b) $N_p=9$,a) $N_p=15$ at $g = 0\text{cm}^{-1}$. See text for details.	76
4.8	Polariton-Polariton scattering $\Gamma(\omega)$ at typical chromophore bipolariton eigenenergy (Chlb) for $\omega = 30000\text{cm}^{-1}$ for varying number of chromophore using Eqn.(4.13). Top Row (for $\kappa = \sqrt{2}, q = 1$) a) $N_p=5$,b) $N_p=9$,a) $N_p=15$; Bottom Row (for $\kappa = 0.9, q \neq 1$) a) $N_p=5$,b) $N_p=9$,a) $N_p=15$ at $g = 0\text{cm}^{-1}$. See text for details.	77
A.1	Imaginary part of DQC signals for Amide-I vibrations in NMA using Eq. A.8 and ladder diagrams (Fig. 3.2b): (a) $ \mathcal{S}_i(\Omega_3, \Omega_2, 0) $ with resonance at $\Omega_{eg} = 1625\text{cm}^{-1}$, (b) $ \mathcal{S}_{ii}(\Omega_3, \Omega_2, 0) $ with resonance at $\Omega_{fe} = 1617\text{cm}^{-1}$ and (c) $ \mathcal{S}(\Omega_3, \Omega_2, 0) $ with resonances at $\Omega_{eg} = 1625\text{cm}^{-1}$ and $\Omega_{fe} = 1617\text{cm}^{-1}$. The linear projections along each axis is shown in green. For simplicity, cavity field vector \mathbf{e}_c is assumed to be mostly parallel to molecular vibrational transition dipole μ_m . Amide-I vibrations (ω_1) is resonant to cavity cutoff frequency $\omega_0 = 1625\text{cm}^{-1}$. The anharmonicity are assumed $\Delta_{11} = 15\text{cm}^{-1}$ (Table 3.1).	96
A.4	Real part DQC signals using Eqn. A.8 and ladder diagrams (Fig. 3.2b): <i>Columns</i> (left-) $ \mathcal{S}_i(\Omega_3, \Omega_2, 0) $ with resonance at Ω_{e1g} and Ω_{e2g} ; (middle-) $ \mathcal{S}_{ii}(\Omega_3, \Omega_2, 0) $ with resonance at $\Omega_{f2,e2}, \Omega_{f2,e1}, \Omega_{f1,e2}, \Omega_{f3,e2}, \Omega_{f1,e1}, \Omega_{f3,e1}$; and (right-) $ \mathcal{S}(\Omega_3, \Omega_2, 0) $ with respective resonances for Amide-I vibrations in NMA with cavity coupling <i>rows</i> : (a) 20cm^{-1} . The linear projections along each axis is shown in green. For simplicity, cavity field vector \mathbf{e}_c is assumed to be mostly parallel to molecular vibrational transition dipole μ_k . Amide-I vibrations (ω_1) is resonant to cavity cutoff frequency $\omega_0 = 1625\text{cm}^{-1}$. The anharmonicity are assumed $\Delta_{11} = 16\text{cm}^{-1}$ (Table 3.1))	97

- A.9 Imaginary part of DQC signals using Eqn. A.8 and ladder diagrams (Fig. 1e in maintext):(a) $\mathcal{S}_i(\Omega_3, \Omega_2, 0)$ with resonance at $\Omega_{e_{1g}}, \Omega_{e_{2g}}$ and $\Omega_{e_{3g}}$ (b) $\mathcal{S}_{ii}(\Omega_3, \Omega_2, 0)$ with resonance at $\Omega_{f_{1e_3}} \approx \Omega_{f_{1e_2}}, \Omega_{f_{3e_4}} \approx \Omega_{f_{4e_2}}, \Omega_{f_{2e_3}} \approx \Omega_{f_{2e_2}}, \Omega_{f_{1e_1}}, \Omega_{f_{3e_3}} \approx \Omega_{f_{3e_2}} = \Omega_{f_{4e_1}} = \Omega_{f_{6e_3}}, \Omega_{f_{6e_2}}, \Omega_{f_{5e_3}}, \Omega_{f_{2e_1}}, \Omega_{f_{5e_2}}, \Omega_{f_{3e_1}}, \Omega_{f_{6e_1}}, \Omega_{f_{5e_1}}$ and (c) $\mathcal{S}_i(\Omega_3, \Omega_2, 0)$ with respective resonances for Amide-I+II vibrations in NMA with cavity coupling $20cm^{-1}$ along Ω_3 , while peaks at $\Omega_{f_{1g}}, \Omega_{f_{2g}}, \Omega_{f_{3g}}, \Omega_{f_{4g}}, \Omega_{f_{5g}} = \Omega_{f_{6g}}$ along Ω_2 in (a)-(c). The linear projections along each axis is shown in green. For simplicity, cavity field vector \mathbf{e}_c is assumed to be mostly parallel to molecular vibrational transition dipole μ_k . Amide-I vibrations (ω_1) is resonant to cavity cutoff frequency $\omega_0 = 1625cm^{-1}$ and $\omega_2 = 1510cm^{-1}$. The anharmonicity are assumed $\Delta_{11} = 16cm^{-1}$ and $\Delta_{22} = 24cm^{-1}$ (Table 3.1). 100
- A.10 Real part of DQC signals using Eqn. A.8 and ladder diagrams (Fig. 3.2b):(a) $\mathcal{S}_i(\Omega_3, \Omega_2, 0)$ with resonance at $\Omega_{e_{1g}}, \Omega_{e_{2g}}$ and $\Omega_{e_{3g}}$ (b) $\mathcal{S}_{ii}(\Omega_3, \Omega_2, 0)$ with resonance at $\Omega_{f_{1e_3}} \approx \Omega_{f_{1e_2}}, \Omega_{f_{3e_4}} \approx \Omega_{f_{4e_2}}, \Omega_{f_{2e_3}} \approx \Omega_{f_{2e_2}}, \Omega_{f_{1e_1}}, \Omega_{f_{3e_3}} \approx \Omega_{f_{3e_2}} = \Omega_{f_{4e_1}} = \Omega_{f_{6e_3}}, \Omega_{f_{6e_2}}, \Omega_{f_{5e_3}}, \Omega_{f_{2e_1}}, \Omega_{f_{5e_2}}, \Omega_{f_{3e_1}}, \Omega_{f_{6e_1}}, \Omega_{f_{5e_1}}$ and (c) $\mathcal{S}_i(\Omega_3, \Omega_2, 0)$ with respective resonances for Amide-I+II vibrations in NMA with cavity coupling $20cm^{-1}$ along Ω_3 , while peaks at $\Omega_{f_{1g}}, \Omega_{f_{2g}}, \Omega_{f_{3g}}, \Omega_{f_{4g}}, \Omega_{f_{5g}} = \Omega_{f_{6g}}$ along Ω_2 in (a)-(c). The linear projections along each axis is shown in green. For simplicity, cavity field vector \mathbf{e}_c is assumed to be mostly parallel to molecular vibrational transition dipole μ_k . Amide-I vibrations (ω_1) is resonant to cavity cutoff frequency $\omega_0 = 1625cm^{-1}$ and $\omega_2 = 1510cm^{-1}$. The anharmonicity are assumed $\Delta_{11} = 16cm^{-1}$ and $\Delta_{22} = 24cm^{-1}$ (Table 3.1). 101
- A.11 Rabi splitting for nearest peaks in Fig. A.1-A.5. The nomenclature used is as follows, $\delta_1 = \omega_{f_{2e_2}} - \omega_{f_{1e_1}}, \delta_2 = \omega_{f_{2e_2}} - \omega_{f_{1e_1}}, \delta_1 = \omega_{f_{2e_2}} - \omega_{f_{1e_1}}, \delta_1 = \omega_{f_{2e_2}} - \omega_{f_{1e_1}}$ and $\delta_1 = \omega_{f_{2e_2}} - \omega_{f_{1e_1}}$ 102
- A.12 Rabi splitting for nearest peaks for Amide-I+II of NMA in single mode cavity corresponding to Fig. A.7-A.9. 102

LIST OF TABLES

	Page
3.1 Parameters used in this work. ω_0 is cavity cut-off frequency. $\omega_{1,2}$ are vibrational exciton (1,2) (<i>Amide - I</i> , <i>Amide - II</i>) energies, $\gamma_{1,2}$ are their respective dephasing rates, J_{ij} is harmonic scalar coupling, and Δ_{ij} are exciton-exciton interaction energies.	41
4.1 Parameters used in this paper. $\epsilon_n^{(0)}$ energies of n isolated chromophore from Light Harvesting Complex (LHCII), μ_a and μ_b are transition dipole moments for Chlorophyll a (Chla) and b (Chlb) respectively. $\epsilon_{ord}^{(0)}$ provides the ordering of energies [1].	61

ACKNOWLEDGMENTS

I would like to thank my advisor, Prof. Shaul Mukamel for introducing me to a beautiful and systematic way of understanding of physical reality. It has been a privilege to learn under his tutelage. I would also like to thank the rest of my committee members, Professors Craig Martens and Eric Potma, for the very valuable encouragements and their valuable time.

For this thesis, I would like to extend my acknowledgement to incredibly hard working and great scientists and friends I have gotten chance to know while working in the Mukamel group: Dr. Konstantin Dorfman, Dr. Kochise Bennet, Dr. Markus Kowalewski, Dr. Jeremy Rouxel, Dr. Zhedong Zhang, Dr. Daeheum Cho, Dr. Benjamin Fingerhut, Dr. Daniel Healion, Dr. Yu Zhang, Dr. Konstantin Dorfman, Dr. Weijie Hua, Dr. Frank Schlawin, Dr. Bijay Aggrawalla, Dr. Arunagshu Debnath, Dr. Swapna Lekkala, Dr. Jason Biggs, and Dr. Hideo Ando.

I would also like to thank all my friends, I have made over years, who have been pivotal in my time at UC-Irvine. Finally, my sincerest of thanks to my parents, my siblings and friends for their everlasting love and support without which none of this would be possible.

I would also gratefully acknowledge the support of National Science Foundation (Grants No. CHE-1361516 and CHE-1111350) and the Chemical Sciences, Geosciences and Biosciences Division, Office of Basic Energy Sciences, Office of Science, U.S. Department of Energy.

Chapters 3 and appendix A adapted with permission from *J. Chem. Phys.* **144**(12), 124115.
© 2015 American Institute of Physics

CURRICULUM VITAE

Prasoon Saurabh

EDUCATION

Doctor of Philosophy in Chemistry University of California- <i>Irvine</i>	2017 <i>Irvine, CA</i>
Master in Chemistry University of California- <i>Irvine</i>	2017 <i>Irvine, CA</i>
Bachelor of Science in Math Budapest University of Technology and Economics (BME) Ripon College	2010 <i>Budapest, Hungary</i> <i>Ripon, Wisconsin</i>
Bachelor of Science in Physics Ripon College	2011 <i>Ripon, Wisconsin</i>
Bachelor of Science in Chemistry Ripon College	2011 <i>Ripon, Wisconsin</i>

RESEARCH EXPERIENCE

Graduate Research Assistant University of California- <i>Irvine</i>	2013–2017 <i>Irvine, CA</i>
---	---------------------------------------

TEACHING EXPERIENCE

Teaching Assistant-General Chemistry Labs University of California- <i>Irvine</i>	Summer 2013 – 2017 <i>Irvine, CA</i>
Teaching Assistant-Graduate Molecular Spectroscopy University of California- <i>Irvine</i>	Spring 2014–2017 <i>Irvine, CA</i>
Teaching Assistant-Graduate Applications of Quantum Mechanics University of California- <i>Irvine</i>	Winter 2015–2017 <i>Irvine, CA</i>
Teaching Assistant-Upper Div. Undergraduate Physical Chemistry University of California- <i>Irvine</i>	2012–2016 <i>Irvine, CA</i>

ABSTRACT OF THE DISSERTATION

Multidimensional Spectroscopy of Molecular Polaritons

By

Prasoon Saurabh

Doctor of Philosophy in Chemistry

University of California, Irvine, 2017

Professor Shaul Mukamel, Chair

Molecular polaritons, dressed light-molecular exciton quasiparticles, have different optical properties compared to excitons. Over the past few decades there has been extensive theoretical understanding and experimental demonstration on how the physical and chemical behaviour of exciton are modified in confined optical cavity. Qualitative and quantitative understanding of nonlinear polariton interactions are at the heart of open questions in the field. These nonlinearities manifests themselves as polariton-polaritons scattering matrices in the lowest order.

Nonlinear spectroscopic techniques, like double quantum coherence (DQC), can be used to study these nonlinearities such as vibrational anharmonicities, on-site interactions etc. A quasiparticle representation of coherent multidimensional optical signals for molecular polaritons in confined cavity (in both time and frequency domain) is developed allowing for direct observations of these polariton-polariton scattering terms that are explicitly present in the nonlinear signals.

In spirit of understanding anharmonicities, sum over state (SOS) method is employed to study modification of vibrational structure of ground electronic states for Amide-I and II motifs of N-methylacetamide due to varying cavity coupling strengths is done. Again, DQC signals are studied for illustrations.

Coherent pumping of molecular polaritons introduces several complications in extracting full structural information due to loss of strong coupling, non-equilibrium thermal excitations, phase-space filling factors (causing the polaritons to deviate from usual bosonic nature) and deviations from Hopfield coefficients, to name a few. Compelling remedies to the last two difficulties is proposed using theoretical framework to redefine the interacting polariton problem into a interacting deformed polaritons form. Discrepancies due to both phase-filling factors and deviations from Hopfield coefficients are encoded in a single deformation parameter q .

A modified DQC is derived and an unique measure for effective enhancement of this signal is presented as a function of number of polaritons. This is used to investigate collective effects due to polariton-polariton scattering. Applications are made for varying number of chromophores (for $N_p \in \{1, 2, \dots, 15\}$) picked from a monomer of Light Harvesting Complex II (LHCII). It is shown that polariton-polariton scattering for non-bosonic polaritons could bring the middle polariton branches (MPBs), which are usually embedded deep within the so called "dark-state", to light.

Chapter 1

Introduction

*“If I could remember name of the particles, I
would be a botanist.”*

—Ernico Fermi

Much of the observable universe, from quarks to cosmos, is understood by carefully analyzing the interactions that govern the constituent particles. One of the most fundamental and physically intuitive ways to interpret observable realities is to study them via “light-matter” interactions. This is the core essence of spectroscopy. In other words, it is the study of matter by its interactions with light in order to know their physical and chemical structure. Of course, linear interactions within matter operators (e.g., terms like $a^\dagger a$) that enters in a typical material Hamiltonian $\sum_i \omega_i a_i^\dagger a_i + \sum'_{i,j} J_{ij} a_i^\dagger a_j$, where ω_i is material frequencies, and J_{ij} is a linear coupling constant, can be extracted by linear spectroscopic techniques such as absorption, emission etc. Any nonlinearity in the material Hamiltonian manifests itself as anharmonicities dictating a plethora of physical properties, from classically motivated thermal expansion [2] to thermalization of Bose-Einstein Condensates (BEC) [3]. And, to chemical physics, eg., by changing molecular electronic and vibrational structures thus controlling the chemical reactions [4, 5]. This necessitates the development of nonlinear

optical spectroscopic techniques as has been excellently done in Ref. [6]. The purpose of the thesis is to extend one of the representations, namely the quasiparticle representation in Ref. [6] (c.f. Sec. 1.1.1 for basic definitions), and to study multidimensional signals of molecules and molecular aggregates confined in optical cavities (c.f. Sec 1.1.2 for survey on optical cavities).

Quasiparticles, a conceptual construction, provides physically intuitive understanding of several collective many-body interactions, for instance, Landau used it to describe superfluid *He* [7]. Bound electron-hole pairs form excitons and are often used to describe molecular excitations. These excitons with localized wavefunctions (*Frenkel* type) has been wildly used to describe molecular Hamiltonian for molecular aggregates [8]. When coupled to a photon in optical cavities they form dressed states called *molecular polariton* which sets the basis for the system hamiltonian under investigation in multidimensional spectroscopy [9].

In the next section (Sec. 1.1), we present the background which includes a short survey on the exciton oscillator model typically used to study large macromolecules and give the definition of the heterodyne detected signal that will be used through out the thesis. The experimental setup for which we wish to develop the theory is presented along with different cavity properties defining different interaction regimes, which is also done in the section. Since most signal calculations done in this thesis use parameters for chromophores (or the whole aggregates) of light harvesting complex II (LHCII) we include a brief discussion on structure and nomenclature of different singly and doubly excited energy bands of LHCII for completeness. We conclude this chapter with an outline of rest of the thesis. (Unless otherwise stated, $\hbar = c = 1$.)

1.1 Background

Spectroscopy is commonly formulated by making the semiclassical approximation by treating the fields classically along with a careful quantum mechanical treatment of matter [10, 11, 12]. The radiation-matter coupling may be described by the minimal coupling Hamiltonian where the electromagnetic fields are represented by vector potential $\mathbf{A}(\mathbf{r}, t)$ [13] and the matter properties enter through the current $\hat{\mathbf{j}}(\mathbf{r}, t)$ and charge density $\hat{\sigma}(\mathbf{r}, t)$ matrix elements of the desired transitions [14]. Alternatively, the multipolar hamiltonian is used where the electromagnetic field is represented by the electric and magnetic fields and matter is expanded in electric and magnetic multipoles. In most applications, including the theory of the laser [11], the lowest order of this multipolar expansion, known as the dipole (long wavelength) approximation is sufficient to account for experimental observations [15].

In recent years, however, there have been rapid developments [16, 17, 18, 19, 20], both theoretical and experimental, in the field of nanooptics [21]. Notable for spectroscopy are, nanoantenna [16], nanoplasmonic [17, 18, 22] and associated spatial and temporal resolutions of optical spectra resulting in attosecond local-field enhanced ($\times 10 - 10^2$) spectroscopy [23, 24, 25, 26, 27]. This is possible because of the nano-scale field confinement ($\sim 10nm$) [16], as in the case of nanoantenne, and the spectral bandwidth of plasmonic spectra (850 – 2200 THz) [17]; and most recently in optical nanocavities [28]. This allows for an interesting venue for strong molecular interactions with confined photons.

Nano-optical fields are spatially confined fields within optical cavities that may show appreciable position (\mathbf{r})- dependence on the molecular length scale [29, 30, 21, 31, 32]. When the field confinement is comparable to quantum confinement of molecular orbitals, the dipole approximation may not be adequate and higher multipoles are required [33, 16]. To our rescue, the $\mathbf{A}^2(\mathbf{r}, t)$ that accompanies the required minimal coupling interaction of photon field with the molecules confined in the optical cavity can be eliminated using generalized the Power-

Zineau-Woolley transformation for arbitrary bounded geometries [34]. Furthermore, under the long wavelength limit, the usual $\mathbf{p}(\mathbf{r}) \cdot \mathbf{A}(\mathbf{r}, t)$ (and $\mathbf{A}(\mathbf{r}, t) \cdot \mathbf{p}(\mathbf{r})$) reduces to $\boldsymbol{\mu}(\mathbf{r}) \cdot \mathbf{E}(\mathbf{r}, t)$. This will be used to define the cavity coupling strength, g (c.f. Sec. 1.1.2), for rest of the thesis following the justification that the single mode (λ or $\lambda/2$) optical cavity for $\lambda \gg a$, where a is the single molecular size is effectively a dipolar interaction. It is still possible to achieve strong coupling at larger $\lambda \propto 1000nm$ if we increase the number of the molecules N as g scales $\sim \sqrt{N}$. This allows for an easier mapping of the quasiparticle representation of nonlinear optical signals to incorporate molecules confined in optical cavities.

1.1.1 Survey of spectroscopic signals for exciton-oscillator model

We start with a simple model that can be used to study the majority of physical systems with electronic transitions in large macromolecules (Light Harvesting Complexes) or vibrational transitions in peptides (like Amide-I and Amide-II motifs) [35, 36]. The model of interest can often be reduced to a system of N interacting chromophores, we restrict ourselves to a three level system, usually labelled as S_0 , S_1 and S_2 with energies relative to the ground electronic state $S_0(\omega_0 = 0)$ denoted as ω_m and ω'_m . The dipole allowed transition are from the ground electronic state S_0 to the first excited state S_1 or from the first excited state S_1 to the doubly excited state S_2 with values denoted by μ_m and μ'_m .

By introducing the exciton-oscillator operator, we set a precedent in developing the quasiparticle representation of multidimensional optical signals for molecular polaritons (c.f. Chapter 2). The exciton creation operator \hat{B}_n for mode n is given by,

$$\hat{B}_n^\dagger := |1\rangle_{nn}\langle 0| + \kappa_n |2\rangle_{nn}\langle 1|, \quad (1.1)$$

where $|i\rangle_n \in \{0, 1, 2\}$ represent the basis for ground, singly and doubly excited states respectively. These exciton operators may deviate from usual bosonic commutation relations due to direct Pauli scattering and also due to the electron-hole exchange tensor [37, 38]. For a three-level system considered in the majority of this thesis, we employ the following commutation relations,

$$[\hat{B}_n, \hat{B}_m^\dagger] = \delta_{mn} \left[1 - \left(2 - \frac{\kappa_n^2}{2} \right) (\hat{B}_m^\dagger)^2 (\hat{B}_m)^2 \right]. \quad (1.2)$$

$\kappa_m (\in \mathbf{R})$ parameterizes the commutation relation [39] and choosing $\kappa_m = \frac{\mu'_m}{\mu_m}$ allows for a simpler relation between the exciton operators and the polarization operator \hat{P} ,

$$\hat{P} = \sum_n \mu_n (\hat{B}_n + \hat{B}_n^\dagger), \quad (1.3)$$

giving a much simpler expression for the Green's function required to calculate the nonlinear responses.

With this, we are now able to write the model hamiltonian for molecular aggregates (used throughout this thesis, unless otherwise stated, in terms of exciton-oscillator operators [39, 8, 40],

$$H_0 = \sum_{mn} \Omega_{mn} \hat{B}_m^\dagger \hat{B}_n + \sum_m \frac{U_m}{2} (\hat{B}_m^\dagger)^2 (\hat{B}_m)^2. \quad (1.4)$$

With nearest neighbor hopping term J_{mn} included in $\Omega_{mn} = \delta_{mn}\omega_m + J_{mn}$ and $U_m = U_{mm,mm} = 2(\omega'_m \kappa^{-2} - \omega_m)$. U_m provides anharmonicities for $\kappa \neq \sqrt{2}$. It should be noted that, the commutation relation (Eqn. 1.2) and model Hamiltonian (Eqn. 1.4) have higher order

polynomials of exciton operators but are inconsequential for multidimensional spectroscopy upto third order. Furthermore, this Hamiltonian allows us to view excitons as oscillator degrees of freedom instead of states. These collective oscillators are quasiparticles that are often used to describe many body phenomenon in systems exhibiting joint electron-holes pair effects and (as already used earlier) are called excitons.

The interaction between the aggregate Hamiltonian H_0 in Eqn. 1.4 with external electric fields is given by,

$$H_{int} = -\mathcal{E}(t) \cdot \hat{P}, \quad (1.5)$$

where, the total electric field,

$$\mathcal{E}(\mathbf{r}, t) = \sum_{j=1}^3 E_j(t) \exp[i\mathbf{k}_j \cdot \mathbf{r} - i\omega_j t] + c.c., \quad (1.6)$$

where, ω_j , \mathbf{k}_j and E_j are the frequency, wavevector and temporal envelope of the incoming fields j . The explicit \mathbf{r} dependence (in Eqn. 1.5) has been ignored for simplicity. For a typical four wave mixing techniques, three such electric fields are applied to the sample. The optical signals are subjected to proper phase matching condition given by, $\mathbf{k}_s = \mp(\mathbf{k}_1 + \mathbf{k}_2 + \mathbf{k}_3)$. Mixing the signal generated after j - pulses with an additional heterodyne pulse gives us the heterodyne detected time-resolved signals, along without destroying the information about coherences [40, 41, 42]. The delays between the pulses τ_i are given by $t_i = \tau_{i+1} - \tau_i$ for $i \in \{1, 2, 3, \dots, n\}$. For two dimensional spectroscopy (2D), one of the three time delays between the pulses is set to 0, allowing a pair of incoming pulse to coincide. The heterodyne

detected signal is thus given by,

$$S(t_3, t_2, t_1) = \int_{-\infty}^{\infty} d\tau \mathcal{E}_{het}(\tau) \hat{P}^3(\mathbf{r}, \tau), \quad (1.7)$$

where, $\mathcal{E}_{het}(\tau)$ is heterodyne field, and the third order polarization ($\hat{D}^3(\mathbf{r}, \tau)$) is given in terms of third order response functions $R(t_3, t_2, t_1)$ as,

$$\hat{P}(\mathbf{r}, \tau) = \int_0^{\infty} dt_3 \int_0^{\infty} dt_2 \int_0^{\infty} dt_1 R(t_3, t_2, t_1) \mathcal{E}(\mathbf{r}, \tau - t_3) \mathcal{E}(\mathbf{r}, \tau - t_3 - t_2) \mathcal{E}(\mathbf{r}, \tau - t_3 - t_2 - t_1) \quad (1.8)$$

This thesis focuses on heterodyne detected signals derived from set of definitions given in Eqn. 1.7 and Eqn. 1.8 unless otherwise stated. Another detection technique, homodyne detection, where the phase information is lost can still be used to study phase-insensitive measurements [43], and more recently in X-ray diffraction measurements [44]. The homodyne technique is not part of this thesis, interested readers are directed towards Ref. [45] and references therein.

The third order response function $R(t_3, t_2, t_1)$ in Eqn. 1.8 can be separated in coherent ($R_c(t_3, t_2, t_1)$) and incoherent ($R_{in}(t_3, t_2, t_1)$) contributions due to sequential processes. Coherent contributions are from processes where the entire optical process is completed before the system relaxes to an exciton population. The detailed derivation of coherent nonlinear response functions $R_c(t_3, t_2, t_1)$ in closed form based on the generalized Bethe-Salpeter equations [46], which was originally used for finding two particle wavefunctions (to study deuteron ground state), for molecular polaritons confined to an optical cavity is done in Chapter 2. In order to proceed, we next discuss what optical cavities are and how molecular polaritons are formed with an experimental schematic that will be used in the majority of this thesis (c.f. Sec. 1.1.2). We conclude the chapter with an outline (c.f. Sec. 1.2) for rest of the thesis.

1.1.2 Optical Cavity

Accounting for the photon statistics in a confined cavity and barring any nonlinear interactions, the underlying physics of a single mode optical cavity can be understood by coupling of harmonic oscillators as aptly explained in Ref. [47] (and given in Eqn. (1.12)). A simple optical cavity can be conceived by having two highly reflective concave mirrors aligned along the z axis set apart by length L_c such that only $\lambda/2$ standing wave of the photon field is confined along this axis. The cavity photon energy then is dependent on the plane wavevector \mathbf{k}_{\parallel} . This wavevector that is parallel to \mathbf{k}_z^c is related to the fundamental cavity resonance frequency ω_0 by,

$$\mathbf{k}_{\parallel} = \frac{\omega_0}{\hbar c} \sin(\theta), \quad (1.9)$$

where θ is the incident angle of photon pumping. The photon energy is quantized along $\mathbf{k}_z^c = \frac{2\pi}{L_c}$ for cavity length L_c . The effective cavity energy can be controlled by changing the angle of incidence and is thus given by [48],

$$\omega_c = \omega_0 \left(1 - \frac{\sin(\theta)^2}{n_{eff}^2} \right)^{-1/2}. \quad (1.10)$$

Cavity coupling (under the dipole approximation with cavity photon) for a molecular mode i is given by,

$$g_i = \sqrt{N} \boldsymbol{\mu}_i \cdot \mathbf{e}_c \sqrt{(\hbar\omega_c/2\epsilon_0 V)}, \quad (1.11)$$

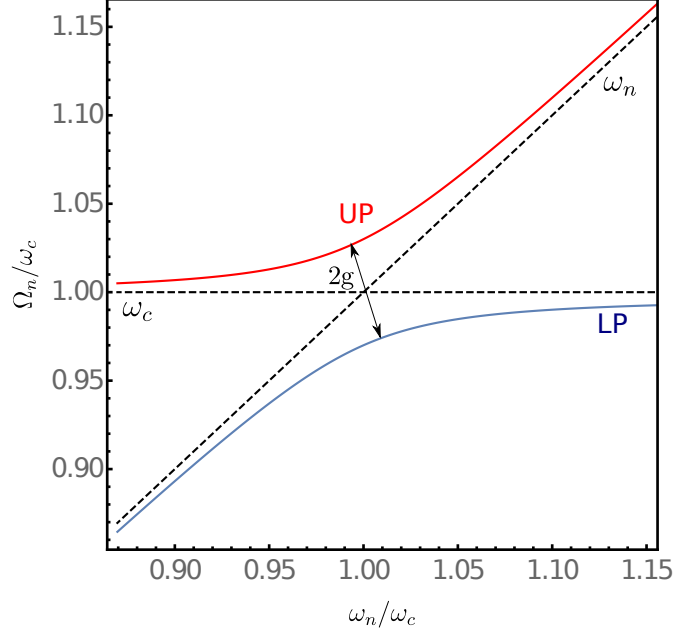


Figure 1.1: The scaled energies of upper (UP, red solid line) and lower (LP, blue solid line) polaritons as a function of ω_n/ω_c where ω_n is molecular energy and ω_c is cavity energy (both black dashed lines) for a single molecule in single mode optical cavity. The ratio is equivalent to changing effective cavity coupling g . The closest gap between the UP and LP at avoided crossing gives the measure of rabi splitting $\sim 2g$.

where, N , is the number of molecules. $\boldsymbol{\mu}_i$ is the transition dipole moment of the mode i , \mathbf{e}_c is the cavity electric field vector, ϵ_0 is vacuum permittivity, and V is the cavity mode volume [49, 50, 51, 52, 53, 54, 55].

Strong coupling to the cavity photon is usually considered when g is much larger compared to the other dephasing constants, namely the cavity decay rate (κ) and molecular dephasing γ . This can be achieved in one of two ways: a) By decreasing the cavity mode volume V , which is achievable even for single molecules [50, 56, 57]. For this method, however, one could run the risk of the breaking dipole approximation and coupling to cavity the photon could be complicated. A more straight forward way is b) by increasing the number of molecule N as g scales as \sqrt{N} which relies on the simple fact that effective dipole $\boldsymbol{\mu}_i$ scales as \sqrt{N} . One of the most recent developments in achieving the strong coupling regime is done by using a sub-wavelength grating (SWG) for both mirrors in Fig. 1.2 [58]. This is because it can be

fabricated to have a fraction of thickness of that of usual distributed Bragg reflector (DBR) or Fabry-Perot (FB) type cavities allowing for a small effective cavity length.

An illustrative example for formation of a molecular polariton can be done by the following Hamiltonian,

$$H = \omega_c a^\dagger a + \omega_n b^\dagger b + \frac{g}{2}(a^\dagger b + b^\dagger a), \quad (1.12)$$

where ω_c is the cavity photon energy and can be controlled by the changing incidence angle θ in Eqn. (1.10). ω_n is the molecular eigenvalue and g is the cavity coupling. Upon diagonalizing this hamiltonian, we can get the polariton with energies Ω_n for upper (UP) and lower (LP) polariton branches. The eigenvectors associated to them are called the polariton basis associated to the Hopfield-Bogolybov coefficients. The energy dispersion for the upper and lower polaritons is shown in Fig. 1.1.

Even when confined along \mathbf{k}_z^c the electromagnetic fields are three dimensional. Usually for quantum dots (1D), quantum wells (2D) or larger molecules (3D) the effective polaritons formed along the measurement axis that is along one of the \mathbf{k}_i axis in Fig. 1.2 can be viewed as 0,1 and 2D polaritons respectively due to the intrinsic cylindrical symmetry of the optical cavity we are interested in.

Possible experimental measurement technique

One of the possible ways to perform multidimensional spectroscopy on molecular polaritons that are formed as “dressed” (cavity photon + Frenkel excitons) is presented in Fig.1.2. Molecules (or molecular aggregates) are placed in a single mode cavity with energy described by Eqn. (1.10) confined along cavity axis \mathbf{k}_z^c with cavity incidence angle θ along it. Once

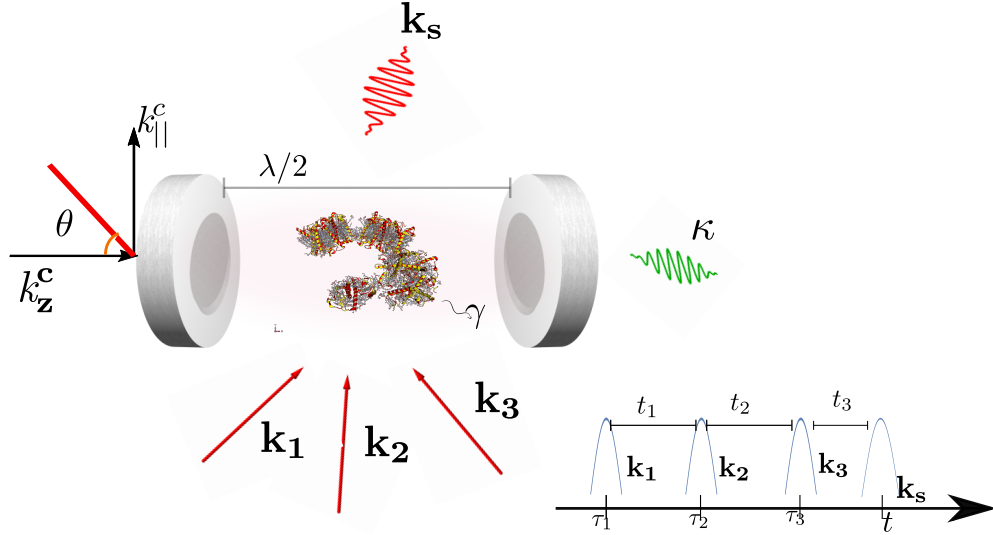


Figure 1.2: Schematic to illustrate possible experimental setup to measure nonlinear optical signals discussed in this thesis. The optical cavity with mirrors $\lambda/2$ distance apart can allow for strong coupling to the molecular vibrational and electronic degrees of freedom. Molecular aggregate with dephasing γ is placed in single mode optical cavity with photon is confined along \mathbf{k}_z^c . κ is cavity dephasing. $\mathbf{k}_i : i \in \{1, 2, 3, s\}$ are three incoming external field wave vectors and signal mode respectively. $t_i : i \in \{1, 2, 3, s\}$ is as described in text and assumed in Eqn. (1.7).

the molecular polaritons are prepared at thermal equilibrium (which can be achieved with slightly off-resonant cavity photon excitations) we can interact the molecular polariton with the incoming optical fields with wavevectors $\mathbf{k}_i : i \in \{1, 2, 3\}$ and detect the signal along \mathbf{k}_s axis using known multidimensional spectroscopic techniques (c.f. (1.7)).

1.1.3 Light Harvesting Complex II

Light harvesting complex II (LHCII), an assembly pigment protein, constitutes more than half of the antenna complexes found in plants. Charge separation processes which is done by channeling the absorbed photons to the reaction center in photosystem II (RC-PSII) initiates in LHCII. The 2.7 resolution structure [59] reveals that the trimer complex is composed of three monomeric units, each consisting of 14 chlorophyll, embedded in a protein and

residing in thylacoid membranes, as belonging to 8 chlorophyll a (*Chla*) in the stromal, and 6 chlorophyll b (*Chlb*) in the lumenal layers.

The arrangements of *Chla* and *Chlb* plays a crucial role in the energy transfer which occurs in a single exciton manifold. The extensive molecular dynamics simulations and fitting to experimental spectra of linear absorption (LA), transient absorption (TA), linear dichroism (OD) and circular dichroism (CD) [60, 61, 62, 63, 64, 65, 66]. provides the proper parameters that will be used in this thesis. It is not structurally clear how some of the *Chla* connect the monomers to form a trimer in extensive LHCI networks. The LHCI monomer has 14 singly excited states (usually labelled as e_i in this thesis, unless otherwise stated) where i indexes the singly excited states. There are $N(N + 1)/2 = 14 * 15/2 = 105$ doubly excited states (labelled as f_i).

The many body dynamics of two and more excitons and its signatures in confined optical cavities will be studied in the majority of the applications presented in this thesis (Except Chapter 3). The Frenkel exciton Hamiltonian, explained in Sec. 1.1.1, will be used to model these light harvesting complexes.

1.2 Outline

In chapter 2, we develop the quasiparticle representation of coherent multidimensional spectroscopy for molecular polaritons. This technique allows for a faster calculation of nonlinear signals in terms of polariton-polariton scattering matrices $\Gamma(\omega)$.

In chapter 3, we use the sum over state (SOS) technique to expand time domain two-dimensional technique, double quantum coherence (DQC) over two polariton eigen basis. This is used to illustrate how the single and double vibrational polariton manifolds may be modified by varying the cavity coupling strength. Applications are made to the amide-I

(CO) and amide-II (CN) bond vibrations of N-methylacetamide confined in a single mode optical cavity.

In chapter 4, the scaling of nonlinear optical signal, particularly double quantum coherence developed in chapter 2, is revisited when polaritons deviate from bosonic nature. We present a slightly different formalism based on q -deformed bosons to explicitly incorporate the N , where N is the number of molecules in a single mode optical cavity to illustrate the signal enhancement as a function of the deformation parameter q and $N + 1$ polariton numbers.

Finally, in chapter 5 we conclude the thesis by summarizing results from each chapter. Relevant appendices are provided after the bibliography.

Chapter 2

Quasiparticle representation of multidimensional signal

Polaritons, dressed light-matter quasiparticles, have different optical properties compared to excitons [67, 68]. Over the past few decades there has been extensive theoretical understanding and experimental demonstration on how the physical [69, 67, 70, 71, 72, 73, 53] and chemical [74, 75, 76, 77, 78, 55, 79] behaviour of exciton are modified in confined optical cavity. Polaritons are well studied in semiconductors [67, 68], and of lately a new surge of interest has risen in understanding molecular polaritons due to their implications in designing new material [80, 81], controlling non-adiabatic chemical dynamics via modified chemical potential energy landscapes [78, 77, 82] and energy transfer processes [83, 74]. The key to all of these interesting phenomena lies in the strength of cavity couplings interactions to QD [84, 85], atoms [68], molecules [9, 55] or macromolecules [80, 81] confined in optical microcavities or nanocavities. Cavity coupling (g) is linear in vacuum field operators of the confined optical cavity and scales as \sqrt{N} for N number of molecules. This linear coupling is enough to describe majority of aforementioned interesting physical and chemical modifications.

Some open questions related to molecular polaritons are: how this cavity coupling strength (g) effects the nonlinear interactions (like polariton-polariton interactions) [86], how they manifest as physically observable quantities, and how new emergent physical phenomena like polariton Bose Einstein Condensates (pBEC) [69, 70], modified molecular anharmonicities [9]. Multidimensional spectroscopy can be used to investigate these questions[6]. Multidimensional spectroscopy have been carried out on 2D studies for electronically excited states in semiconductor cavity for nano-particles like $In_{0.04}Ga_{0.96}As$ has been demonstrated [87, 88], electronic exciton-polariton interactions of quantum wells in microcavity [89]. We have theoretically shown that anaharmonicities in single molecule like *N – methylacetamide* can be modified as coupling to cavity and vibrational-polaritons are varied [9]. Authors in [90] had applied the nonlinear exciton equations (NEE) proposed for Frenkel excitons by [39] to calculate linear response for molecular aggregates in microcavity. *Ab initio* calculations using methods developed in [91, 92, 93].

In this work, we develop the quasiparticle representation of multidimensional optical response for molecular polaritons in single mode optical cavities based on equations of motion for polaritons. Nonlinearity in optical signal is often attributed to nonvanishing polariton-polariton scattering, $\Gamma(\tau)$. We derive the coherent third order response function in terms of $\Gamma(\tau)$. Neglecting the population transport, and approximating the the expectation values of products of polariton operators (\hat{p}_i), as $\langle \hat{p}_{j_1}^\dagger \hat{p}_2^\dagger \cdots \hat{p}_1 \hat{p}_2 \cdots \rangle = \langle \hat{p}_1^\dagger \hat{p}_2^\dagger \cdots \rangle \langle \hat{p}_1 \hat{p}_2 \cdots \rangle$ [94], naturally allows us to rewrite the multidimensional response functions in terms of polariton-polariton scattering matrices [65, 95, 39]. under coherent polariton dynamics limit. Nonlinear polariton equations (NPE) are then derived using Heisenberg equation of motion for the polariton dynamical varibales under truncation schemes used for nonlinear exciton equations (NEE) [95, 39, 65] allowing us to write self-consistent set of equation in quasiparticle (polariton) basis. Using NEE, the response functions can be derived in terms of exciton-exciton scattering matrices[39, 65] and has been used for multidimensional spectroscopy of large

macromolecules [96]. NPE is an extension of NEE to incorporate the single mode cavity photon variables in joint (“exciton+photon”) space.

Controlling the cavity coupling strength contributes to varying nonlinear optical signals due to modification in chemical and physical properties. In chapter 4, we will investigate third order signal (in particular, double quantum coherence signal with pulse configuration $\mathbf{k}_s = \mathbf{k}_1 + \mathbf{k}_2 - \mathbf{k}_3$) using quasiparticle representation utilizing nonlinear polariton equations which will be derived in this chapter. This method avoids explicit calculation of doubly excited states, reducing the dimensionality because the single polariton dynamical variables scales as N where as double polariton variables roughly scales as N^2 which is less computationally extensive compared to expanding the optical response functions in global eigenspace (c.f. Sec.2.1). The multidimensional signal thus can be represented in terms of polariton-polariton scattering matrices. For nonvanishing positive scattering time $\delta\tau > 0$ changes the resonant frequencies for doubly excited polariton manifold without having to explicitly calculate the two-polariton manifold. Consequently, the computations time is hugely reduced.

2.1 Model Hamiltonian

The electronic excitations for large macromolecules can be modelled using Frenkel exciton Hamiltonian. It thus suffices to start with N Frenkel exciton coupled to a single mode optical cavity (with energy ω_c) to derive the non-linear polariton equations, [97, 39, 65, 84].

$$H_0 = H_1 + H_2. \tag{2.1}$$

Where, H_1 contains all the linear order interacting terms, and is given by,

$$H_1 = \omega_c a^\dagger a + \sum_k \omega_k B_k^\dagger B_k + \sum_{k \neq l} J_{k,l} B_k^\dagger B_l + g \sum_k \left(a^\dagger B_k + B_k^\dagger a \right), \quad (2.2)$$

and, the quadratic terms are contained in H_2 given by,

$$H_2 = \sum_{kl,mn} U_{kl,mn} B_k^\dagger B_l^\dagger B_m B_n. \quad (2.3)$$

Here, $a^\dagger(a)$ are cavity photon creation (annihilation) operators and obeys bosonic commutation relations, $B_k^\dagger(B_l)$ are exciton creation (annihilation) operators for mode $k(l)$ and usually follows commutation relation in Eqn. (1.2), but for simplicity will be assumed to be bosonic in nature. ω_c is the cavity energy. And, ω_k is the exciton energy of mode k , J_{kl} is the dipole coupling between excitons at sites k and l , $U_{kl,mn}$ is the exciton-exciton interaction and finally, $g = \sum_k \boldsymbol{\mu}_k \cdot \mathbf{e}_c \sqrt{N} \left(\frac{\pi \hbar c}{n_{eff}^2 \lambda \epsilon_0 V} \right)^{1/2}$ is the cavity-exciton coupling strength for mode k with where, $\boldsymbol{\mu}_k$ is the exciton dipole moment, \mathbf{e}_c is the cavity electric field vector, N is the number of exciton, λ is the cavity resonance wavelength, ϵ_0 is vacuum permittivity and finally $V = (\lambda/n_{eff})^3$ is the cavity mode volume.

Let us assume $|G\rangle$ to be the global ground state containing no optical photon and all molecular aggregates in their respective ground state, i.e., $a|G\rangle = B_l|G\rangle = 0$. Furthermore, H_1 in Eqn. (2.2) conserves number of polaritons, i.e., $[H_1, \hat{N}] = 0$. We define the total number operator for polaritons as,

$$\hat{N} = a^\dagger a + \sum_j^N B_j^\dagger B_j, \quad (2.4)$$

and it counts number of excitations with respect to $|G\rangle$. This implies that we can canonically construct eigenstate of H_1 using products of linear combination of photons and exciton operators. We assume $U_{kl,mn} \ll \omega_k$ allowing us to treat H_2 as perturbation, thus condition $[H_1, \hat{N}] = 0$ is sufficient to define polariton creation operator (\hat{p}_i) for mode i ,

$$\hat{p}_i^\dagger = C_i a^\dagger + \sum_j^N X_{ji} B_j^\dagger. \quad (2.5)$$

Polariton annihilation operator \hat{p}_i for mode i is defined as conjugate transpose of \hat{p}_i^\dagger . Furthermore, coefficients C_i and X_{ji} are found by Hopfield-Bogolyuov transformation [98] of Eqn. (2.2) which is only tractable by numerical diagonalization for $N > 5$. We next define the n^{th} excited polariton as,

$$|\psi_n\rangle = \hat{P}_1^n |G\rangle \quad (2.6)$$

where, we have used following shorthand,

$$\hat{P}_1^n = \prod_{i=1}^n \hat{p}_i^\dagger. \quad (2.7)$$

For our purpose, the singly excited polariton states are given by,

$$|\psi_1\rangle = \hat{P}_1^1 |G\rangle = \hat{p}_1^\dagger |G\rangle \quad (2.8)$$

and doubly excited polariton states are given by,

$$|\psi_2\rangle = \hat{P}_1^2|G\rangle = \left(\sum_{i,j}^2 \hat{p}_i^\dagger \hat{p}_j^\dagger \right) |G\rangle. \quad (2.9)$$

Diagonalizing Eqn. (2.2) for first excited states, i.e., $n = 1$, thus give,

$$H_1|\psi_1\rangle = \Omega_m|\psi_1\rangle, \quad (2.10)$$

where, Ω_n are the first excited polariton energies of mode n . In order to rewrite Eqn. (2.1) in terms of polariton operators, we must define the commutation relations for polariton operator. After explicitly writing the polariton creation (annihilation) operators in terms of exciton and photon operators using Eqn. (2.5) we get at,

$$[\hat{p}_i, \hat{p}_j^\dagger] = \delta_{ij} \left(|C_i|^2 + \sum_{j=1}^N |X_{ji}|^2 [B_i, B_i^\dagger] \right). \quad (2.11)$$

As explained earlier (and for rest of this chapter), we set $[B_i, B_i^\dagger] = 1$ for simplicity. This gives following easily achievable normalization condition for the Hopfield-Bogolyubov coefficients,

$$|C_i|^2 + \sum_{j=1}^N |X_{ji}|^2 = 1 \quad (2.12)$$

in order for polariton operators to be treated as bosonic in nature with,

$$[\hat{p}_i, \hat{p}_j^\dagger] = \delta_{ij} \quad (2.13)$$

Complete treatment of Eqn. (2.11) is done in Chapter 4 using q – *deformed* analytics.

Using Eqn. (2.5) and commutation relations, Eqn. (2.13) we can rewrite Eqn. (2.1) as,

$$H_{pol} = \sum_i^{N+1} \Omega_i \hat{p}_i^\dagger \hat{p}_i + \frac{1}{2} \sum_{ij,kl} \tilde{V}_{ij,kl} \hat{p}_i^\dagger \hat{p}_j^\dagger \hat{p}_k \hat{p}_l. \quad (2.14)$$

Where, Ω_i are polariton energies, and $\tilde{V}_{ij,kl}$ is polariton-polariton interaction term which is defined as,

$$\tilde{V}_{ij,kl} = U_{kl,mn} X_i^* X_j^* X_k X_l, \quad (2.15)$$

where, $X_i = \sum_j^N X_j i$. The interaction to an ultrashort external field $\mathcal{E}^*(t) = \mathcal{E} \delta(t - \tau) e^{-i\omega\tau}$ given by,

$$H_{int} = - \sum_n \mu_n \mathcal{E}^*(t) \hat{p}_n + H.c. \quad (2.16)$$

where, μ_n is polariton transition dipole moments of mode n and can be found using Hopfield-Bogolyubov transformation. Using Eqns. (2.14) and (2.16), the total Hamiltonian of our

concern then is,

$$H_{tot} = H_{pol} + H_{int}. \quad (2.17)$$

This completes our definition of total Hamiltonian providing the basis for derivation of nonlinear polariton equations.

2.2 Coherent Nonlinear Polariton Equations

Of course, finding the global eigenvalues $\Omega_n^{(g)}$ obtained by solving $H_1|\psi_n\rangle = \Omega(g)_n|\psi_n\rangle$ (using Eqn. (2.10) for global polariton wavefunction c.f. Eqn. (2.6)) requires largers computation power and sum over state (SOS) techniques expands the optical response in these basis $|\psi_n\rangle$. An efficient way to achieve this is by using self-consistent set of nonlinear equations that relates dynamical polariton variables derived using Heisenberg's equation of motion. The coherent polariton dynamics can be evaluated by truncating the hierarchial Heisenberg equations of motions, i.e., $id\hat{p}_m/dt = [\hat{p}_m, H_{tot}]$. The expectation values The expectation values $\langle \dots \rangle = \langle \psi_0 | \dots | \psi_0 \rangle$ with respect to polariton ground state $|\psi_0\rangle$.

To this end, we define general polariton dynamical variables,

$$P_{(n)}^{\sigma_{ij}} = \left\langle \prod_n^N \hat{p}_n^{\sigma_{ij}} \right\rangle \quad (2.18)$$

where $i \in \{0, 1, \dots, m\}$ counts number of dagger (\dagger) terms and $j \in \{0, 1, \dots, m\}$ counts nondagger terms. (n) is defined as indices running over N -tuples. σ is $m \times m$ matrix where m is determined by the dimension of the truncation scheme. For our purpose we will set

$m = 3$ levels. σ can be thought as the metric for counting orders of polariton operators in normal ordered form and is given by,

$$\sigma = \begin{matrix} & \begin{matrix} 0 & 1 & 2 \end{matrix} \\ \begin{matrix} 0 \\ 1 \\ 2 \end{matrix} & \begin{pmatrix} 00 & 01 & 02 \\ 10 & 11 & 12 \\ 20 & 21 & 22 \end{pmatrix} \end{matrix} \quad (2.19)$$

where each element is an ordered pair of ij and $0, 1, 2$ are the ground, first and second excited manifolds respectively. Eqn. (2.18) takes following explicit forms when restricted to two polariton variables, which is sufficient to derive equations upto third order spectroscopy for molecular polaritons,

$$P_n^{\sigma_{01}} = \langle \hat{p}_n^{\sigma_{01}} \rangle = \langle \hat{p}_n \rangle \quad (2.20)$$

for single variable and,

$$P_{nm}^{\sigma_{02}} = \langle \hat{p}_n^{\sigma_{01}} \hat{p}_m^{\sigma_{01}} \rangle = \langle \hat{p}_n \hat{p}_m \rangle \quad (2.21)$$

for double polariton variables. It is important to include the pure dephasing due to coupling to the bath in molecular aggregates. For simplicity we neglect these effects until Chapter 5 when we calculate double photon coincidence for Light Harvesting Complex II (LHII) in single mode optical cavity. This simpler treatment is useful to get relevant structural information and are physically viable at lower temperatures since the effects due to nuclear

vibrations and phonon baths due to protein environments are small. Performing explicit Heisenberg equations of motion on the dynamical variables we have following polariton dynamics equations,

$$i\hbar \frac{dP_m^{\sigma_{01}}}{dt} - \sum_n \tilde{\Omega}_{mn} P_n^{\sigma_{01}} = P_m^{\sigma_{10}} \sum_{nkl} \left(\tilde{V}_{mn,kl} P_{kl}^{\sigma_{02}} + \mathcal{P}_{mn,kl} (P_k^{\sigma_{01}} E_l(t) + E_k(t) P_k^{\sigma_{01}}) \right) + E_m(t) \quad (2.22)$$

and, the for two-polariton dynamical equation

$$i\hbar \frac{dP_{nm}^{\sigma_{02}}}{dt} - \sum_{kl} (W_{mn,kl} + \tilde{V}_{mn,kl}) P_{kl}^{\sigma_{02}} = - \sum_{kl} (\delta_{mk} \delta_{nl} - \mathcal{P}_{mn,kl}) P_k^{\sigma_{01}} E_l(t) + E_k(t) P_k^{\sigma_{01}} \quad (2.23)$$

where,

$$\tilde{\Omega}_{mn} = \hbar \delta_{mn} \Omega_n \quad (2.24)$$

$$W_{mn,kl} = \tilde{\Omega}_{mk} \delta_{nl} + \delta_{mk} \tilde{\Omega}_{nl} \quad (2.25)$$

$$\mathcal{P}_{mn,kl} = \delta_{mn} \delta_{mk} \delta_{nl} (1 - q). \quad (2.26)$$

For what follows in this chapter, we will set $q = 0$ which is equivalent to setting excitons to behave fully bosonic in nature i.e., $\mathcal{P}_{mn,kl} = 0$. Furthermore, we have used,

$$E_n(t) = \mu_n \mathcal{E}^*(t). \quad (2.27)$$

Since the contribution third order response function derived in this way is independent from $S_1 \rightarrow S_2$ allowing us to conveniently ignore $\mu^{(2)} = 0$ described in chapter 1. The observable under dipole approximation is thus the expectation value of following dipole operator,

$$\langle \hat{D} \rangle = \left\langle \sum_n \mu_n (\hat{p}_n + \hat{p}_n^\dagger) \right\rangle. \quad (2.28)$$

Polariton-polariton scattering matrix contains all the non-linearity when the deviation from bosonic nature is not considered ($q = 0$). We next derive this expression using local structure of commutation relations of polariton operators (c.f. Eqn (2.13)). To this end, we need to solve the NPE given in Eqn. (2.22) and (2.23). This is easily done by setting $E_n(t) = \delta(t)$ which renders the NPE equations to be entirely homogenous giving following set of definition for N - polariton Green's functions, in compact form,

$$P_{(n)}^{\sigma ij}(t) = \sum_{(n')} G_{(n'),(n)}^{(N)} P_{(n')}^{\sigma ij}(0) \quad (2.29)$$

where, $N = i + j$ gives the order of Green's function which are $2N$ - adic tensors. (n) are N indices separated by 2-tuples. The ones relevant for our calculations are,

$$P_n^{\sigma 01}(t) = \sum_n G_{mn}^{(N)} P_{n'}^{\sigma 01}(0) \quad (2.30)$$

$$P_{mn}^{\sigma 02}(t) = \sum_{m'n'} G_{mn,m'n'}^{(N)} P_{m'n'}^{\sigma 02}(0) \quad (2.31)$$

$$(2.32)$$

Since we are assuming polaritons to be bosonic in nature, $P_n^{\sigma 01}(0)$ can be assumed to have bosonic distribution at thermal equilibrium. We are now in position to derive expressions for two-polariton correlation functions in terms of polariton-polariton scattering matrices.

2.3 Response functions in terms of polariton Green's function

In this section we derive expressions for coherent time domain third order response functions $R^{(c)}(t_3, t_2, t_1)$ for the time delays t_i for $i \in \{1, 2, 3\}$. In order to do so, we must evaluate $P_{(n)}^{\sigma ij}(t)$ to third order in driving field $\mathcal{E}(t)$. For this, we start with following first order term for $P_{(n)}^{\sigma ij(1)}(t)$,

$$P_n^{\sigma 01(1)}(t) = i \int_0^\infty \sum_m G_{mn}^{(1)} E_m(\tau - t) d\tau. \quad (2.33)$$

Plugging Eqn. (2.33) into Eqn. (2.23) and Eqn. (2.22), we get,

$$P_{mn}^{\sigma 02}(t) = i^2 \int_0^\infty dt_2 \int_0^\infty dt_1 \sum_{m'n', kk'} G_{mn, m'n'}^{(2)} G_{kk'}^{(1)} \bar{E}_{m'n', k'}(\tau - t_2) E_k(\tau - t_2 - t_1). \quad (2.34)$$

Here we have defined $\bar{E}_{m'n', k'}(\tau) = \delta_{mk} E_n(\tau) + \delta_{nk} E_m(\tau)$. Now plugging Eqns. (2.33)-(2.34) into Eqn. (2.22) and (2.23) gives,

$$P_{\bar{\sigma} 01 n}^{\sigma}(t) = \int_0^{t_3} P_n^{\sigma 01(3)}(t, t_3 - t, t_2, t) \quad (2.35)$$

where, the expansion of $P_n^{\sigma_{01}}(t)$ to third order is given by,

$$\begin{aligned}
P_m^{\sigma_{01}^{(3)}}(t, t_3 - t, t_2, t) &= i^4 \sum \tilde{V}_{sj,kl} \left\{ G_{ms}^{(1)}(t) G_{kl,n'm'}^{(2)}(t_3 + t_2 - t) G_{jj'}^{\dagger(1)}(t_3 - t) G_{k'k''}^{(1)}(t_1) \right. \\
&\times \mu_{j'} \bar{\mu}_{n'm',k'} \mu_{k''} + G_{ms}^{(1)}(t) G_{kl,n'm'}^{(2)}(t_3 - t) G_{jj'}^{\dagger(1)}(t_3 + t_2 - t) G_{ii'}^{(1)}(t_2 + t_1) \\
&\times \bar{\mu}_{n'm',i} \mu_{j'} \mu_{i'} + G_{ms}^{(1)}(t) G_{kl,n'm'}^{(2)}(t_3 - t) G_{jj'}^{\dagger(1)}(t_3 + t_2 + t_1 - t) G_{ii'}^{(1)}(t_2) \\
&\times \bar{\mu}_{n'm',i} \mu_{i'} \mu_j + G_{ms}^{(1)}(t) G_{kl,n'm'}^{(2)}(t_3 - t) G_{jj'}^{\dagger(1)}(t_3 - t) G_{i'l',i''j''}^{(2)}(t_2) \\
&\times \left. [G_{i''}^{(1)}(t_1) \delta_{j'l'} + \delta_{i'l'} G_{k'j''}^{\dagger(1)}(t_1)] \bar{\mu}_{n'm',l'} \mu_{l'} \mu_{k'} \right\}. \tag{2.36}
\end{aligned}$$

where we have used, $\bar{\mu}_{mn,k} = \mu_n \delta_{mk} + \mu_m \delta_{nk}$. We now define the third order response function as,

$$R(t_3, t_2, t_1) = \sum_n \mu_n P_n^{\bar{\sigma}_{01}}(t) \tag{2.37}$$

. The polariton-polariton scattering $\Gamma_{kl,mn}(t)$ matrix enters $R(t_3, t_2, t_1)$ through two polariton Green's function in $P_n^{\bar{\sigma}_{01}}(t)$. We next derive expressions for that.

2.4 Polariton-Polariton scattering matrix

Polariton-polariton scattering matrix $\Gamma_{kl,mn}(t)$ is derived by using Bethe-Salpeter equations to relate two polariton Green's function $\mathcal{G}^{(2)}(t)$ to free propagating two polariton function $\mathcal{F}(t)$. We will see later that due to local nature of polariton commutation relations we can get diadic scattering matrix which simplifies our expression as we need to invert a $N \times N$ matrix instead $N^2 \times N^2$ where N is total number of polaritons. However, here we will go ahead with the general form of scattering matrix indexed ($\{m\}, \{n\}$) where $\{n\}$ are incoming polariton

indices while $\{m\}$ are outgoing polariton indices. The proper Bethe-Salpeter equation thus reads,

$$\sum_{k'l'} G_{mn,k'l'}^{(2)}(\delta_{kk'}\delta_{l'l}) = F_{mn,kl}(t) + \sum_{m'n'k'l'} \int_0^t d\tau'' \int_0^{\tau''} d\tau' F_{mn,m'n'}(t - \tau'') \Gamma_{m'n',k'l'}(\tau'' - \tau') F_{k'l',kl}(\tau'). \quad (2.38)$$

The expression can be physically understood as follows:

- a Starting with two incoming polaritons labelled k and l that evolves freely for time τ , into outgoing polaritons labelled k' and l' . This information is encoded in expression $F_{k'l',kl}(\tau')$ given by,

$$F_{k'l',kl}(\tau') = G_{k'l'}^{(1)}(\tau') G_{kl}^{(1)}(\tau'), \quad (2.39)$$

where, $G_{kl}^{(1)}(\tau')$ is one polariton Green's function defined as,

$$G_{kl}^{(1)}(\tau') = \theta(\tau') \exp[-I\Omega t - \gamma t]_{kl}. \quad (2.40)$$

- b The particle with incoming modes k' and l' scatters for $\tau'' - \tau'$ to modes m' and n' and the relevant expression is stored in $\Gamma_{m'n',k'l'}(\tau'' - \tau')$ which we will derive shortly.
- c It then freely evolves from mode m' and n' to m and n for time $(t - \tau'')$. The integration over intermediate time variable yields an expression for two polariton scattering even to which we finally must add free polaritonic evolution $F_{mn,kl}(t)$ completing Dyson like equation to get overall two polariton Green's function $G_{mn,k'l'}^{(2)}$.

The fact that, in time domain, the exponential form of Green's function guarantees that it is unitless while, $\mathbf{\Gamma}(t)$ has dimensions of frequency squared. In frequency domain, Green's function has units of time, implies that polariton-polariton scattering matrix appears with units of angular frequency. In the representation depicted by Eqn. (2.38), a doubly excited state can be described as two polaritons residing on the same site which makes it possible for each polariton branch i to be doubly excited where the scattering appears as onsite anharmonicity $\tilde{V}_{mm,mm} = \Delta_m$. For two level polaritons, $\tilde{V}_{mm,mm} \rightarrow \infty$ which implies the polariton scattering is simply the (multiplicative) inverse of free two-polariton propagator with (additive) inverse frequency [39].

We will express relevant two-polariton functions in frequency domain which is related to time domain expression Fourier transform. For instance,

$$\mathbf{\Gamma}(t) = \int_0^\infty \frac{d\omega}{2\pi} \exp[-I\omega t] \mathbf{\Gamma}(\omega). \quad (2.41)$$

Using similar transforms, we get,

$$\mathcal{G}^{(2)}(\omega) = \mathcal{F}(\omega) + \mathcal{F}(\omega) \mathbf{\Gamma}(\omega) \mathcal{F}(\omega) \quad (2.42)$$

where, $\mathcal{G}^{(2)}(\omega)$, $\mathcal{F}(\omega)$ and $\mathbf{\Gamma}(\omega)$ are used as full tetradic tensors. Proper inversion then gives us the expression for polariton-polariton scattering matrix in frequency domain,

$$\mathbf{\Gamma}(\omega) = -\mathcal{F}(\omega)^{-1} + \mathcal{F}(\omega)^{-1} \mathcal{G}^{(2)}(\omega) \mathcal{F}(\omega)^{-1}, \quad (2.43)$$

where,

$$\mathcal{F}(\omega) = (\omega - \hat{\Omega} \otimes \mathbf{I}_d + \mathbf{I}_d \otimes \hat{\Omega} - I\eta)^{-1} \quad (2.44)$$

$$\mathcal{G}^{(2)}(\omega) = [\omega - (\hat{\Omega} \otimes \mathbf{I}_d + \mathbf{I}_d \otimes \hat{\Omega}) - \tilde{\mathcal{V}} - I\eta]^{-1} \quad (2.45)$$

where, $\hat{\Omega}$ is the matrix with elements Ω_{mn} and \mathbf{I}_d is identity matrix of dimension equivalent to number of polaritons. $\eta \rightarrow \infty$ guarantees causality. Substituting Eqn. (2.44) in Eqn. (2.43) then yields a simple expression for polariton-polariton scattering matrix,

$$\mathbf{\Gamma}(\omega) = [\mathbf{I}_d - \tilde{\mathcal{V}}\mathcal{F}(\omega)]^{-1}\tilde{\mathcal{V}}. \quad (2.46)$$

Now we exploit the locality of the polariton commutation relations to have a two indexed polariton-polariton scattering matrix,

$$\Gamma_{mn}(\omega) = (1 - \tilde{V}_{mn}F_{nm}(\omega))^{-1}\tilde{V}_{mn}, \quad (2.47)$$

where the local $F_{nm}(\omega)$ is defined as,

$$F_{nm}(\omega) = (\omega - \Omega_{mn} - \Omega_{nm})^{-1} \quad (2.48)$$

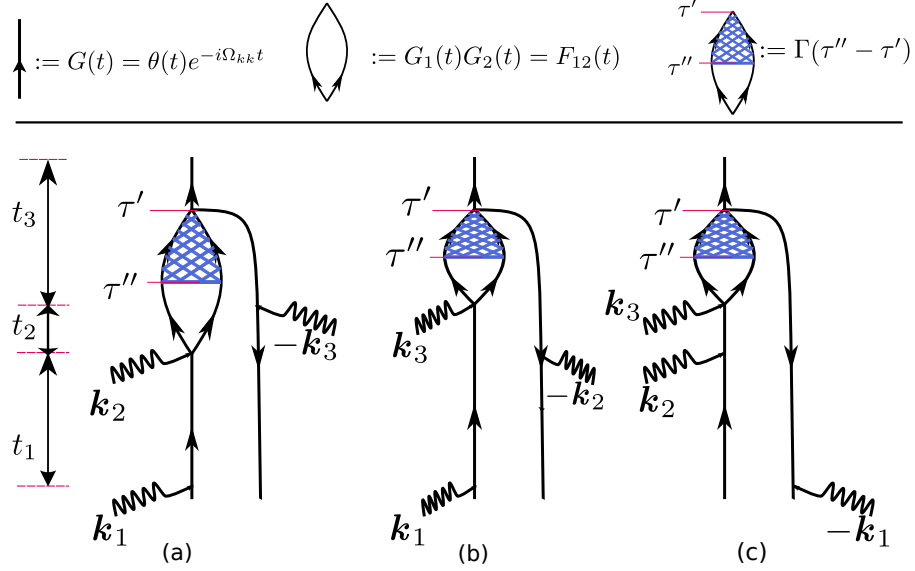


Figure 2.1: Coherent polariton dynamics represented by Feynmann diagrams (a) for \mathbf{k}_{III} c.f. Eqn. (2.53), (b) for \mathbf{k}_{II} c.f. Eqn. (2.52) and (c) for \mathbf{k}_I c.f. Eqn. (2.51)

. The single solid line as represents $G(t)$ propagation, the unshaded fish shaped represents free two-polariton propagator, and finally the blue shaded region in represents the two polariton scattering event for time interval $(\tau'' - \tau') > 0$. This scattering changes the resonant energies correctly adjusting the doubly excited polariton energies.

and, \tilde{V}_{mn} in local form is defined as,

$$\tilde{V}_{mn} = 2 \sum_{kl} U_{mn,kl} X_{ml}^* X_{nk}^* X_{lm} X_{kn} \quad (2.49)$$

with $X_{\mu\nu}$ being Hopfield-Bogolyubov coefficients.

2.5 Third order response functions for polaritons

2.5.1 Time domain

We are now in position to express $R(t_3, t_2, t_1)$ in terms of one polariton Green's function, polariton-polariton scattering matrix, and (ignoring incoherent polariton population trans-

fer) polariton population Green's functions. This is done by substituting Eqn. (2.38) into Eqn. (2.37) to get,

$$R_{coh}(t_3, t_2, t_1) = R_{coh}^{kI}(t_3, t_2, t_1) + R_{coh}^{kII}(t_3, t_2, t_1) + R_{coh}^{kIII}(t_3, t_2, t_1) \quad (2.50)$$

where, the photon-echo (rephasing signal) in time domain is given by,

$$\begin{aligned} R_{coh}^{kI}(t_3, t_2, t_1) &= \left(\frac{i}{\hbar}\right)^3 \boldsymbol{\mu}_k^* \boldsymbol{\mu}_l \boldsymbol{\mu}_n \boldsymbol{\mu}_m^* \int_0^{t_3} d\tau' \int_0^{\tau'} d\tau G_{kk'}^{(1)}(t_3 - \tau') \Gamma_{k'm', l'n'}(\tau' - \tau) \\ &\times G_{kk'}^{(1)}(\tau) G_{nn'}^{(1)}(t_2 + \tau) G_{m'm}^{*(1)}(t_1 + t_2 + \tau') \end{aligned} \quad (2.51)$$

Similarly, the non-rephasing photon echo signal in time domain is given by,

$$\begin{aligned} R_{coh}^{kII}(t_3, t_2, t_1) &= \left(\frac{i}{\hbar}\right)^3 \boldsymbol{\mu}_k^* \boldsymbol{\mu}_l \boldsymbol{\mu}_n^* \boldsymbol{\mu}_m \int_0^{t_3} d\tau' \int_0^{\tau'} d\tau G_{kk'}^{(1)}(t_3 - \tau') \Gamma_{k'm', l'n'}(\tau' - \tau) \\ &\times G_{kk'}^{(1)}(\tau') G_{n'n}^{*(1)}(t_2 + \tau') G_{mm'}^{(1)}(t_1 + t_2 + \tau). \end{aligned} \quad (2.52)$$

And, finally double quantum coherence signal in time domain is,

$$\begin{aligned} R_{coh}^{kIII}(t_3, t_2, t_1) &= \left(\frac{i}{\hbar}\right)^3 \boldsymbol{\mu}_k^* \boldsymbol{\mu}_l \boldsymbol{\mu}_n^* \boldsymbol{\mu}_m \int_0^{t_3+t_2} d\tau' \int_0^{\tau'} d\tau G_{kk'}^{(1)}(t_3 - \tau') \Gamma_{k'm', l'n'}(\tau' - \tau) \\ &\times G_{kk'}^{(1)}(\tau') G_{nn'}^{(1)}(t_2 + \tau) G_{m'm}^{*(1)}(t_1 + t_2 + \tau). \end{aligned} \quad (2.53)$$

2.5.2 Frequency domain

Fourier transforming Eqn. (2.51)- (2.53) with respect to the delays, t_1, t_2 and t_3 and denoting the respective fourier conjugates as $\bar{\Omega}_1, \bar{\Omega}_2$, and $\bar{\Omega}_3$, we get following set of coherent response functions using expressions for free-two polariton propagator $F_{mn}(\omega)$ (*c.f. Eqn. (2.48)*), polariton-polariton scattering $\Gamma_{kl,mn}(\omega)$ (*c.f. Eqn. (2.47)*) and single polariton Green's function $G_k(\omega) = [\omega - \Omega_k + i\gamma_k]^{-1}$ and γ_k as phenomenological dephasing for polariton in mode k . We begin with response function contributing to rephasing photon-echo signal,

$$\begin{aligned}
R_{coh}^{kI}(\bar{\Omega}_3, \bar{\Omega}_2, \bar{\Omega}_1) &= \left(\frac{i}{\hbar}\right)^3 \sum_{ijkl} \sum_{m,n'} \boldsymbol{\mu}_k^* \boldsymbol{\mu}_l \boldsymbol{\mu}_j \boldsymbol{\mu}_i^* G_k^{(1)}(\bar{\Omega}_3) \Gamma_{km',ln'}(\bar{\Omega}_3 + \Omega_{m'} + i\gamma_{m'}) \\
&\times F_{ln'}(\bar{\Omega}_3 + \Omega_{m'} + i\gamma_{m'}) \delta_{ki} \delta_{jl} G_j^{(1)}(\bar{\Omega}_2) G_i^{*(1)}(-\bar{\Omega}_2) G_i^{*(1)}(-\bar{\Omega}_1). \quad (2.54)
\end{aligned}$$

Similarly, the response function associated to non-rephasing photon echo signal is given by,

$$\begin{aligned}
R_{coh}^{kII}(\bar{\Omega}_3, \bar{\Omega}_2, \bar{\Omega}_1) &= \left(\frac{i}{\hbar}\right)^3 \sum_{ijkl} \sum_{m,n'} \boldsymbol{\mu}_k^* \boldsymbol{\mu}_l \boldsymbol{\mu}_j^* \boldsymbol{\mu}_i G_k^{(1)}(\bar{\Omega}_3) \Gamma_{km',ln'}(\bar{\Omega}_3 + \Omega_{m'} + i\gamma_{m'}) \\
&\times F_{lm'}(\bar{\Omega}_3 + \Omega_{m'} + i\gamma_{m'}) \delta_{ki} \delta_{jl} G_j^{(1)}(\bar{\Omega}_2) G_i^{*(1)}(\bar{\Omega}_2) G_i^{(1)}(\bar{\Omega}_1). \quad (2.55)
\end{aligned}$$

Finally, the double quantum coherence (DQC) response function signal is given by,

$$\begin{aligned}
R_{coh}^{kIII}(\bar{\Omega}_3, \bar{\Omega}_2, \bar{\Omega}_1) &= \left(\frac{i}{\hbar}\right)^3 \sum_{ijkl} \sum_{m,n'} \boldsymbol{\mu}_k^* \boldsymbol{\mu}_l^* \boldsymbol{\mu}_j \boldsymbol{\mu}_i \left[\Gamma_{kl,ji}(\bar{\Omega}_2) F_{ji}(\bar{\Omega}_2) - \Gamma_{kl,ji}(\bar{\Omega}_3 + \Omega_k + i\gamma_k) \right. \\
&\times \left. F_{ji}(\bar{\Omega}_3 + \Omega_k + i\gamma_k) \right] G_l^{(1)}(\bar{\Omega}_3) G_j^{*(1)}(\bar{\Omega}_1) G_k^{*(1)}(\bar{\Omega}_2 - \bar{\Omega}_3). \quad (2.56)
\end{aligned}$$

We have now developed full set of equations required to calculate third order optical signals in both time and frequency domains for coherent polariton dynamics, i.e., we have factorized the expected values of product of dagger terms with products of non-dagger which does not account for any incoherent population transfer due to factoring of expectation values of terms like $P_{mn}^{\sigma_{11}}(t)$ to $P_m^{\sigma_{10}}(t)P_n^{\sigma_{01}}(t)$ (where $P_{(m)}^{\sigma_{ij}}(t)$ is defined in Eqn. (2.18) with (m) representing list of $2(i+j)$ 2-tuples).

2.5.3 Heterodyne detected signals

Projection of induced polarizabilities (c.f. Eqn. 1.8) that is related to the response function we calculated in this chapter (Eqn. (2.50)-(2.53)) for time domain can be related to optical signal for heterodyne detected technique given by Eqn. 1.7. Performing triple fourier transform (restricted to upper half plane, i.e., with boundary $\{0, \infty\}$) with respect to time delays t_i in $i \in 1, 2, 3$ then gives us frequency domain signals, i.e.,

$$S(\bar{\Omega}_3, \bar{\Omega}_2, \bar{\Omega}_1) = \int_0^\infty dt_3 \int_0^\infty dt_2 \int_0^\infty dt_1 \exp[i(\Omega_3 t_3 + \bar{\Omega}_2 t_2 + \bar{\Omega}_1 t_1)] S(t_3, t_2, t_1). \quad (2.57)$$

Using Eqn. (2.57) and plugging appropriate response functions from Eqns. (2.54)-(2.56) we arrive at following heterdyne detected signals.

$$\begin{aligned} S_{\mathbf{kI}}^{(coh)}(\bar{\Omega}_3, \bar{\Omega}_2, \bar{\Omega}_1) &= - \left(\frac{i}{\hbar} \right)^3 \sum_{ijkl} \sum_{m,n'} E_k^*(\Omega_l - \omega_s) E_l(\Omega_k - \omega_3) E_j(\Omega_j - \omega_2) E_k^*(\Omega_i - \omega_1) G_k^{(1)}(\bar{\Omega}_3) \\ &\times \Gamma_{km',ln'}(\bar{\Omega}_3 + \Omega_{m'} + i\gamma_{m'}) F_{ln'}(\bar{\Omega}_3 + \Omega_{m'} + i\gamma_{m'}) \\ &\times \delta_{ki} \delta_{jl} G_j^{(1)}(\bar{\Omega}_2) G_i^{*(1)}(-\bar{\Omega}_2) G_i^{*(1)}(-\bar{\Omega}_1). \end{aligned} \quad (2.58)$$

where, we have used $\boldsymbol{\mu}_k \mathcal{E}_k(\omega) = E_k(\omega)$ (and the conjugates are defined accordingly) for simplicity of expressions. And, ω_i with $i \in \{s, 1, 2, 3\}$ are the pulse width of the i^{th} incoming fields. Using similar definition, we also get non-rephasing photon echo signal,

$$\begin{aligned}
S_{\mathbf{k}II}^{(coh)}(\bar{\Omega}_3, \bar{\Omega}_2, \bar{\Omega}_1) &= - \left(\frac{i}{\hbar} \right)^3 \sum_{ijkl} \sum_{m,n'} E_k^*(\Omega_l - \omega_s) E_l(\Omega_k - \omega_3) E_j(\Omega_j - \omega_2) E_k^*(\Omega_i - \omega_1) G_k^{(1)}(\bar{\Omega}_3) \\
&\times \Gamma_{km',ln'}(\bar{\Omega}_3 + \Omega_{m'} + i\gamma_{m'}) F_{lm'}(\bar{\Omega}_3 + \Omega_{m'} + i\gamma_{m'}) \\
&\times \delta_{ki} \delta_{jl} G_j^{(1)}(\bar{\Omega}_2) G_i^{*(1)}(\bar{\Omega}_2) G_i^{(1)}(\bar{\Omega}_1). \tag{2.59}
\end{aligned}$$

The coherent heterodyne detected signal for double quantum coherence in frequency domain is then given by,

$$\begin{aligned}
S_{\mathbf{k}III}^{(coh)}(\bar{\Omega}_3, \bar{\Omega}_2, \bar{\Omega}_1) &= - \left(\frac{i}{\hbar} \right)^3 \sum_{ijkl} E_k^*(\Omega_l - \omega_s) E_l(\Omega_k - \omega_3) E_j(\Omega_j - \omega_2) E_k^*(\Omega_i - \omega_1) \\
&\times \left[\Gamma_{kl,ji}(\bar{\Omega}_2) F_{ji}(\bar{\Omega}_2) - \Gamma_{kl,ji}(\bar{\Omega}_3 + \Omega_k + i\gamma_k) \right. \\
&\times \left. F_{ji}(\bar{\Omega}_3 + \Omega_k + i\gamma_k) \right] G_l^{(1)}(\bar{\Omega}_3) G_j^{*(1)}(\bar{\Omega}_1) G_k^{*(1)}(\bar{\Omega}_2 - \bar{\Omega}_3). \tag{2.60}
\end{aligned}$$

2.6 Discussion and Conclusion

In this chapter, we have developed third order heterodyne detected signals for molecular polaritons assuming polaritons behave as bosons in both time (Eqns. (2.51), (2.52) and (2.53) (as third order response functions) and in frequency domain (Eqns. (2.58)–(2.60)) using nonlinear polariton equations (NPE) (Sec. 2.2 and equations there in). These set of self-consistent equation allows us to write third order response functions in terms of polariton-polariton scattering matrix, $\boldsymbol{\Gamma}(t)$ in time domain c.f. Eqn. (2.47)), equivalently in

frequency domain (c.f. Eqn. (2.43) for time domain expression); two polariton propagator $\mathcal{F}(\omega)$ given in Eqn. (2.44) (see Eqn. (2.39)) and single polariton Green's functions. The key advantage of deriving the nonlinear optical signals using NPE is to avoid explicit calculations of doubly excited states which increases N^2 with N being number of molecular polaritons. For larger macromolecules this can become computationally cumbersome to achieve specially when more modes of optical cavities are included as the molecular polaritons thus formed may not be exhibit Frenkel type properties.

Usually Wannier type polaritons can be achieved with more optical mode [99]. Computation of doubly excited states then scale as N^4 . The method presented here, though focuses on Frenkel type molecular excitons confined in optical cavities, can be extended to include should one were to work with multimode optical cavities, and for large number of cavity mode treatment similar to phonon bath [39] with resonance replaced by photon bath with appropriate energies. The power of NPE is clear in systems when the doubly excited states aren't explicitly calculated but are achieved by incorporating proper polariton-polariton scattering terms for positive scattering times.

Optical nonlinearities that are introduced due to polariton-polariton scattering can be easily studied using techniques developed specifically double quantum coherence (DQC) signals (Eqn. (2.60)). For most cases, the exciton-exciton interaction term ($U_{kl,mn}$) in Eqn. (2.3) changes to polariton-polariton interaction term $\tilde{V}_{kl,mn}$ via Eqn. (2.15) with Hopfield coefficients contributions is due to excitonic part X_{mn} , and upon summing over the m index to compose single index for both incoming and outgoing polaritons modes allowing the possibilities of local form of $\tilde{V}_{kl,mn} \equiv \tilde{V}_{mn}$ which makes quadratic terms local. This along with the intrinsic local nature of the polariton operators reduces the effective dimensionality of the tetradic scattering matrix to diadic, which implies computing optical signals (Eqns. (2.58)–(2.60)) requires inversion of $N \times N$. Again, due to the possibility of writing the induced polarizabilities in local forms allowing one for direct structural measurements of molecular

polaritons for larger macroaggregates coupled to one (or few) mode optical cavity, similar to those done for excitons in Ref. [96].

In conclusion, I would like to emphasize on double quantum coherence signal in Eqn. (2.60) and how it's simple structure allows us to measure any anharmonicities present in the system either due to polariton-polariton scatterings (assumed in this chapter, and used in chapter 4, and ??) or because of both polariton-polariton scattering and polariton statistics (as applied in chapter ??). The terms in square brackets in Eqn. (2.60) vanish when $\bar{\Omega}_2$ is resonant with sum of $\bar{\Omega}_3 + \Omega_k$. This is true when there is no anharmonicities. Allowing the DQC signals to be unique measure for studying molecular anharmonicities due to different polariton scattering processes. In other words, anharmonicities (Δ_k can be defined as $\bar{\Omega}_2 - \bar{\Omega}_3 + \Omega_k$ and this vanishes for harmonic cases.

Chapter 3

Molecular vibrational polaritons

This chapter is solely based on: “**Prasoon Saurabh** and Shaul Mukamel. Two-dimensional infrared spectroscopy of vibrational polaritons of molecules in optical cavity. *The Journal of chemical physics*, **144**(12):124115, 2016” [9]. Here, I present, how strong coupling of molecular vibrations to an infrared cavity mode affects their nature by creating dressed polariton states. This is done by showing how the single and double vibrational polariton manifolds may be controlled by varying the cavity coupling strength and probed by a time domain two-dimensional infrared (2DIR) technique, double quantum coherence. Particular applications are made to the amide-I (CO) and amide-II (CN) bond vibrations of N-methylacetamide.

3.1 Introduction

Elementary physical and chemical properties of molecules can be modified by coupling them to the optical modes of a cavity thus forming strongly coupled *matter + field* states known as polaritons [50, 56]. These have been widely studied in atoms. Electronic polaritons in molecules have been extensively studied both experimentally and theoretically [81, 74, 90].

Vibrational polaritons in the infrared has been recently demonstrated in molecular aggregates [52, 53, 54, 55] and in semiconductor nano-structures [100, 101, 87]. The radiation matter coupling is related to cavity frequency ω_c by, $g_i = \sqrt{N}\boldsymbol{\mu}_i \cdot \mathbf{e}_c\sqrt{(\hbar\omega_c/2\epsilon_0V)}$, where, N is the number of molecules. $\boldsymbol{\mu}_i$ is the transition dipole moment of the mode i , \mathbf{e}_c is the cavity electric field vector, ϵ_0 is vacuum permittivity, and V is the cavity mode volume [49, 50, 51, 52, 53, 54, 55]. While strong coupling to cavity modes has been realized even for a single atom, $N = 1$, [50, 56, 57] polaritons in organic molecules were reported for large $N(\sim 10^{17})$ [52]. With the advent of anomalous refractive index materials [102, 103], sub-wavelength Fabry-Perot microcavities [104], and nanocavities [105] it may become possible to achieve strong cavity coupling of single molecules.

Coherent multidimensional infrared spectroscopy is a powerful time domain tool that can probe anharmonicities and vibrational energy relaxation pathways [106, 107, 108, 109, 110]. Vibrational polaritons were experimentally reported [52, 54, 55] and calculated [53, 111] recently. Multidimensional spectroscopic studies for electronically excited states in semiconductor cavity for nano-particles like $In_{0.04}Ga_{0.96}As$ has been demonstrated [87, 88]. Similarly, electronic exciton-polariton interactions of quantum wells in microcavity [89] has also been reported. Bipolaritons generated using four wave mixing techniques have been used as efficient entangled photon source [112, 113].

In this article, we calculate 2DIR signals for vibrational polaritons, focusing specially on the double quantum coherence (DQC) technique. Studying DQC of molecular vibrational polaritons in optical cavity can be used to study the effects of strong couplings on the vibrational anharmonicities and consequently allow us to control these anharmonicities. We introduce DQC signal in next section (Sec.3.2), we then study single vibrational mode (Amide-I of NMA) coupled to a single mode cavity and calculate DQC in section (Sec.3.3), followed by two vibrational modes (Amide-I+II of NMA) coupled to a single mode cavity (Sec.3.4); and finally conclude in Sec. 3.5.

3.2 Vibrational polaritons and their DQC signal

Vibrational modes (Fig. 3.1) coupled to an infrared cavity under the Rotating Wave Approximation (RWA) are described by the hamiltonian [39, 65, 114, 52, 53, 54, 55],

$$\begin{aligned}
 H_0 &= \omega_c(\theta)a^\dagger a + \sum_i^m \omega_i b_i^\dagger b_i + \sum_{i \neq j}^m J_{ij} b_i^\dagger b_j \\
 &- \sum_{ij}^m \frac{\Delta_{ij}}{2} b_i^\dagger b_j^\dagger b_i b_j + \sum_{i,j=1}^m g_i \left(a^\dagger b_i + b_i^\dagger a \right), \tag{3.1}
 \end{aligned}$$

where, $a(a^\dagger)$ and $b(b^\dagger)$ are annihilation(creation) operators for the cavity photon, and vibrational excitation respectively, which satisfy boson commutation relations, $[a, a^\dagger] = 1; [b_i, b_j^\dagger] = \delta_{ij}$ and $\hbar = 1$. $\omega_c(\theta) = \omega_0 \left(1 - \frac{\sin^2(\theta)}{n_{eff}^2} \right)^{-1/2}$, is the angle-dependent cavity energy with ω_0 being cavity cut-off (or maximum) energy and, θ the angle of incidence to the cavity mirrors. We set $\theta = 0^\circ$ for simplicity. ω_i is vibrational frequency of mode i . J_{ij} is the scalar coupling between two vibrational modes i and j , while Δ_{ij} is the anharmonicity between respective modes. Finally, the coupling strength of vibrational modes i to an optical mode is, g_i as described in introduction.

The cavity volume ($V = (\lambda/n_{eff})^3$) depends on cavity resonance wavelength (λ) and effective intra-cavity refractive index (n_{eff}) [49, 50, 51]. Decreasing n_{eff} can also be used for strong coupling to single molecular vibrational excitation, for instance, when the refractive indices of one of the two layers' of a Distributed Bragg Reflector (DBR) Fabry-Perot is equal to the empty cavity refractive index n_c , say $n_c = (n_2 n_1)$, then $n_{eff} = \sqrt{n_1 n_2}$. In this case, choosing either one of the layers to be material with anomalous refractive index may decrease $n_{eff} < 1$ [104]. The vacuum Rabi splitting Ω_R of mode i is $2\hbar g_i$.

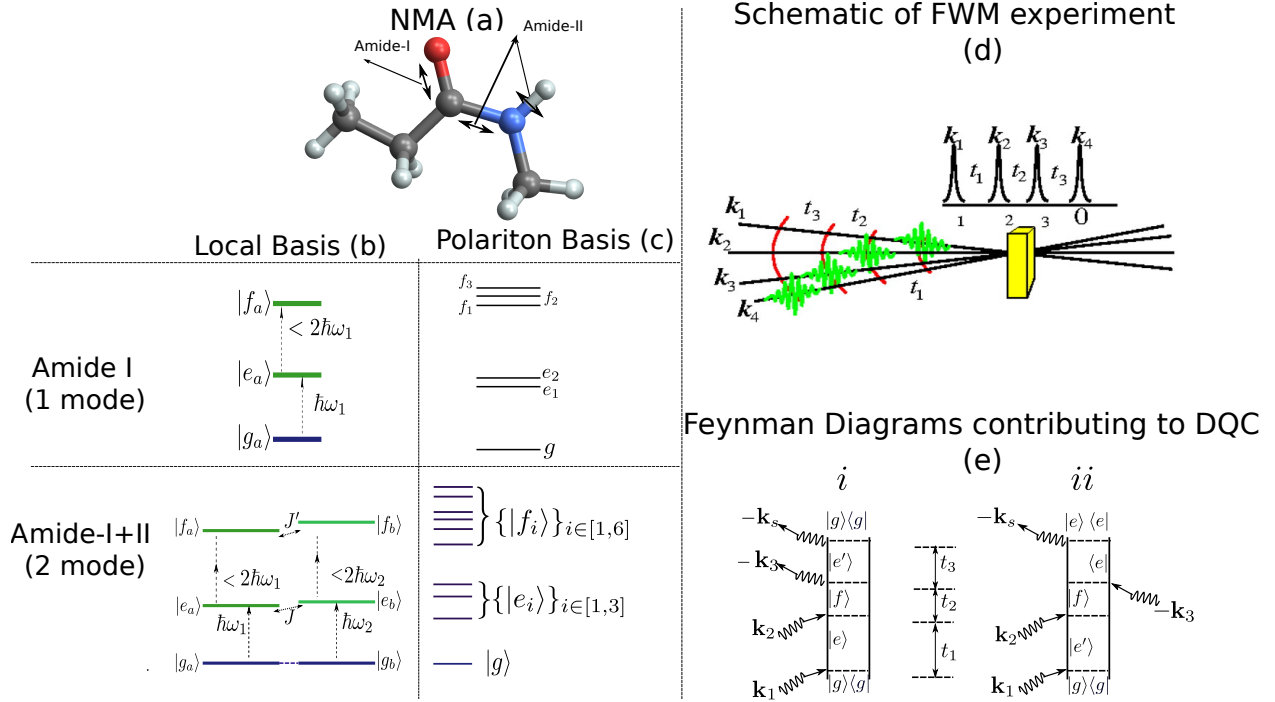


Figure 3.1: Amide-I ($C = O$ symmetric stretch) and Amide-II (CN symmetric stretch + NH bend) vibrations are represented using double sided arrow for $N - Methylacetamide$ in (a). Eigen-energies of Amide-I and coupled Amide-I and Amide-II motifs in local basis and polariton basis (see Sec.SI of supplementary information A.1 for detail) are given in (b) and (c) respectively. (d) schemes the FWM experiment, the yellow sample is the DBR Fabry-Perot cavity coupled to molecular vibrations (see text for detail) and, (e) shows the relevant ladder diagrams contributing to double quantum coherence (DQC) technique.

DQC is a four wave mixing signal generated by three chronologically ordered pulses with wavevectors \mathbf{k}_1 , \mathbf{k}_2 and \mathbf{k}_3 and detected by with a fourth pulse in the direction, $\mathbf{k}_{III} = \mathbf{k}_1 + \mathbf{k}_2 - \mathbf{k}_3$ (Fig.3.1 (e)) [107, 6]. The signal is recorded versus three time delays t_1 , t_2 and t_3 . We assume a three polariton manifold as shown in Fig. 3.1. Using the ladder diagrams for DQC (Fig. 3.1e) in polariton basis, which diagonalizes the first three and last terms of Eq. A.1 (Fig. 3.1, Sec.SI of supplementary information A.1), we see that system oscillates with frequency $\Omega_{eg} = \Omega_e - \Omega_g$ during time delay $t_1 = \tau_2 - \tau_1$ and with frequency $\Omega_{fe} = \Omega_f - \Omega_e$ during delay $t_2 = \tau_3 - \tau_2$ in both contributing diagrams (Fig. 3.1e). After the third pulse the system oscillates either with frequency $\Omega_{e'g}$ or $\Omega_{e'f}$ during the delay $t_3 = \tau_4 - \tau_3$. For harmonic case, $\Omega_{e'g} = \Omega_{e'f}$ where the DQC signal vanishes. A 3D signal $\mathcal{S}(t_3, t_2, t_1)$, which

can be written as double Fourier transform with respect to t_2 and t_3 as [107],

$$\mathcal{S}(\Omega_3, \Omega_2, t_1) = \int_0^\infty \int_0^\infty dt_3 dt_2 e^{i(\Omega_3 t_3 + \Omega_2 t_2)} \mathcal{S}(t_3, t_2, t_1). \quad (3.2)$$

Upon expanding in polariton eigenstates, the signal with time delay $t_1 = 0$ becomes,

$$\begin{aligned} \mathcal{S}(\Omega_3, \Omega_2, t_1 = 0) &= \sum_{ee',f} \frac{1}{(\Omega_2 - \Omega_{fg} + i\gamma_{fg})} \\ &\quad \left[\frac{\mu_{e'f} \mu_{ge'} \mu_{fg} \mu_{ge}}{\Omega_3 - \Omega_{e'g} + i\gamma_{e'g}} \right. \\ &\quad \left. - \mu_{ge'} \mu_{e'f} \mu_{fg} \mu_{eg} \frac{1}{\Omega_3 - \Omega_{fe} + i\gamma_{fe}} \right]. \end{aligned} \quad (3.3)$$

Where, μ_{ij} is the polariton transition dipole from states in manifold $j \rightarrow i$ while γ_{ij} is the respective dephasing. Note that the polariton eigenstates depend on the effective cavity coupling strengths, $\tilde{g}_i \left(= \sqrt{Ng_i^2 - \frac{1}{4}(\kappa - \gamma_i)^2} \right)$, where κ is cavity decay rate, and γ_i is dephasing rate of respective mode [49]. Tuning the cavity coupling allows to control spectral structures of the singly and doubly excited vibrational polariton manifolds (Fig.3.2 and can be captured using DQC as illustrated in the following section (Sec. 3.3).

3.3 A Single vibrational mode coupled to single cavity mode

The Amide motifs ($O = C - N - H$) link the amino-acid in peptides containing fundamental structural information, for instance, backbone geometry, interactions with hydrogen bonds and dipole-dipole interactions [115]. 2D spectroscopy of the amide-I and II symmetric vibra-

Table 3.1: Parameters used in this work. ω_0 is cavity cut-off frequency. $\omega_{1,2}$ are vibrational exciton (1,2) (*Amide – I*, *Amide – II*) energies, $\gamma_{1,2}$ are their respective dephasing rates, J_{ij} is harmonic scalar coupling, and Δ_{ij} are exciton-exciton interaction energies.

(in cm^{-1})	Cavity	Amide-I	Amide-I+II
Energy	$\omega_0=1625$	$\omega_1=1625$	$\omega_1=1625, \omega_2=1545$
Dephasing	$\kappa=0$	$\gamma_1=20$	$\gamma_1 = \gamma_2=20$
Anharmonicities (Local basis)	$\Delta_{00} = 0$	$\Delta_{11}=15$	$\Delta_{11}=15, \Delta_{22}=11$ $\Delta_{21} =$
Scalar coupling	-	-	$\Delta_{12}=10$ $J_{12}=15$
Eff. refractive ind.	$n_{eff} = 0.5$	-	-
Anharmonicities (Polariton basis)		$\tilde{V}_{ij} = \frac{\Delta_{ij}}{2} X_i ^2 X_j ^2$	

tions (Fig. 3.1e) have been studied [116, 106]. We focus on the Amide-I vibrations in NMA (Table. 3.1). We consider a single Amide-I stretch mode in resonance with the cavity mode and large anharmonicity ($\Delta_{ij} > \gamma_{ij}$) with varying coupling strengths \tilde{g}_1 ranging from 0 to 80 cm^{-1} (Table. 3.1). For a single vibrational mode (Fig.3.1), the three polariton manifolds have a ground state (g), two single excited states (e) and three doubly excited states (f). Furthermore, for detuning ($\delta = \omega_1 - \omega_c$), the polariton basis modifies the anharmonicity $\Delta_{11} (\rightarrow \tilde{V}_{11} = 16\Delta_{11}|\tilde{g}_1^4/(\delta^2 - 16\tilde{g}_1^2)|)$.

Using Eq. A.8 and ladder diagrams (Fig. 3.1e) the signals $|\mathcal{S}_i(\Omega_3, \Omega_2, 0)|$, $|\mathcal{S}_{ii}(\Omega_3, \Omega_2, 0)|$ and $|\mathcal{S}(\Omega_3, \Omega_2, 0) = |\mathcal{S}_i(\Omega_3, \Omega_2, 0) + \mathcal{S}_{ii}(\Omega_3, \Omega_2, 0)|$ are shown in Fig. 3.3 and 3.4 in left, center and right columns respectively (sec. 3.3). Absolute values are shown to illustrate peak assignments and affects of varying coupling strengths (\tilde{g}_i). For completeness, the respective absorptive (Im) and dispersive (Re) parts of the DQC signals are shown in Sec.AIIIA in Appendix A. The peak splittings depends on coupling strengths (\tilde{g}_i) and polariton anharmonicities (\tilde{V}_{ij}) and are given Sec.A6 of Appendix A.

Free molecule (Fig. 3.3): The Amide-I vibrations in NMA (without cavity) is a simple three level system as shown in Fig. 3.1. Under this condition, $e_1 = e_2$ and $f_1 = f_2 = f_3$, thus we only observe single peak resonant at $\Omega_{fg} = 3168 \text{ cm}^{-1}$ on Ω_2 axis. The peaks

due to $|\mathcal{S}_i(\Omega_3, \Omega_2, 0)|$ (Fig. 3.3(a)) shows $\Omega_{eg} = 1625\text{cm}^{-1}$ resonance, while $|\mathcal{S}_{ii}(\Omega_3, \Omega_2, 0)|$ (Fig. 3.3(b)) shows resonance at $\Omega_{fe} = 1617\text{cm}^{-1}$ along Ω_3 axis. The total signal (Fig. 3.3(c)) thus shows two peaks due to resonances at Ω_{eg} and Ω_{fe} .

Weak coupling regime (Fig. 3.4-top row) with $\tilde{g}=20\text{cm}^{-1}$: Upon varying the coupling strength, there are two singly excited and three doubly excited polariton states (Fig. 3.1 b-c, Sec SII-S1 of [?]). We thus observe that all $|\mathcal{S}_i(\Omega_3, \Omega_2, 0)|$, $|\mathcal{S}_{ii}(\Omega_3, \Omega_2, 0)|$ and $|\mathcal{S}(\Omega_3, \Omega_2, 0)|$ show three distinct peaks along Ω_2 axis with energies resonant to $\Omega_{f_1g} = 2\Omega_{e_1g} - \tilde{V}_{11}$, $\Omega_{f_2g} = 2\Omega_{e_1g}$ and $\Omega_{f_3g} = 2\Omega_{e_2g} - \tilde{V}_{33}$ respectively. Along Ω_3 axis, $|\mathcal{S}_i(\Omega_3, \Omega_2, 0)|$ (Fig. 3.4(top, left)) shows peak resonance at Ω_{e_1g} and Ω_{e_2g} with splitting $\sim \tilde{g}$. The $|\mathcal{S}_{ii}(\Omega_3, \Omega_2, 0)|$ (Fig. 3.4(top, middle)) has six distinct peaks at energies resonant to Ω_{f_2, e_2} , Ω_{f_2, e_1} , Ω_{f_1, e_2} , Ω_{f_3, e_2} , Ω_{f_1, e_1} , Ω_{f_3, e_1} in increasing order respectively. The $|\mathcal{S}(\Omega_3, \Omega_2, 0)|$ (Fig. 3.4(top, right)) has diminished peaks at $\Omega_{f_2e_1}$ and $\Omega_{f_3e_2}$ due to destructive interference of $\Omega_{f_2e_1}$ with Ω_{e_1g} and $\Omega_{f_3e_2}$ with Ω_{e_2g} resonances.

Strong coupling regime (Fig. 3.4-bottom row) with $\tilde{g} = 50\text{cm}^{-1}$: The signals corresponding to $|\mathcal{S}_i(\Omega_3, \Omega_2, 0)|$ (Fig. 3.4(bottom, left)), $|\mathcal{S}_{ii}(\Omega_3, \Omega_2, 0)|$ (Fig. 3.4(bottom, middle)) and $|\mathcal{S}(\Omega_3, \Omega_2, 0)|$ (Fig. 3.4(bottom, right)) show peaks corresponding to Ω_{f_1g} , Ω_{f_2g} and Ω_{f_3g} along Ω_2 axis. Projections on Ω_3 axis for $|\mathcal{S}_{ii}(\Omega_3, \Omega_2, 0)|$ six peaks assigned as in weak coupling case, however the peak splitting between resonance pairs with energies $(\Omega_{f_2e_1}, \Omega_{f_1e_2})$ and $(\Omega_{f_3e_2}, \Omega_{f_1e_1})$ remains relatively constant and proportional to respective contributing anharmonicities. The total signal shows six peaks due to $\Omega_{f_2e_1}$ and $\Omega_{f_3e_2}$ diminished because of destructive interferences from resonances of singly excited polaritons.

This partial cancellation of peaks puts an upper bound on strong coupling strengths for fully resolved DQC signals. Furthermore by changing t_1 , we can observe the dynamics in singly and doubly excited polariton manifolds to obtain bountiful information regarding lifetimes of molecular vibrational bipolaritons. In case of zero detuning ($\delta = \omega_1 - \omega_c = 0$), the doublet peak splitting due to \tilde{V}_{11} is independent of coupling strength *i.e.*, $\tilde{V}_{11} = \Delta/32$. Thus DQC

can be used as direct measurements of anharmonicities due to vibrational polariton-polariton interactions for vanishing detuning cases. One has to be careful however, for $\delta \neq 0$ cases; as such conditions allow the anharmonicities to vary non-trivially ($\sim 16\Delta_{11}|\tilde{g}_1^4/(\delta^2 - 16\tilde{g}_1^2)^2|$). This may cause destructive interference of different peaks along Ω_3 axis.

3.4 Polaritons for two vibrational modes and their DQC signal

We now couple the Amide-I and Amide-II vibrations (Fig. 3.1, [116]) of a single NMA molecule ($N = 1$) to an infrared cavity. We next calculate the double quantum coherence (DQC) signals for vibrational molecular polaritons (Fig. 3.1 (e), Eq. A.8) utilizing Eqs.S2-S5 (of supplementary material A.1).

The overlapping of peaks due to anharmonicities is better illustrated in case of Amide-I+II vibrations coupled to single mode cavity. We next present three coupling regimes for such a condition. We assume $\tilde{g}_1/\tilde{g}_2 = \text{constant}$ for simplicity. The remainder of relevant parameters are shown in Table 3.1.

No cavity (Fig. 3.6)(a): The coupled Amide-I+II vibrations of NMA is effectively a three level system with two singly excited states and three doubly excited states in absence of cavity coupling. The two singly excited states are resonant with Ω_{e_1g} and Ω_{e_2g} . The three doubly excited states are resonant with frequencies $\Omega_{f_1g} = 2\Omega_{e_1g} - \Delta_{11}$, $\Omega_{f_2g} = \Omega_{e_1g} + \Omega_{e_2g}$ and $\Omega_{f_3g} = 2\Omega_{e_2g} - \Delta_{22}$ (Sec. SII of supplementary material A.1, Table 3.1). These peaks are observed along Ω_2 axis. Whereas, we only observe four peaks along Ω_3 axis in (Fig. 3.6(a, right column)) because the tuples $(\Omega_{f_2e_1}, \Omega_{f_1e_2}, \Omega_{e_1g})$ and $(\Omega_{f_3e_2}, \Omega_{f_1e_1}, \Omega_{e_2g})$ cannot be resolved due to anharmonicities (Δ_{ii} , Table 3.1).

Weak coupling regime with $\tilde{g} = 10\text{cm}^{-1}$ (Fig. 3.6)(b): Under these conditions, we observe five peaks along Ω_2 axis corresponding to $\Omega_{f_1g}, \Omega_{f_2g}, \Omega_{f_3g}, \Omega_{f_4g}, \Omega_{f_5g} = \Omega_{f_6g}$. Projections along Ω_3 axis shows two peaks for $|\mathcal{S}_i(\Omega_3, \Omega_2, 0)|$ (Fig. 3.6(b, bleft column)) resonant with frequencies $\Omega_{e_1g}, \Omega_{e_2g} \approx \Omega_{e_3g}$. For $|\mathcal{S}_{ii}(\Omega_3, \Omega_2, 0)|$ (Fig. 3.6(b, bmiddle column)) we would ideally expect eighteen peaks corresponding to $\Omega_{f_1e_3}, \Omega_{f_1e_2}, \Omega_{f_3e_4}, \Omega_{f_4e_2}, \Omega_{f_2e_3}, \Omega_{f_2e_2}, \Omega_{f_1e_1}, \Omega_{f_3e_3}, \Omega_{f_3e_2} = \Omega_{f_4e_1} = \Omega_{f_6e_3}, \Omega_{f_6e_2}, \Omega_{f_5e_3}, \Omega_{f_2e_1}, \Omega_{f_5e_2}, \Omega_{f_3e_1}, \Omega_{f_6e_1}, \Omega_{f_5e_1}$ in energetically increasing order. However, only twelve peaks are observed due to overlapping caused by anharmonicities and coupling strength. Similar to Amide-I vibrations of NMA in cavity, we observe fewer peaks in $|\mathcal{S}(\Omega_3, \Omega_2, 0)|$ (Fig. 3.6(b, right column)) than that of $|\mathcal{S}_{ii}(\Omega_3, \Omega_2, 0)|$ due to destructive interferences between $|\mathcal{S}_{ii}(\Omega_3, \Omega_2, 0)|$ and $|\mathcal{S}_i(\Omega_3, \Omega_2, 0)|$.

Strong coupling regime $\tilde{g} = 50\text{cm}^{-1}$ (Fig. 3.6(c)): Increasing coupling resolves the six bipolariton resonances along Ω_2 for all contributions to the DQC signal (Fig. 3.6(c)). Along Ω_3 axis, however, only $|\mathcal{S}_i(\Omega_3, \Omega_2, 0)|$ is more resolved with three peaks corresponding to $\Omega_{e_1g}, \Omega_{e_2g}$ and Ω_{e_3g} with splitting $\sim \tilde{g}_i$. Despite better peak resolution due to coupling strength dependent peak separations, resonances due to overlapping peaks cannot be fully resolved. The total signal (Fig. 3.6(right column)) only has 10 distinct peaks as a result of destructive interference of energies of Ω_{e_2g} and Ω_{e_3g} with some of the resonances from $|\mathcal{S}_{ii}(\Omega_3, \Omega_2, 0)|$.

Increasing coupling strengths provides us well resolved molecular vibrational bipolariton manifold structure (along Ω_2 axis), however, it may not provide well resolved DQC signals along Ω_3 axis requiring a careful tuning of \tilde{g}_i .

3.5 Conclusions

The Multidimensional DQC signals shown in Figs. 3.2 - 3.6 demonstrate how the ground state vibrational excitation manifolds are modified upon coupling to the cavity modes. The

anharmonicities in the case of Amide-I of NMA coupled to cavity (for non-zero detuning $\delta \neq 0$) are modified with cavity coupling strength, $\Delta_{ij} \rightarrow \tilde{V}_{ij} = 16\Delta_{11}|\tilde{g}_1^4/(\delta^2 - 16\tilde{g}_1^2)^2|$ and this can be observed in the peak splitting. For zero detuning, the anharmonicity is independent of coupling strength, i.e., $\lim_{\delta \rightarrow 0} \tilde{V}_{ij} = \Delta_{11}/32$. However, in the case of Amide-I+II of NMA coupled to the infrared cavity anharmonicities in polariton basis varying nontrivially by, $\tilde{V}_{ij} = 1/2\Delta_{ij}|X_i|^2|X_j|^2$ where, $X_{i/j}$ depend on higher order of coupling strengths. This causes several peaks to overlap beyond certain cavity coupling and this is why not all expected peaks for Ω_{fe} can be spectrally resolved in Fig. 3.6. However, we can use cavity coupling dependent anharmonicities for modifications of ground vibrational structures to mimic weakly interacting molecular vibrational multi-modes.

Controlling and manipulating lifetime of single molecular vibrations by tuning the coupling strengths and time delays between ultrafast pulses (say, t_1) can reveal new energy transfer mechanisms. Varying cavity polarization ($\boldsymbol{\mu}_k \cdot \mathbf{e}_c$) and incident angle (θ) in Eq. A.1 using collinear experiments [88] could provide information regarding spatial confinements of several vibrational excitations and possibilities of molecular vibrational condensates like usual electronic polariton condensates in organic [117] and inorganic [117, 118, 119] microcavities, if effective dense vibrational polaritons are obtained, which may be possible in larger macromolecules like J-aggregates. Time-varying cavity coupling strengths can be used to study dynamics of efficient cooling of molecular vibrational states for n -polariton manifolds using higher dimensional spectroscopic techniques.

This work can be extended to control collective molecular vibrational excitations, which may be a useful tool in molecular cooling [120] allowing to perform ultracold experiments even at room-temperature. Furthermore, by varying the time delays one could be able to modify molecular vibrations via cavity and catch them in action in real time. We show that, by varying the cavity coupling strength (\tilde{g}), it is possible to retrieve spectrally well-resolved molecular vibrational polariton(bipolariton) resonances which are otherwise difficult to re-

solve (see Fig. 3.2 - 3.6 for example). Similar results with respect of the anharmonicities and peak redistributions due to cavity coupling can be achieved using other 2DIR techniques, e.g. $\mathbf{k}_s = -\mathbf{k}_1 + \mathbf{k}_2 + \mathbf{k}_3$ or $\mathbf{k}_s = \mathbf{k}_1 - \mathbf{k}_2 + \mathbf{k}_3$, however, the full power of DQC measurements presented here for single molecule in optical cavity can be seen more easily for macromolecules. For such larger systems, a different and much faster numerical algorithms utilizing techniques similar to Nonlinear Exciton Equations (NEE) [65] will be useful. Studying the dynamics of modified electronic ground states by applying methods developed in Ref. [6] can also be done. In addition, incorporating electronic states can similarly be achieved to modify vibrational excitations of electronically excited states.

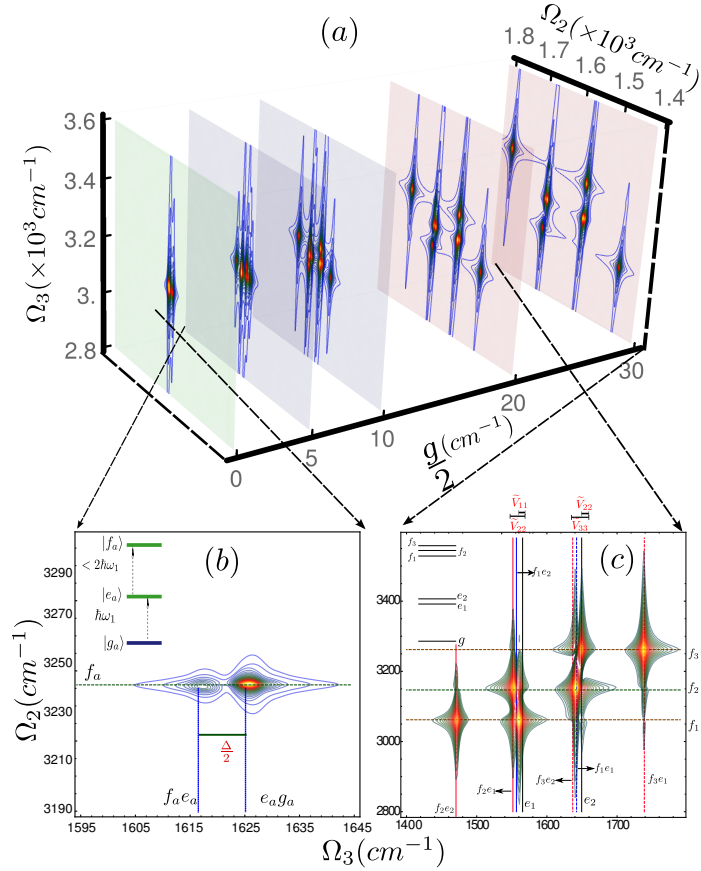


Figure 3.2: (a) Absolute value of DQC signal (Eq. A.8) for Amide-I vibrations of NMA, as we vary coupling strength (g) from no (green plane), weak (blue planes) and strong (red planes) coupling regimes. (b) Schematic representation of DQC signal (zoomed in the grey square at $g = 0 \text{cm}^{-1}$) with all possible peaks identified as intersections of different lines. (c) Same result but for strong coupling and the last panel. The lines are: i) Ω_{fe} labelled as $f_i e_j$ (dashed blue lines), ii) Ω_{eg} labelled as e_j (black solid lines), iii) Ω_{fg} labelled as f_i and appropriate anharmonicities (Δ_{ij} in local basis or \tilde{V}_{ii} in polariton basis) respectively. We wish to spectrally resolve (b) to (c).

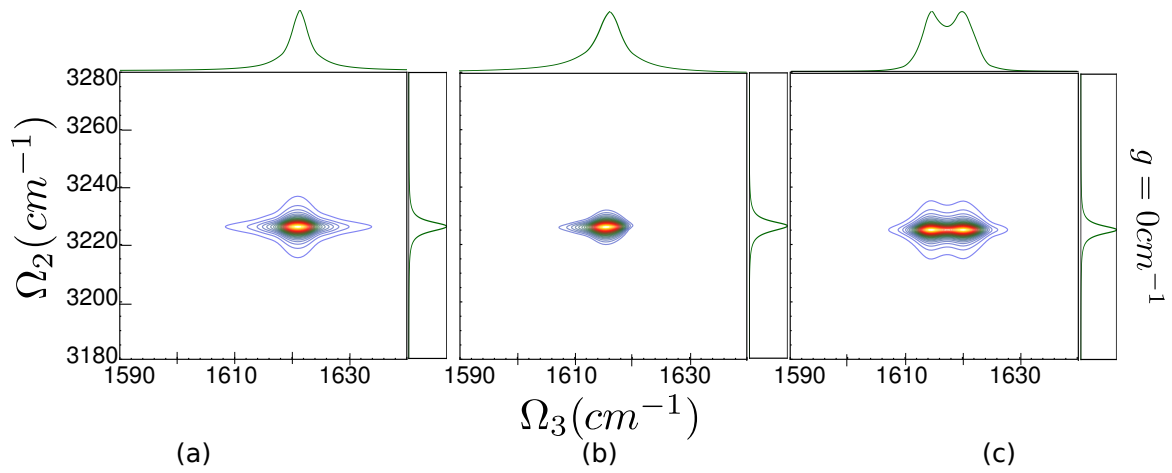


Figure 3.3: DQC signals for Amide-I vibrations in NMA using Eq. A.8 and ladder diagrams (Fig. 3.1e): (a) $|\mathcal{S}_i(\Omega_3, \Omega_2, 0)|$ with resonance at $\Omega_{eg} = 1625\text{cm}^{-1}$, (b) $|\mathcal{S}_{ii}(\Omega_3, \Omega_2, 0)|$ with resonance at $\Omega_{fe} = 1617\text{cm}^{-1}$ and (c) $|\mathcal{S}(\Omega_3, \Omega_2, 0)|$ with resonances at $\Omega_{eg} = 1625\text{cm}^{-1}$ and $\Omega_{fe} = 1617\text{cm}^{-1}$. The linear projections along each axis is shown in green. For simplicity, cavity field vector \mathbf{e}_c is assumed to be mostly parallel to molecular vibrational transition dipole μ_m . Amide-I vibrations (ω_1) is resonant to cavity cutoff frequency $\omega_0 = 1625\text{cm}^{-1}$. The anharmonicity are assumed $\Delta_{11} = 15\text{cm}^{-1}$ (Table 3.1).

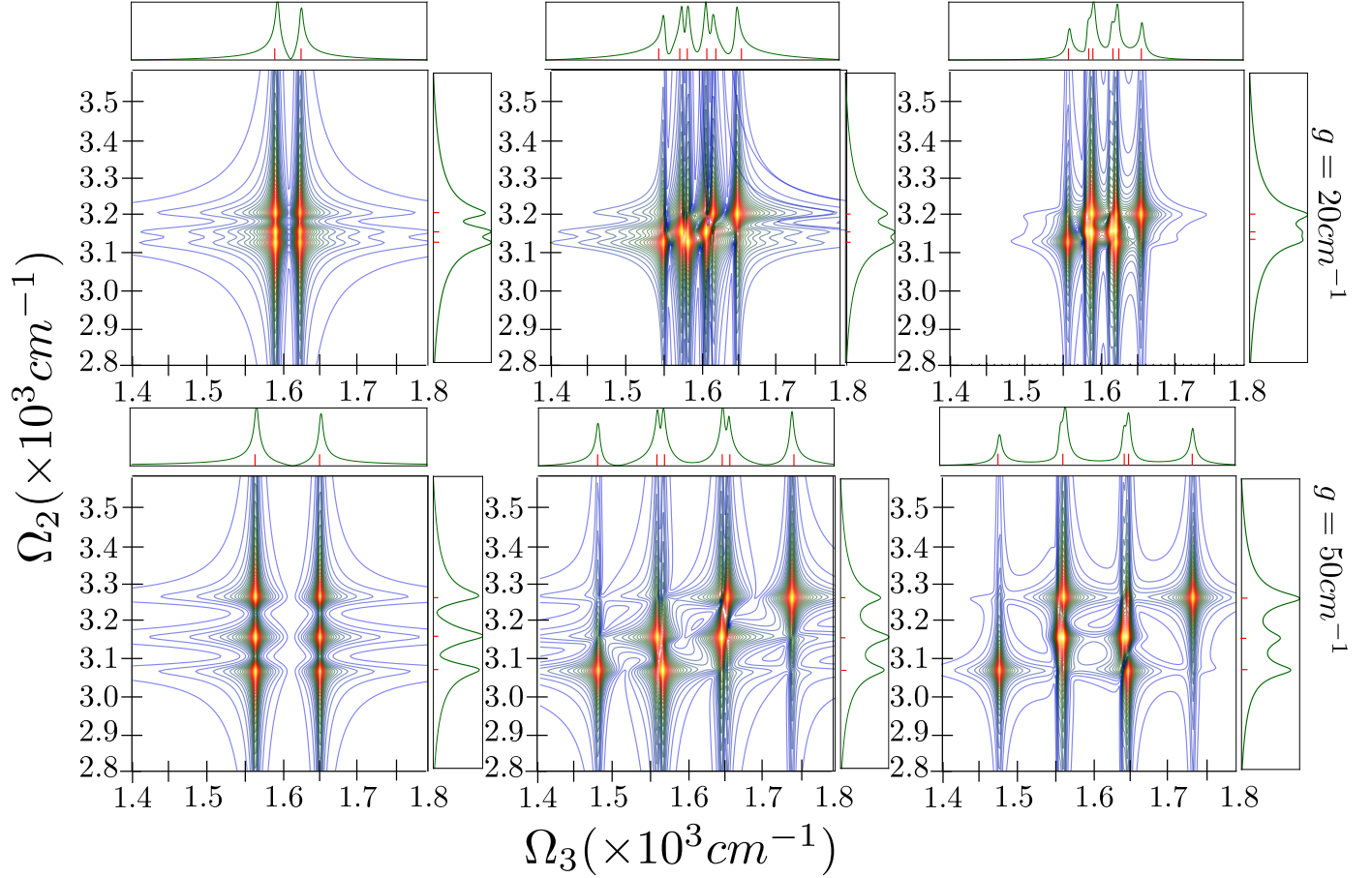


Figure 3.4: DQC signals using Eq. A.8 and ladder diagrams (Fig. 3.2b): *Columns* (left–) $|\mathcal{S}_i(\Omega_3, \Omega_2, 0)|$ with resonance at Ω_{e_1g} and Ω_{e_2g} ; (middle–) $|\mathcal{S}_{ii}(\Omega_3, \Omega_2, 0)|$ with resonance at Ω_{f_2,e_2} , Ω_{f_2,e_1} , Ω_{f_1,e_2} , Ω_{f_3,e_2} , Ω_{f_1,e_1} , Ω_{f_3,e_1} ; and (right–) $|\mathcal{S}(\Omega_3, \Omega_2, 0)|$ with respective resonances for Amide-I vibrations in NMA with cavity coupling *rows*: (a) 20cm^{-1} and (a) 50cm^{-1} . The linear projections along each axis is shown in green. For simplicity, cavity field vector \mathbf{e}_c is assumed to be mostly parallel to molecular vibrational transition dipole μ_m . Amide-I vibrations (ω_1) is resonant to cavity cutoff frequency $\omega_0 = 1625\text{cm}^{-1}$. The anharmonicity are assumed $\Delta_{11} = 15\text{cm}^{-1}$ (Table 3.1)

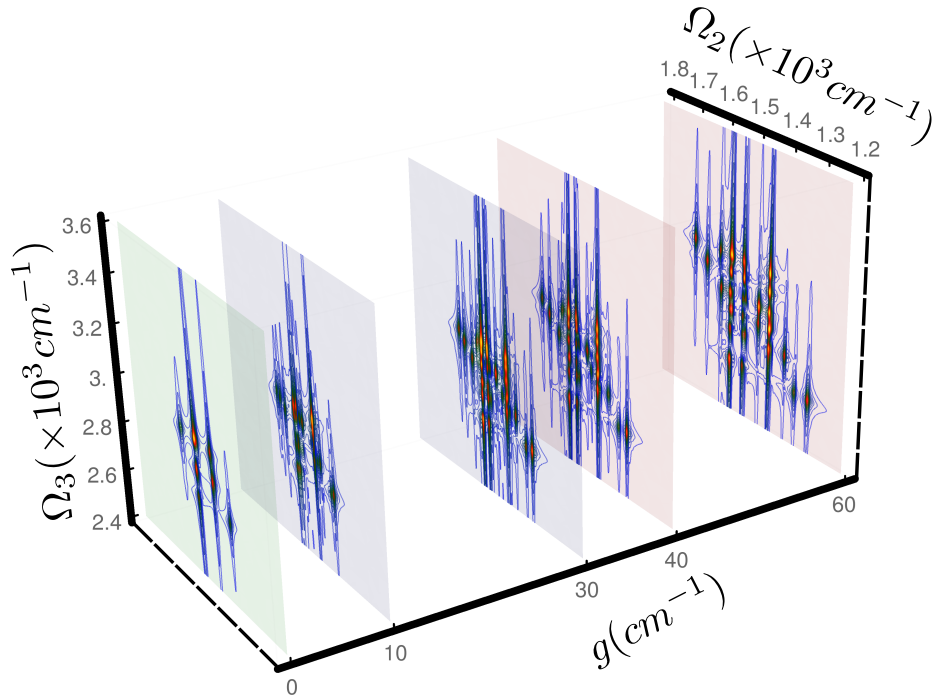


Figure 3.5: Modulus of DQC signal for Amide-I+II vibrations in NMA with varying cavity coupling ($0\text{cm}^{-1} \rightarrow 60\text{cm}^{-1}$). Cavity field vector \mathbf{e}_c is assumed to be mostly parallel to molecular vibrational transition dipole μ_m . Amide-I vibrations (ω_1) is resonant to cavity cutoff frequency $\omega_0 = 1625\text{cm}^{-1}$ and $\omega_2 = 1540\text{cm}^{-1}$. The anharmonicities $\Delta_{11} = 15\text{cm}^{-1}$ and $\Delta_{22} = 11\text{cm}^{-1}$ (Table 3.1).

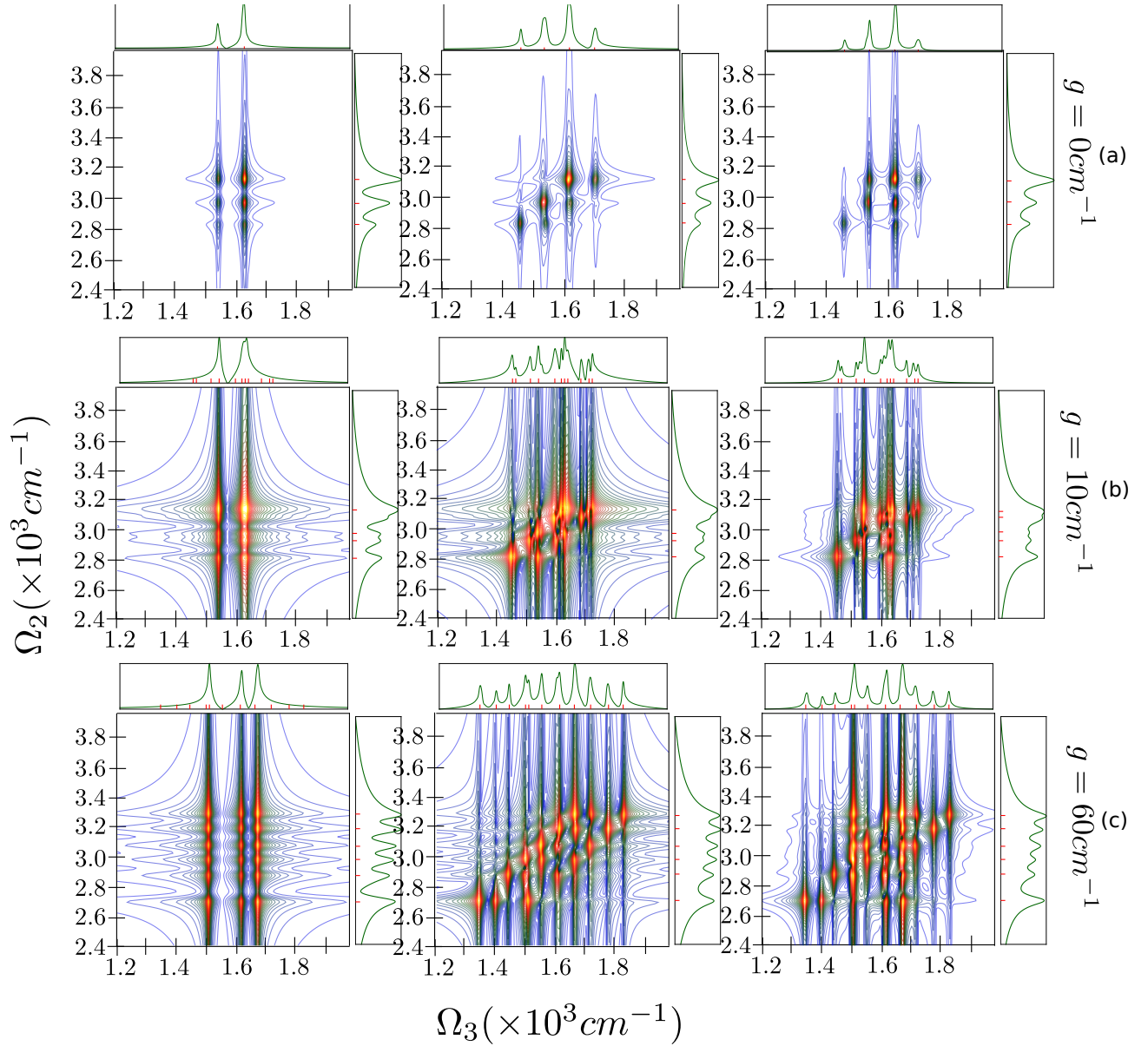


Figure 3.6: DQC signals for Amide-I+II vibrations in NMA using Eq. A.8 and ladder diagrams (Fig. 3.1e): *Columns* : (left-) $|\mathcal{S}_i(\Omega_3, \Omega_2, 0)|$ with resonance at Ω_{e_1g} , Ω_{e_2g} and Ω_{e_3g} ; (middle-) $|\mathcal{S}_{ii}(\Omega_3, \Omega_2, 0)|$ with resonance at $\Omega_{f_1e_3} \approx \Omega_{f_1e_2}$, $\Omega_{f_3e_4} \approx \Omega_{f_4e_2}$, $\Omega_{f_2e_3} \approx \Omega_{f_2e_2}$, $\Omega_{f_1e_1}$, $\Omega_{f_3e_3} \approx \Omega_{f_3e_2} = \Omega_{f_4e_1} = \Omega_{f_6e_3}$, $\Omega_{f_6e_2}$, $\Omega_{f_5e_3}$, $\Omega_{f_2e_1}$, $\Omega_{f_5e_2}$, $\Omega_{f_3e_1}$, $\Omega_{f_6e_1}$, $\Omega_{f_5e_1}$ and (right-) $|\mathcal{S}(\Omega_3, \Omega_2, 0)|$ with respective resonances and cavity couplings (*rows*) (a) 0 cm^{-1} , (b) 10 cm^{-1} , and (c) 60 cm^{-1} along Ω_3 , while peaks at Ω_{f_1g} , Ω_{f_2g} , Ω_{f_3g} , Ω_{f_4g} , Ω_{f_5g} and Ω_{f_6g} along Ω_2 . The linear projections along each axis is shown in green. For simplicity, cavity field vector \mathbf{e}_c is assumed to be mostly parallel to molecular vibrational transition dipole μ_m . Amide-I vibrations (ω_1) is resonant to cavity cutoff frequency $\omega_0 = 1625 \text{ cm}^{-1}$ and $\omega_2 = 1540 \text{ cm}^{-1}$. The anharmonicities are assumed $\Delta_{11} = 15 \text{ cm}^{-1}$ and $\Delta_{22} = 11 \text{ cm}^{-1}$ (Table 3.1)

Chapter 4

Interacting Deformed Molecular Polaritons

In this chapter, modified Double Quantum Coherence (DQC) is derived and a unique measure for effective enhancement of this signal is presented as a function of number of polaritons. This is used to investigate collective effects due to polariton-polariton scatterings. Applications are made for varying number of chromophores (for $N_p \in \{1, 2, \dots, 15\}$) picked from monomer of Light Harvesting Complex II (LHCII). It is shown that polariton-polariton scattering for non-bosonic polaritons could bring the middle polariton branches (MPBs) that are usually embedded deep within so the called "dark-state" to light.

4.1 Introduction

Molecular polaritons, dressed light-molecular exciton quasiparticles, have different optical properties compared to excitons. Over the past few decades there has been extensive theoretical understanding and experimental demonstrations on how the physical [121, 67, 69,

70, 71, 72, 73] and chemical behaviors [53, 81, 74, 122, 78, 77, 55] of exciton are modified in confined optical cavities. Qualitative and quantitative understanding of nonlinear polariton interactions are at the heart of open questions in the field [123, 124, 125]. To lowest order in external electric fields, these nonlinearities manifests themselves as polariton-polaritons scattering [6, 65].

Nonlinear spectroscopic techniques, like double quantum coherence (DQC), can be used to study these nonlinearities such as vibrational anharmonicities, on-site interactions etc [?]. Quasiparticle representation of coherent multidimensional optical signals for molecular polaritons in confined cavity (in both time and frequency domain) has been developed allowing for direct observations of these polariton-polariton scattering terms that are explicitly present in the nonlinear signals [126].

Using a quantum spectroscopic technique called Mollow spectroscopy, Ref. [127] were able to cleanly measure weak nonlinearity even under strongly dissipative conditions. However, this requires a delicate experimental setup and use of quantum light to excite the molecular polaritons [128]. For widely used techniques in multidimensional spectroscopy, coherent pumpings of molecular polaritons introduces several complications in extrating full structural informaion due to several constraints. Loss of strong coupling [129, 130], non-equilibrium thermal excitations [124], phase-space filling factors [131, 132, 133?] (causing the polaritons to deviate from usual bosonic nature) and deviations from Hopfield coefficients [134], to name a few.

We propose compelling remedies to the last two difficulties using theoretical framework to redefine the interacting polariton problem into a interacting deformed polaritons form. Discrepancies due to both phase-filling factors and deviations from Hopfield coefficients are encoded in a single deformation parameter q (described in detail in the main text). This allows us to develop a modified double quantum coherence (DQC), a time-dependent multi-dimensional spectroscopic technique. Using the intensity of this signal as we vary the number

of molecular polaritons, we are able to devise an unique measure for effective enhancement of this signal. This is then used to investigate collective effects due to polariton-polariton scatterings.

To this end, the usual interacting molecular polariton is given by following Hamiltonian [126],

$$H = \sum_i \Omega_i p_i^\dagger p_i + \sum_{i,j} V_{ij} p_i^\dagger p_j^\dagger p_i p_j, \quad (4.1)$$

where, Ω_i is polariton energy of branch i and V_{ij} is polariton-polariton interaction between sites i and j . p_i^\dagger (p_i) are polariton creation (annihilation operators) and follow bosonic commutation relations $[p_i, p_j^\dagger] = \delta_{ij}$. Hamiltonian for interacting deformed polaritons is introduced in next section. Followed by discussion on effects due to these deformations for varying number of optically confined chromophores and possibilities of observation of the middle polariton branches (MPBs) that are usually embedded deep within so the called "dark-state" to light due to polariton-polariton scattering of deformed molecular. We end with concluding remarks.

4.2 Interacting deformed molecular polaritons

We start with the following transformed interacting molecular polariton Hamiltonian with polariton energies $\tilde{\Omega}_i$ for mode i ,

$$\mathcal{H} = \sum_i \tilde{\Omega}_i \hat{\pi}_i^\dagger \hat{\pi}_i + \sum_{i,j} W_{ij} \hat{\pi}_i^\dagger \hat{\pi}_j^\dagger \hat{\pi}_i \hat{\pi}_j, \quad (4.2)$$

and, two-site polariton-polariton interaction quantified by W_{ij} . $\hat{\pi}_i^\dagger$ ($\hat{\pi}_i$) are deformed polariton creation (annihilation operators) with commutator A_i defined as [135, 136],

$$[\hat{\pi}_i, \hat{\pi}_j^\dagger] = \delta_{ij} \left(q_i^{\hat{N}_i} (1 + q) + q_i^{-1} \hat{\pi}_i^\dagger \hat{\pi}_i - q_i \hat{\pi}_i \hat{\pi}_i^\dagger \right) := A_i \delta_{ij} \quad (4.3)$$

$\hat{N}_i (= \hat{\pi}_i^\dagger \hat{\pi}_i)$ is the number operator for mode i , such that, $\sum_i \hat{N}_i = \hat{N}$ gives the total polariton number operator. The dependence of Eqn. (4.3) on \hat{N}_i allows for interesting many body polariton-polariton interaction but it does come with meticulous algebraic transformation. We will present a simple case to illustrate its feasibility restricting \hat{N}_i to doubly excited manifold. The deformed polaritons operators, $\hat{\pi}_i^\dagger$ ($\hat{\pi}_i$), are related to usual polariton operators p_i^\dagger (p_i) by following unitary preserving transformations [136],

$$\begin{aligned} \hat{\pi}_i^\dagger &= p_i^\dagger \sqrt{\frac{[\hat{N}_i]}{\hat{N}_i + 1}} \\ \hat{\pi}_i &= \sqrt{\frac{[\hat{N}_i]}{\hat{N}_i + 1}} p_i. \end{aligned} \quad (4.4)$$

$[\hat{N}_i]$ is the q-analytic form of \hat{N}_i given by,

$$[\hat{N}_i] = \frac{q_i^{\hat{N}_i} - q_i^{-\hat{N}_i}}{q_i - q_i^{-1}} = \cosh(\lambda_i) \sinh(\hat{N}_i \lambda_i), \quad (4.5)$$

and is also valid for q-analog for numbers. We have used $q_i = \exp(\lambda_i)$ for algebraic simplifications needed for expanding over orders of number operator \hat{N}_i . The polariton Fock space

$(\mathcal{F}_p = \otimes^{N_p} |n\rangle_i)$ is spanned by direct product of polariton basis $|n_i\rangle$,

$$|n\rangle_i = \frac{(\hat{\pi}_i^\dagger)^n}{\sqrt{[n]_i!}} |0\rangle_i, \quad (4.6)$$

on ground state $|0\rangle_i$ of mode i . Next we provide mapping procedure to rewrite deformation parameters q_i in terms of already known Hopfield coefficients that are found upon diagonalizing exciton plus photon cavity Hamiltonian. This information alone can provide a smooth transition to formulate nonlinear polariton equations (NPE) as done in [126] for deformed polaritons. To this end, we define following dynamical (in sense of cavity coupling strength) structure factor (\mathbf{f}_i) for mode i . We truncate the metric to incorporate upto doubly excited exciton-polariton manifold to get,

$$\mathbf{f}_i = \begin{bmatrix} -1 & -1 & -1 \\ z & -1 + \alpha_{11}(\bar{\kappa}_i - 2\tilde{X}_i) & -1 + \alpha_{21}(\bar{\kappa}_i - 2\tilde{X}_i) \\ z & -1 + \alpha_{12}(\bar{\kappa}_i - 2\tilde{X}_i) & -1 + \alpha_{22}(\bar{\kappa}_i - 2\tilde{X}_i) \end{bmatrix} \quad (4.7)$$

where, $\alpha_{ij} = n_i^{ex}/n_j$ is the ratio between excitons (n_i^{ex}) and polaritons (n_j) numbers for a single mode optical cavity. Furthermore, z resides in positive integer plane, and, we have defined,

$$\begin{aligned} \bar{\kappa}_i &= \frac{\kappa_i}{2} \tilde{X}_i, \\ \tilde{X}_i &= \sum_j |X_{ij}|^2, \end{aligned} \quad (4.8)$$

for brevity. κ_i which usually incorporates deviation in exciton operators due to Coulomb and Pauli interactions [39, 65], is defined as the ratio $\mu_{ex}^{(2)}/\mu_{ex}^{(1)}$ for exciton transition dipoles of doubly and singly excited states. Of course, all of nonlinear polariton equations can be formulated using techniques done in [126]. The explicit inclusion of number dependent deformation parameters allows for studying cooperative phenomena in molecular polaritons mor simply.

In order to derive expression for \mathbf{f}_i we have used the normalization of Hopfield Coefficients, i.e., $\sum_i |C_i|^2 + \sum_{ij} |X_{ij}|^2 = 1$, which is easily achieved upon polariton transformation discussed in [9] to get Eqn. (4.2) here. Furthermore, utilizing exponential theorem for Fock spaces spanning exciton (\mathcal{F}_e), cavity photon (\mathcal{F}_c) and joined polariton (\mathcal{F}_p) guarantees that such a transformation is unitary and dimensions of \mathcal{F}_p equals that of sum of \mathcal{F}_c and \mathcal{F}_e . Dimensionless parameter λ_i is then defined by,

$$\lambda_i = -\mathbf{f}_i + \mathcal{L}_w(e^{\circ\mathbf{f}_i}), \quad (4.9)$$

where, $e^{\circ\mathbf{f}_i}$ is Hadamard exponent of \mathbf{f}_i and \mathcal{L}_w is the Lambert W function. Beside providing computational convenience in calculation of deformation factors $\lambda_i = \text{Log}(q_i)$, the metric \mathbf{f}_i contains following topological information for $f_{i,jk}$ (with indices j and k running from 0 to 2, and identified $f_{i,jk} \mapsto f_{jk}$ to avoid redundancy): a) f_{00} polariton ground state, b) f_{01} polariton (photon) reservoir, c) f_{02} , biphoton reservoir d) f_{10} exciton reservoir, e) f_{11} exciton-polariton, f) f_{12} bipolariton, g) f_{20} biexciton reservoir, h) f_{21} biexciton-polariton, and i) f_{22} bipolariton. For rest of this paper we will focus on *exciton – polariton* (or f_{11}) term only and will use short hand $\lambda_i \equiv \lambda_{i,11}$ for simplicity. It is easy to show that for $\kappa_i = \sqrt{2}$, $\lambda_i = 0$ and $q_i \rightarrow 1$. This consequently makes commutator A_i (c.f. Eqn. (4.3)) a unity and all the equations in [126] are recovered exactly.

Simple algebra can show that the two site polariton interaction terms (W_{ij}) in Eqn. (4.1) connect to V_{ij} in Eqn. (4.2) via,

$$W_{ij} = \tilde{V}_{ij}\{(q_i + 1) + \text{Log}[q_i] + q_i \text{Log}(q_i) + q_i^{-1} - q_i\}. \quad (4.10)$$

Where we have expanded $q_i^{\hat{N}_i}$ to first order in \hat{N}_i , and $q_i > 0$. The condition $q_i > 0$ assures that polaritons are deformed bosons and not fermions. Furthermore, it avoids singularity in W_{ij} at $q_i = 0$ preventing from infinite particle interaction coupling bounding $W_{ij} < \infty$. This is always valid in the energy regimes we work with.

Usually, $\kappa = \sqrt{2}$ is assumed which is equivalent to treating interacting polaritons are weakly interacting bosonic gases. The expression in Eqn. (4.10) correctly reduces to $W_{ij} = 2V_{ij}$ equivalent to what is done in deriving nonlinear polariton equations in [65, 126].

upon expanding to third order in field that enters through the following interaction term, $H_{int} = \sum_i (\mu_i^{pol} \cdot E(\omega, t) + h.c.)$, we notice that double quantum coherence (DQC) signal is altered. This modification can be attributed to the change in polariton-polariton scattering via W_{ij} . DQC signal in frequency domain for deformed polaritons is thus given by,

$$\begin{aligned} S_{\mathbf{q}}^{DQC}(\bar{\Omega}_3, \bar{\Omega}_2, \bar{\Omega}_1) &= - \left(\frac{i}{\hbar}\right)^3 \sum_{ijkl} E_k^*(\Omega_l - \omega_s) E_l(\Omega_k - \omega_3) E_j(\Omega_j - \omega_2) E_k^*(\Omega_i - \omega_1) \\ &\times \left[\Gamma_{kl,ji}^q(\bar{\Omega}_2) F_{ji}(\bar{\Omega}_2) - \Gamma_{kl,ji}^q(\bar{\Omega}_3 + \Omega_k + i\gamma_k) \right. \\ &\times \left. F_{ji}(\bar{\Omega}_3 + \Omega_k + i\gamma_k) \right] G_l^{(1)}(\bar{\Omega}_3) G_j^{*(1)}(\bar{\Omega}_1) G_k^{*(1)}(\bar{\Omega}_2 - \bar{\Omega}_3). \quad (4.11) \end{aligned}$$

Where we have used $E_k(\omega) = \mu_k^{pol} E(\omega)$ for simplicity, ω_s is frequency of the local oscillator, and introduced a phenomenological dephasing γ_k . The one-polariton Green's functions for

mode i is given by,

$$G_i^{(1)}(\omega) = (\omega - \tilde{\Omega}_i + i\gamma_i)^{-1}. \quad (4.12)$$

Both free one and two polariton propagators $G_k^{(1)}(\omega)$ and $F_{nm}(\omega)$ have inconsequential modification in zero point energy (from factor $\frac{1}{2} \rightarrow \mathcal{L}_w(1/e)$). The polariton-polariton scattering $\mathbf{\Gamma}^q(\omega)$ is given by,

$$\mathbf{\Gamma}^q(\omega) = (1 - W_{mn}F_{nm}(\omega))^{-1}W_{mn}. \quad (4.13)$$

One straight forward advantage of rewriting Eqn. (4.2) in terms of Eqn. (4.1) with deformed commutation relations ($A_i \neq 1$, c.f. Eqn. (4.3)) is explicit tractability of the parameter regimes (for cavity coupling g and κ_i) for studying different nonlinear effects as we increase number of chromophores in the optical cavity. We next elaborate on some of those effects using parameters given in Table. 4.1. In all of the numerical calculations that follows, we have used parameters for N_{ex} chromophores of the Light Harvesting Complex II (LHCII) coupled to single mode optical cavity with parameters in Table.4.1. Before proceeding we briefly mention what we mean when we use N_p . It indicates that there are N_p-1 molecular chromophores in single mode optical cavity with energies corresponding to ϵ_i for $i \in \{1, \dots, N_p - 1\}$ from the list of excitons mentioned earlier. A typical DQC signal is shown in 4.1

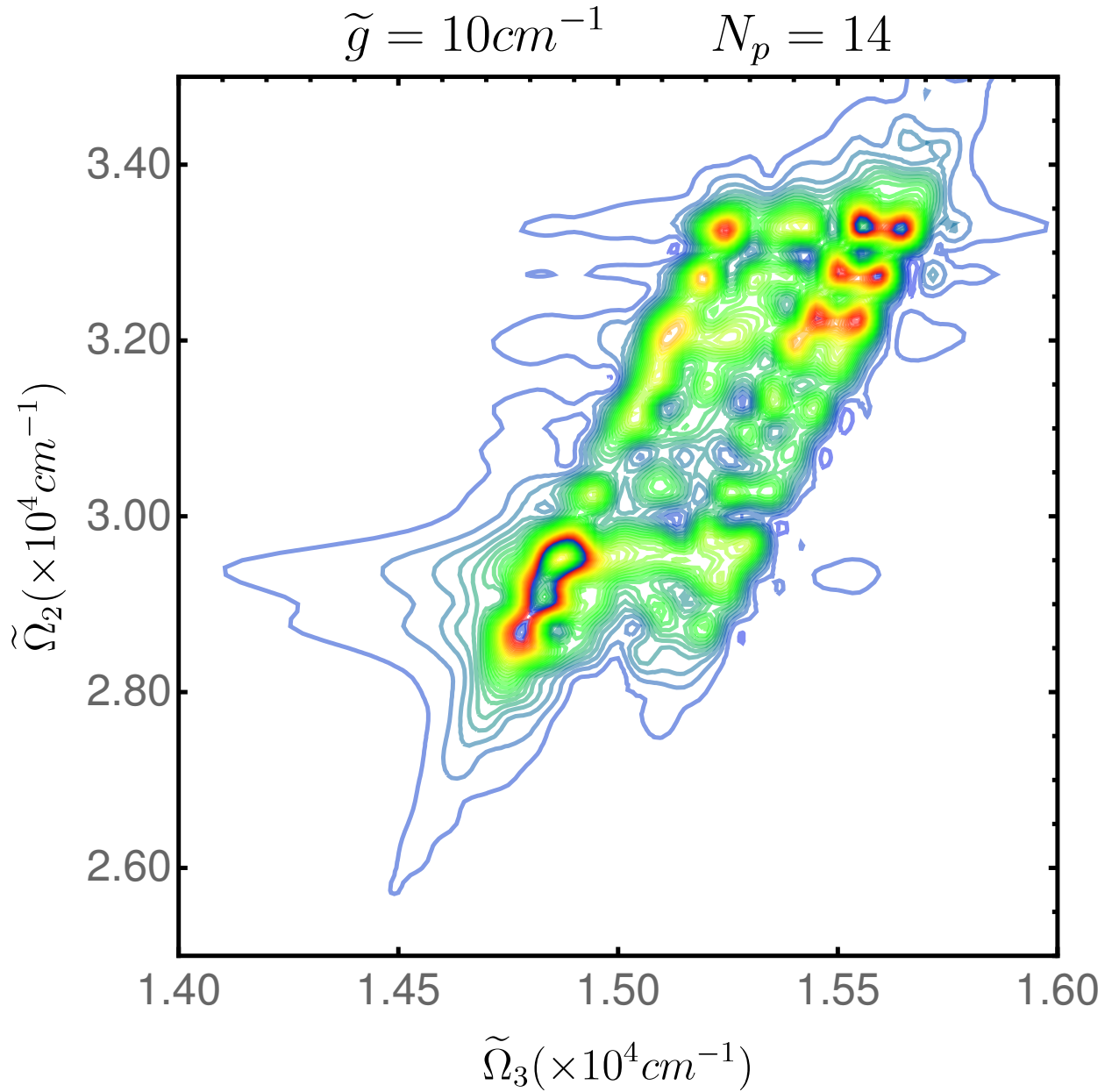


Figure 4.1: Typical double quantum coherence (DQC) using Eqn. (4.11) using parameters in Table 4.1 for light harvesting complex II (LHC-II) for coupling strength of $10cm^{-1}$.

Table 4.1: Parameters used in this paper. $\epsilon_n^{(0)}$ energies of n isolated chromophore from Light Harvesting Complex (LHCII), μ_a and μ_b are transition dipole moments for Chlorophyll a (Chla) and b (Chlb) respectively. $\epsilon_{ord}^{(0)}$ provides the ordering of energies [1].

$\epsilon_{ord}^{(0)}$	chla,chla,chla,chla,chla,chla,chlb,chlb chlb,chla,chla,chla,chlb,chlb,chlb
$\epsilon_n^{(0)}$ (in cm^{-1})	14850, 14860,14780,14930,14960,15175,15635 15415,14870,14920,1555,15395,13505
μ_a (in D)	4.0
μ_b (in D)	3.4

4.3 Effects due to deformations of molecular polaritons

We start this section by exploring an obvious advantage of using Eqn. (4.2) to study interacting molecular polaritons formed in organic optical cavities. In Fig. 4.2 we present variation of average deformation defined by, $\bar{q}_{N_p} = \frac{1}{N_p} \sum_i^{N_p} q_i$ with $q_i = \text{Log}(\lambda_i)$ for λ_i defined in Eqn. (4.9). We observe that for typical value of $\kappa_i = \kappa = \sqrt{2}$ (marked as dashed black line in Fig. 4.2) that justifies the Frenkel exciton model used to study molecular aggregate becomes bosonic, we observe that $N_p \bar{q} \sim 1$. This implies that N - dependent factor on polariton interactions vanishes (i.e., $W_{ij} = 2V_{ij}$). Consequence of this is that many body effects that manifest due to interacting polaritons cannot show cooperative effects as we increase the number of chromophores in the cavity and any enhancements in the singals is purely due to power play between radiative and non-radiative decays of molecular polaritons [79, 137, 138, 139].

For $N_p = 2$, that is when one single molecule is placed in a single mode optical cavity, overall deformation may only occur at very low cavity coupling strengths, where a complete mixing of cavity and excitons mode is possible similar to molecule interacting with single optical phonon [95]. Similar effects are seen at high κ . As we increase the number of chromophores, we see that certain values ($\kappa = 0.36, 1.2$) are more likely to give interesting variations in deformation parameters and hence rich structural information for a wide range of cavity coupling strengths

($200\text{cm}^{-1} < g < 600\text{cm}^{-1}$). For $N_p = 15$ we clearly see that assuming $\kappa = \sqrt{2}$ gives $N_p \bar{q}_i \sim 1$ for each polariton branch suggesting that such a model fails to properly detect many body effects and any variations in nonvanishing nonlinearities of molecular polaritons that are not purely due to cavity mediated photon mixing to molecular excitons. We can see that understanding \bar{q} (and q_i indirectly) allows for a robust theoretical prediction of parameter regimes (for instance red dashed lines in Fig. 4.2) for maximal structural control and information extraction using nonlinear spectroscopic measures. Inverting this, could allow us a way for control and predictions of κ or molecular polaritonic dipole transitions for given cavity coupling strength and aggregate size. As mentioned earlier, κ_i contains

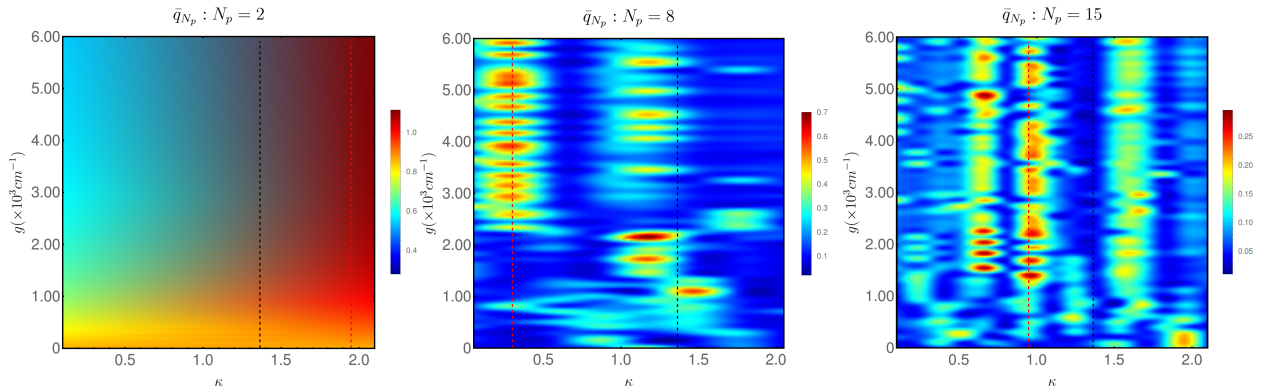


Figure 4.2: Average deformation $\bar{q} = \frac{\sum q_i}{N_p}$ as function of κ and cavity coupling strength g for various polariton numbers N_p : a) $N_p = 2$; b) $N_p = 8$; and c) $N_p = 15$. The expression for q_i is calculated using Eqn. (4.9) and $\lambda_i = q_i$. The dashed black lines are at $\kappa = \sqrt{2}$ where $N_p \bar{q} \sim 1$. and Eqn.(4.1) to Eqn.(4.2) apart from factor of 2. Dashed red lines show possible values of κ where more interesting structural information can be extracted for varying coupling strengths.

information about Pauli and Coulomb interactions, thus being able to indirectly measure q_i does not provide direct measure for those interactions. Nevertheless, the fact that we are able to establish connection between total polariton number and deformations q_i could further interesting insights into cooperative phenomena in molecular polaritons. To that end, we study enhancements in DQC signals (Eqn. (4.11)) next.

4.3.1 Signal Enhancement

Molecules confined in optical cavity under specific conditions allows for cooperative enhancements of signals, for instance, enhancements in spontaneous signals due to superradiance [140]. Collective interactions of atoms, molecules, or macromolecules to the vacuum mode of the optical cavity may enhance signals as well [141]. Typically, enhancements due to collective nature of molecular polaritons compete with the dephasing processes (either due to cavity decay or radiative molecular decay) in molecular cavity. How these radiative and non-radiative decays change with increasing (Huang-Rhys) parameters and bath modes have recently been studied [137]. It has been predicted that for molecular polaritons, strong coupling to cavity mode could decouple their lowest lying polariton branches with vibrational bath available to them. For our purposes, we will assume that the radiative decay (\sim cavity decay rate $\sim 10fs$) scales as $N_p(N_p - 1)$ for a single mode optical cavity. The non-radiative processes in molecular polaritons decays due to individual molecules and their baths typically is of higher order ($\sim ps$) [137]. In nonlinear signals, there may also be enhancements due to nonlinear interactions within molecular polaritons, in particular polariton-polariton interactions and must be incorporated in quantifying third order signal enhancements. To this end, we define following enhancement coefficient (\mathcal{Q}) that is proportional to the intensity of DQC (c.f. Eqn. (4.11)). After a bit of algebra, and assuming radiative processes (γ_r) scales as $N_p(N_p - 1)$ and non-radiative process (γ_{nr}) scales with temperature T as $\eta T \gamma_r$ for parameter $0 < \eta < 1$, we arrive at the signal enhancement for individual modes i ,

$$\mathcal{Q}_i = \frac{\gamma_r^3}{\gamma_{nr}^2} \sum_j \frac{W_{ij}}{\gamma_{nr} - iW_{ij}} = \frac{(1 + q_i) \{(N_i - 1)(N_i - 1)(N_i + q_i - N_i q_i + N_i q_i \text{Log}(q_i))\}}{\sqrt{((N_i - 1)N_i q_i)^2 + (1 + N_i)(N_i + q_i - N_i q_i + N_i q_i \text{Log}(q_i))}} \quad (4.14)$$

where, we have implicitly expanded the W_{ij} in polariton basis. Thus, N_i now is the polariton number of specific mode i . Summing over all indices gives total enhancement (i.e., $\mathcal{Q} =$

$\sum_i \mathcal{Q}_i$ that depends on total polariton number ($N_p = \sum_i N_i$). In Fig.4.3, we present \mathcal{Q} for lower (LPB), middle(MPB) and upper(UPB) polariton branches. The MPB is selected by $\text{Floor}[n/2]$ (for instance is 0, when $N_p = 2$, implying no middle polariton branch) which becomes 0 for single molecule in optical cavity. For both LPB and UPB, we see more signal enhancements along even number of polaritons. This can be explained as follows: Out of N_p polariton branches 2 of them are so called "bright" states polaritons due to higher mixing of cavity photon components or high transition dipoles. They are also the LPB and UPB. The remaining $N_p - 2$ states are "dark" in a sense that they have either small photon mixing or small transition dipole moments and thus are spectroscopically less visible. For even N_p , there are even number of bright and dark states, thus allowing maximal distribution of photon components between LPB and UPB (thus having higher signal enhancements) due to almost complete destructive interference among the remaining $N_p - 2$ states. For odd N_p some of the photonic components are bound to reside on MPB causing diminished signal.

Furthermore, we predict that signal would be enhanced when $N_p = 15$ (equivalent to LHCII complex in single mode optical cavity) around $g = 150\text{cm}^{-1}$. Unlike LPB, for $N_p = 15$ (\equiv LHCII) we predict that the signal would be almost always be enhanced for $g < 300\text{cm}^{-1}$ and sporadic after allowing us to pick proper cavity coupling regime to control aggregate properties due to polariton nonlinearities.

The enhancement signals in the MPB provides for a more peculiar case. The MPBs lie deep in the "dark-states" submanifold, thus such signal enhancements would mean they could in principle be visible under certain suitable conditions ($\kappa = 0.9$). This prediction does not provide sufficient conditions to claim spectral resolution of all MPBs but speculates that some MPB can be observed in third order signals due to many body interactions. To study such possibilities and know that polariton transition dipoles play an important interfering role in signal visibility we next propose an effective enhancement measure ($c\mathcal{Q}$).

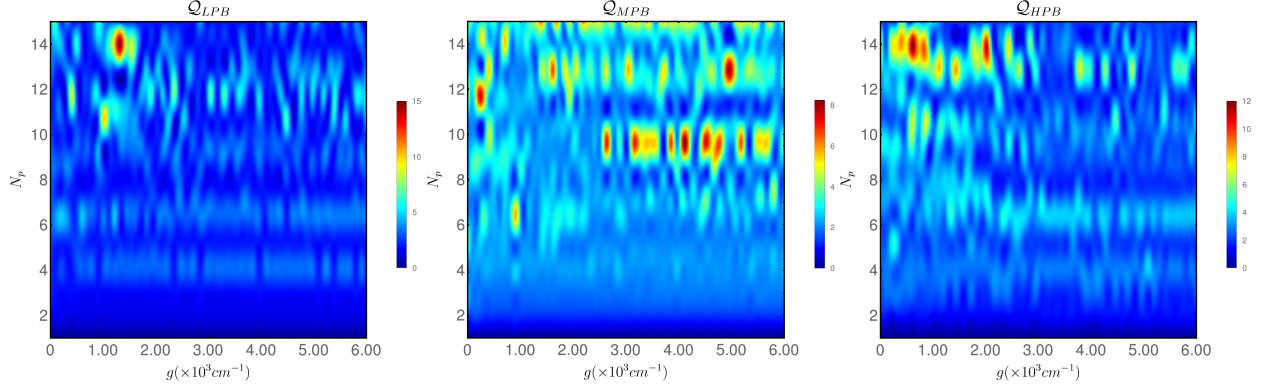


Figure 4.3: Signal enhancements, \mathcal{Q} (using Eqn. (4.14)) for DQC for $\kappa = 0.9$ for varying cavity coupling strength g vs increasing chromophore number in optical cavity is showed for a) Left: Lower Polariton Branch (LPB), b) Middle Polariton Branch (MPB) and c) Upper Polariton Branch (HPB) is done. (see text for details)

4.3.2 Effective Enhancement

We define effective enhancement ($c\mathcal{Q}$) incorporating transition dipole (μ_{pol}) interference as,

$$c\mathcal{Q} = \text{Log} \left(\left| \frac{1 - \mathcal{Q}}{\mu_{pol}} \right|^2 \right). \quad (4.15)$$

We calculate $c\mathcal{Q}$ for same parameters as for \mathcal{Q} and using parameters in Table. 4.1. As expected, we see effective enhancement still there for even number of modes for LPB in Fig. 4.4, however the isolated enhancement at lower cavity coupling strength for full LHCII disappears and better signal enhancements agreeing with typical values for molecular aggregates in optical cavities [74]. Barring few isolated cases, the effective enhancement show similar trend for UPB. There are some effective enhancements for MPB as well for either smaller number of chromophores in at low cavity coupling strength because of more homogeneous mixing of photonic components in the such polaritons. Among MPBs, depending upon our choice, the effective enhancement of the signal varies for larger number of chromophores. From Fig. 4.4 (c) and (d) we would possibilities of spectroscopic detection of these states

bringing them on same level as the “bright” states. Not only that, the logarithmic plot of the differences between enhancements of the two MPBs (MPB and MPB1) show that even these states can be detected from the dense MPB submanifold for appropriate parameter regimes $\kappa = 0.9$ allowing for deformed polariton interactions. This could pave an interesting way to detect “dark” polaritons which relies purely on many-body effects in molecular polaritons unlike studied before for vibronic polaritons [138]. To further illustrate the effects of deformation on spectroscopic signals, we next dissect the polariton-polariton interactions $V_{ij} = W_{ij}|_{q=1}$ and W_{ij} , followed by an analysis of the polariton-polariton scattering matrices $\Gamma(\omega)$ for varied aggregate size and cavity coupling g .

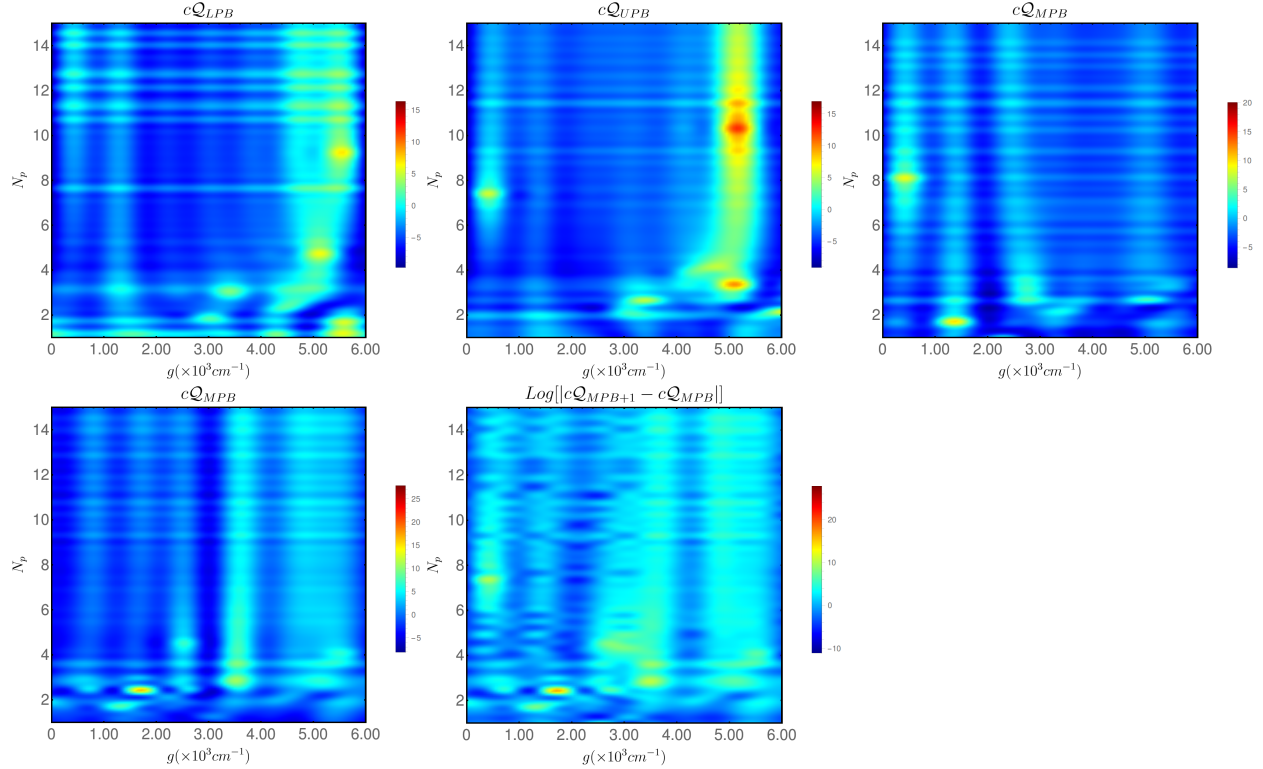


Figure 4.4: Effective signal enhancement cQ (using Eqn. (4.15)) for DQC for $\kappa = 0.9$ for varying cavity coupling strength g vs increasing chromophore number in optical cavity is showed for Top Row: Lower Polariton Branch (LPB, Left), b) Upper Polariton Branch (UPB, Middle) and c) Middle Polariton Branch (MPB, Right); Bottom Row: Middle Polariton Branch (MPB1, Left), and $\text{Log}(|cQ_{MPB1} - cQ_{MPB}|)$ are done. (see text for details)

4.3.3 Polariton-Polariton Scatterings

Polariton-polariton scattering matrices can be thought of as complex two-polariton proper self energy terms. The real part contributes to the energy shift and the imaginary to the pure dephasing associated to them. The poles of these matrices contain information regarding resonances of doubly excited polaritons. Thus exploring structural variations of these matrices at changing cavity coupling strengths and deformation parameter q_i for a chosen $\kappa (= 0.9)$ may provide intuitive and interesting physical insights into nonlinear polariton processes that often dictate nonlinear signals. Utilizing the local nature of polariton operators and their commutators (as A_i is defined with single index) helps us reduce the dimensionality of polariton-polariton interactions and scattering. Physically, they are defined with four indices, two incoming and two outgoing polariton branches, i.e., they are defined with indices mn, kl but we identify the indices such that $mn, kl \mapsto mn, mn$ and two indices mn are sufficient to study essential physics. In the Figures (4.5–4.8) presented in this section, we have only shown mm, nn or cases where two polaritons from site m interact and scatter to two polaritons at site n . This can be equivalently seen as the trace of the tetradic polariton-polariton interaction and scattering tensors. We first discuss two-site polariton interactions W_{ij} which under the limit $q \rightarrow 1$ goes to $2V_{ij}$.

In Fig. 4.5, we present polariton couplings (unnormalized due to color scaling functions which is used for structural illustration) for varied number of chromophores in a single optical cavity. A general trend of positive coupling interactions ($V_{ij} > 0$, red) is observed along the diagonal implying that on-site interactions are repulsive, while nearest neighbor interaction along the diagonal can become attractive ($V_{ij} < 0$, blue). Also, sites farther barely couple with each other. Compared to bosonic case (top row, $q = 1$), we can see (in bottom row) that deformation diffuses some of the strongly repulsive interactions by paying some energy due to many body interactions and could possibly be a reason for observed Feshbach resonance in molecular polaritons [87, 142]. The trend becomes clearer as we increase N_p to 15. At low

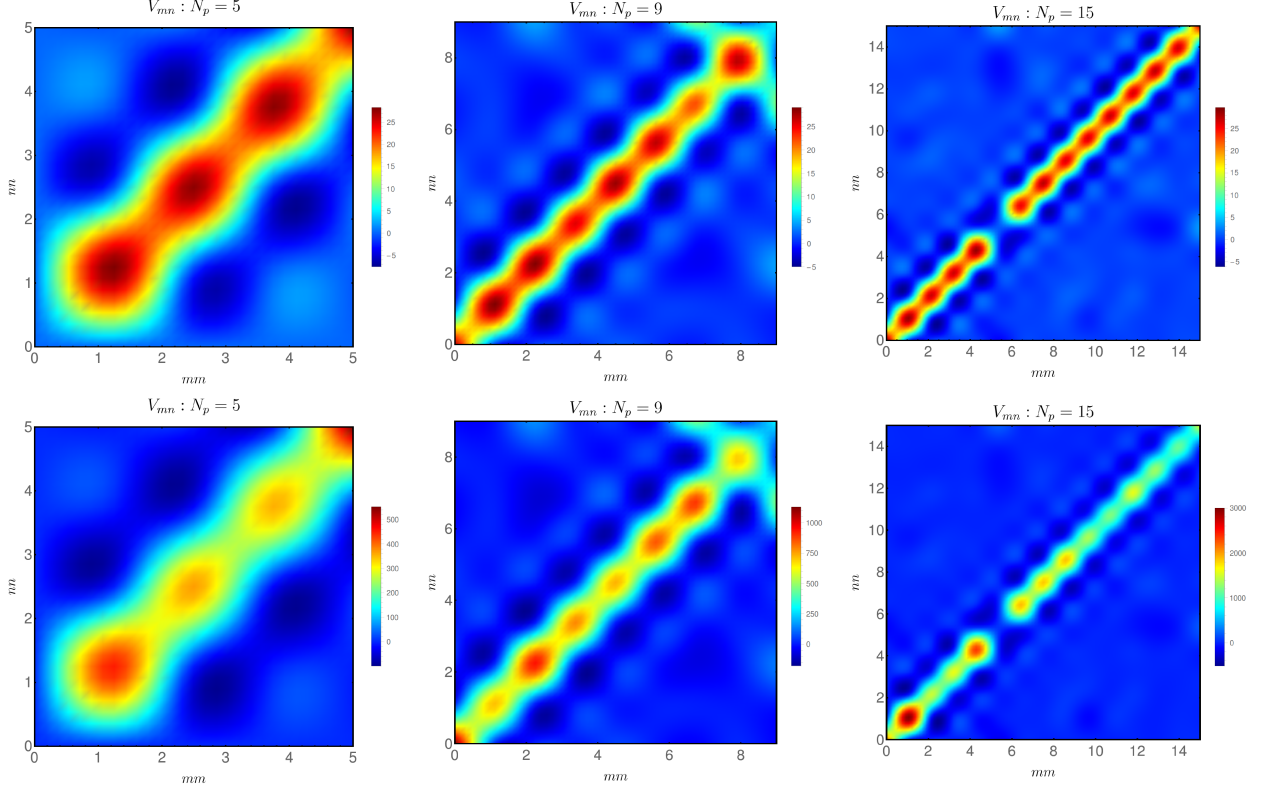


Figure 4.5: Polariton-Polariton interactions varying number of chromophore using Eqn.(4.10). Top Row (for $\kappa = \sqrt{2}, q = 1$) a) $N_p=5$,b) $N_p=9$,a) $N_p=15$; Bottom Row (for $\kappa = 0.9, q \neq 1$) a) $N_p=5$,b) $N_p=9$,a) $N_p=15$ at $g = 0cm^{-1}$. See text for details.

cavity coupling ($g \sim 0cm^{-1}$) for full LHCI ($N_p = 15$), when the cavity photon is chosen to be quasi-resonant with frequency of exciton $\epsilon_5^{(0)}$ from Table. 4.1, seen as mode 6 in Fig. 4.5, we see no effective interactions between these modes. This is because the cavity photon creates polariton degenerate with mode 6. And due to the excitonic Hopfield coefficient being ~ 0 for this state allows for vanishing interactions at no coupling to cavity. This restriction is relieved when cavity coupling is increased and we see appearances of repulsive interactions at mode 6 in both $\kappa = \sqrt{2}$ and $\kappa = 0.9$.

For coupling $g = 150cm^{-1}$ (Fig. 4.6), general trend remains same except for the case mentioned earlier. For $N_p = 9$ we can see more off diagonal interactions suggesting that system becomes more delocalized. The presence of deformation smears out some of the on-site repulsive interactions and make them more attractive. This could mean that, by changing the

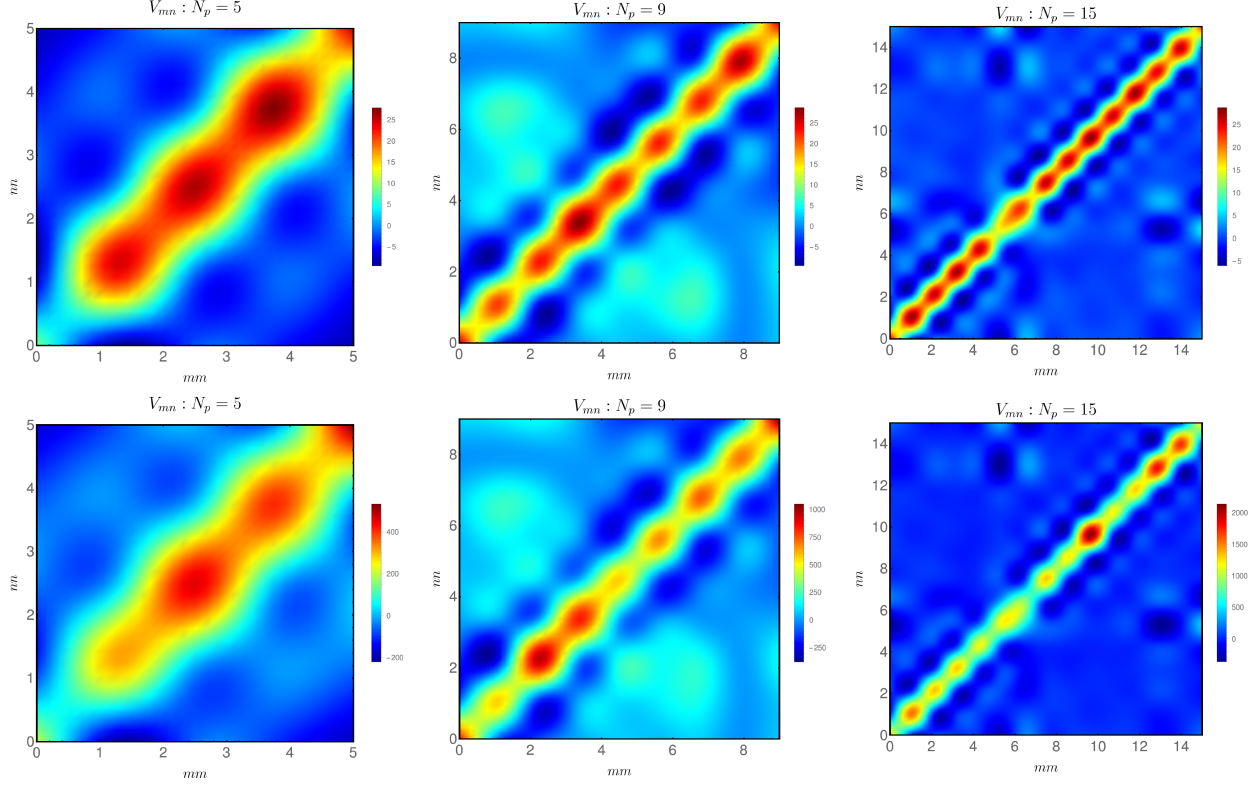


Figure 4.6: Polariton-Polariton interactions varying number of chromophore using Eqn.(4.10). Top Row (for $\kappa = \sqrt{2}, q = 1$) a) $N_p=5$, b) $N_p=9$, a) $N_p=15$; Bottom Row (for $\kappa = 0.9, q \neq 1$) a) $N_p=5$, b) $N_p=9$, a) $N_p=15$ at $g = 150cm^{-1}$. See text for details.

ratio between $\mu_{ex}^{(2)}/\mu_{ex}^{(1)}$ we can control electronic anharmonicities to our advantage. Next we discuss scattering events with ultrafast scattering time $\tau_2 - \tau_1 = 1.5fs$ which is equivalent to $\sim 30000cm^{-1}$ (Fig. 4.7). This is a typical value for doubly excited polariton manifold and has been used for illustrative purposes.

At no cavity coupling $g = 0cm^{-1}$, the effects due to polariton deformations are insignificant for $N_p = 5$ and 15 except for nodal localizing the scattering events. For instance, for $N_p = 5$; most of the scattering happens between modes 5 and 1, with it being more localized when $q_i \neq 1$ for $N_P = 5$. Case of $N_p = 9$ shows more interesting scattering processes suggesting most of modes could scatter to each other again suggesting delocalization as we saw in Fig. 4.6. For LHCI monomer ($N_p = 15$) confined in single mode optical cavity, only mode 4 scatter with frequency close to 30000 suggesting $(4W_{ij} = 30000cm^{-1} - 2(14930cm^{-1}) = 140)$.

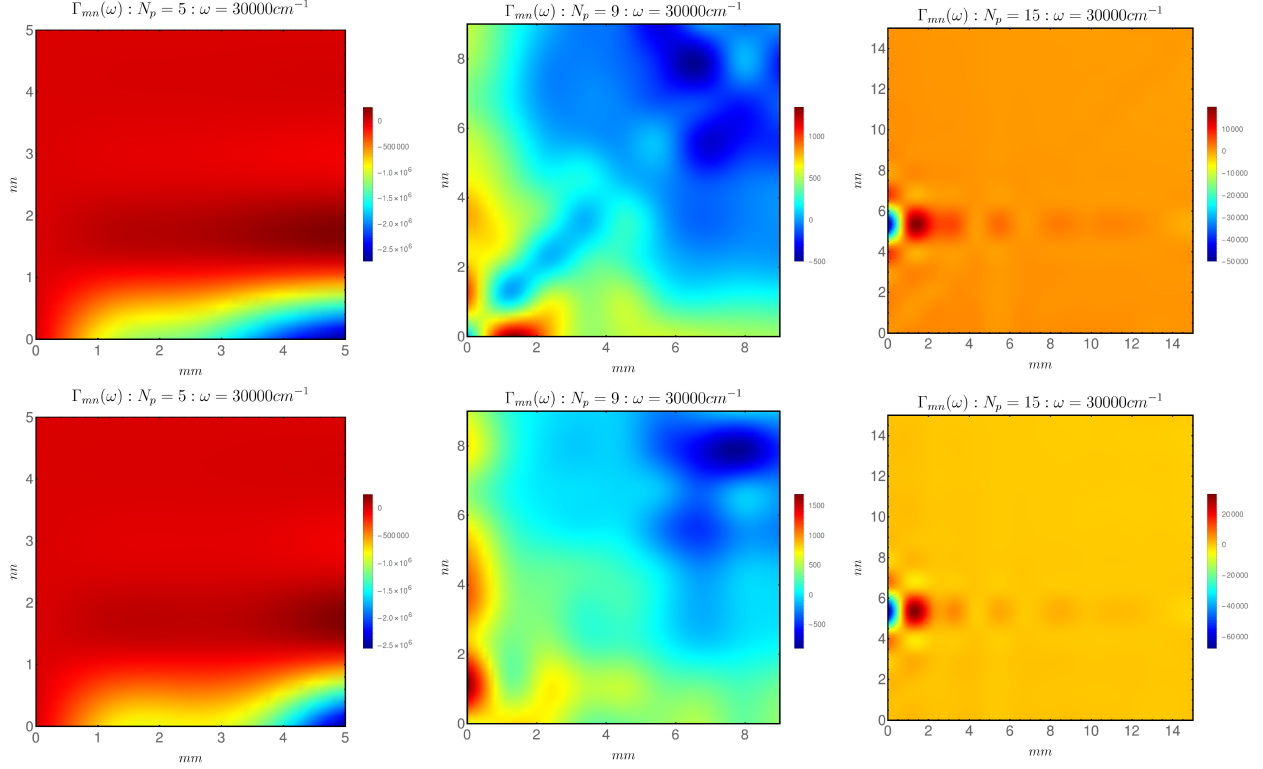


Figure 4.7: Polariton-Polariton scattering $\Gamma(\omega)$ at typical chromophore bipolariton eigenenergy (Chlb) $\omega = 30000\text{cm}^{-1}$ for varying number of chromophore using Eqn.(4.13). Top Row (for $\kappa = \sqrt{2}, q = 1$) a) $N_p=5$, b) $N_p=9$, a) $N_p=15$; Bottom Row (for $\kappa = 0.9, q \neq 1$) a) $N_p=5$, b) $N_p=9$, a) $N_p=15$ at $g = 0\text{cm}^{-1}$. See text for details.

As we tune the cavity coupling to about 150cm^{-1} we see more of polariton modes scattering with that scattering time $\tau_2 - \tau_1$ of 1.5fs both for $N_p = 5$ and 9 . Deformation, again, scattering matrix switches signs again causing redshift in energy of bipolariton to blueshift, for some modes. One could say that deformation mediates, otherwise impossible interactions, due to many-body effects. These effects seems to break down for large $N_p = 15$. This would mean that scattering events are very localised for LHCII. Furthermore, changing coupling strengths even slightly $0\text{cm}^{-1} \rightarrow 150\text{cm}^{-1}$ can allow for particles to scatter from $41 \mapsto 14$ at ultrafast scattering timescale ($\sim 1.25\text{fs}$) while changing parity. Since we have plotted only the real part of the scattering matrix ($\Re : \Gamma(\omega)$) parity change implies red to blue shift in doubly excited polariton manifold. A signature of thus formed molecular polaritons being purely Frenkel type [73].

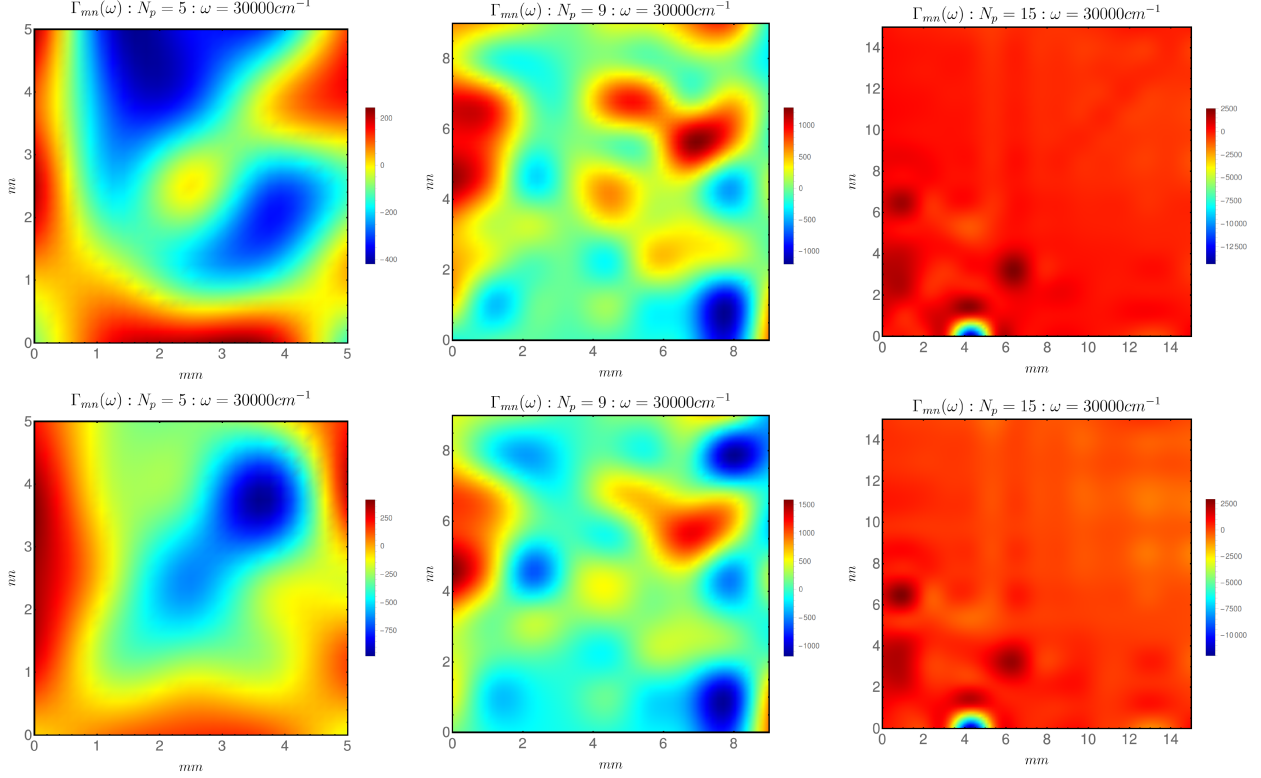


Figure 4.8: Polariton-Polariton scattering $\Gamma(\omega)$ at typical chromophore bipolariton eigenenergy (Chlb) for $\omega = 30000cm^{-1}$ for varying number of chromophore using Eqn.(4.13). Top Row (for $\kappa = \sqrt{2}, q = 1$) a) $N_p=5$,b) $N_p=9$,a) $N_p=15$; Bottom Row (for $\kappa = 0.9, q \neq 1$) a) $N_p=5$,b) $N_p=9$,a) $N_p=15$ at $g = 0cm^{-1}$. See text for details.

4.4 Concluding Remarks

Expressing interacting molecular polaritons as Eqn. (4.1) with commutator A_i (Eqn. (4.3)) allows for a careful monitoring of polariton-polariton coupling terms (Eqn. (4.10)) as a function of polariton number. It is a simple yet robust theoretical framework to study molecular polaritons ranging from weakly to strongly interacting cases. Here we restrict ourselves to weakly interacting regimes, thus allowing use Bethe-Salpeter equations in finding the two-polariton scattering matrices. Third order response functions derived for deformed polaritons, namely DQC (Eqn. (4.11)), contains polariton-polariton scattering matrices.

Using the DQC signal, we have derived a closed form expression for polariton particle number dependent effective enhancement, cQ (Eqn. (4.15)). We use this to predict that under certain

conditions ($\kappa = 0.9$) one can detect dense MPB submanifold that lie deep in so called "dark" states for wide range of cavity couplings (Fig.. 4.4). The effects due to phase-space filling factor (ϕ) and deviation from the Hopfield coefficients are already baked in Eqn. (4.15) through Eqn. (4.14) that depends on deformations (q_i). q_i for each polariton branches is found by taking natural logarithm of λ_i (Eqn. (4.9)) and contains the term $\bar{\kappa}_i$ (Eqn. (4.8)). It is $\bar{\kappa}_i$ that actually encodes information regarding phase-space filling factor and deviation from Hopfield coefficients. It (Eqn. (4.8)) has following interpretation: κ_i term in $\bar{\kappa}_i$ is related to the phase-space filling factor (ϕ) directly, i.e., for each polariton mode i , $\phi_i = 2 - \kappa_i^2$ [39]. This is equivalent to $\phi = \phi_i = 1.19$ for our case ($\kappa_i = \kappa = 0.9$).

Similarly, the term $\tilde{X}_i = \sum_j X_{ij}$ in Eqn. (4.8) contains the deformed Hopfield coefficients (X_{ij}), their absolute squares are related to usual Hopfield coefficients (x_{ij}) and cavity photon number (n^a) by,

$$\begin{aligned} |X_{ij}|^2 &= \left| \frac{1 - 2\phi_i(3 - 2n^a)}{1 + 2g(1 - \phi_i n^a)} x_{ij} \right|^2 \\ &= \left| \frac{1 - 2\phi_i}{1 + 2g(1 - \phi_i)} x_{ij} \right|^2 \quad \text{when } n^a = 1 \end{aligned} \quad (4.16)$$

Thus calculating cQ for varying number of chromophores confined in a tunable single mode optical cavity provides a simple measure to study effects of both phase-space filling factor (ϕ) and deviations from Hopfield coefficients which is unavoidable during coherent pumping of molecular polaritons [134].

We further predict that, for ultrafast polariton-polariton scattering (1.15fs) the scattering processes localizes as we increase the number of chromophores in the cavity (Figs. 4.7-4.8) for both vanishing and weak cavity coupling regimes. Localization of interactions between isolated modes for deformed molecular polaritons could also be used to study direct energy transfer pathways in large macromolecules in optical cavities. Furthermore, change in parity

of the nonlinear coupling as we go from no (Fig. 4.6) to weak coupling (Fig. 4.5) could be used to explain optical Feshbach resonance observed in molecular polaritons [87, 142]. Further more localization of polariton-polaritons interactions only to some polariton modes (Fig. 4.5) should allow for easier measure of these resonance.

We have only presented the results for scattering matrices and used DQC signal to predict effective enhancements. Explicit calculations of DQC signals can be done and their temporal evolution (under coherent limit) be studied in details but, however, essential physics is contained in the polariton-polariton scattering matrices discussed in this work. An extension to this theory to incorporate incoherent processes with explicit polariton number as a parameter could provide for a more complete definition of effective enhancements ($c\mathcal{Q}$).

All operators are expanded in polaritonic Fock space (\mathcal{F}_p) and only static cavity couplings are considered. \hat{N}_i that enter in Eqn. (4.3) implicitly contains information about cavity couplings via the polariton operators ($\hat{\pi}_i$ and $\hat{\pi}_i^\dagger$). If we have time-dependent cavity coupling ($g(t)$, instead of g) then \hat{N}_i is equipped with time-dependence. Use of coherent basis for deformed polaritons then could provide a more intuitive understanding of the effects on third order signals and effective enhancements for time dependent coupling cases without changing the formalism drastically [143].

Finally, if the size of the macromolecules becomes comparable to the wavelength to the cavity length that confines them, then the usual dipolar form of cavity field's (\vec{E}_c) to macromolecular coupling, i.e., $g \sim \vec{\mu} \cdot \vec{E}_c$ would break down. A more fundament (minimal coupling) approach would be required to then define cavity coupling (\tilde{g}_{mc}) in terms of canonical current density $\mathbf{J}(\mathbf{r})$ and cavity vector potential $\mathbf{A}_c(\mathbf{r})$, $\tilde{g}_{mn} = \mathbf{J}(\mathbf{r}) \cdot \mathbf{A}_c(\mathbf{r})$ to encapsulate \mathbf{r} -dependence carefully [144]. A more rigorous approach would then be required to map Eqn. (4.1) to a case of \mathbf{r} -dependent deformed polaritons.

Chapter 5

Concluding Remarks

This thesis sets first steps towards explaining the vastly growing field of molecular polaritons and into systematic study of nonlinearities through multidimensional spectroscopy. Quasi-particle method developed here allows for computationally feasible structural analysis of larger macromolecules confined in optical cavities under coherent limits.

The basic physics of molecular excitons, optical cavity is explained in Chapter 1. We then quickly delve into deriving self consistent set of nonlinear equations for polariton dynamical variable and solve them using Bethe-Salpeter equations. We then use the solutions to derive a closed form expression of polariton-polariton scattering which is finally used to derive coherent multidimensional signals. Such a representation of signal requires us to calculate poles of tetradic polariton scattering matrices, the poles of which are resonant with the doubly excited polaritons (bipolaritons) requiring only the information regarding the singly excited polariton manifold. This method is particularly useful for computing higher order signals for larger macromolecules where sum over states (SOS) method would require to diagonalize $(N + 1)(N + 2)$ size matrices for N chromophores in single mode optical cavity increasing the computation time. In the formulation done in Chapter 2 though the poles of

tetradic matrix is needed to calculate which is as large $(N + 1)^2 \times (N + 1)^2$, these matrices are usually sparse and numerical diagonalizations are more tractable. Furthermore, they give more intuitive physical understanding of polariton interactions.

In chapter 3, the changes of vibrational anharmonicities are discussed for molecular vibrational polaritons using sum over states for single and two molecules in single mode optical cavity. Chapter 4 delves deeper into the polariton-polariton interactions and provides a measure for signal enhancements for DQC in terms of deformation parameter. These parameters q are intrinsically related to the number operators hence expanding over proper number basis gives the explicit N dependence on third order signal which is not necessarily N^2 but a more complicated function of deformation parameter q and total number of molecular polaritons N . It further delves into the possibilities of observing "dark" states due to polariton-polariton interactions which explicitly depends on number of polaritons only for deformed molecular polaritons. Possibilities of expanding the theory of coherent quasiparticle representations of molecular polaritons to incoherent cases is mentioned very briefly and could be an interesting future project.

Bibliography

- [1] Vladimir I Novoderezhkin, Miguel A Palacios, Herbert Van Amerongen, and Rienk Van Grondelle. Energy-transfer dynamics in the lhci complex of higher plants: modified redfield approach. *The Journal of Physical Chemistry B*, 108(29):10363–10375, 2004.
- [2] Edward A Stern. Theory of the anharmonic properties of solids. *Physical Review*, 111(3):786, 1958.
- [3] Yoshihisa Yamamoto and Kouichi Semba. *Principles and Methods of Quantum Information Technologies*. Springer, 2016.
- [4] Co E Treanor, JW Rich, and RG Rehm. Vibrational relaxation of anharmonic oscillators with exchange-dominated collisions. *The Journal of Chemical Physics*, 48(4):1798–1807, 1968.
- [5] Guglielmo Lanzani, Giulio Cerullo, and Sandro De Silvestri. *Coherent Vibrational Dynamics*. CRC Press, 2007.
- [6] Shaul Mukamel. *Principles of nonlinear optical spectroscopy*. Number 6. Oxford University Press on Demand, 1999.
- [7] LD Landau. The theory of a fermi liquid. *Soviet Physics JETP-USSR*, 3(6):920–925, 1957.
- [8] Shaul Mukamel and Darius Abramavicius. Many-body approaches for simulating coherent nonlinear spectroscopies of electronic and vibrational excitons. *Chemical reviews*, 104(4):2073–2098, 2004.
- [9] Prasoon Saurabh and Shaul Mukamel. Two-dimensional infrared spectroscopy of vibrational polaritons of molecules in an optical cavity. *The Journal of chemical physics*, 144(12):124115, 2016.
- [10] S. Mukamel. *Principles of nonlinear optical spectroscopy*, volume 29. Oxford University Press, New York, 1995.
- [11] M. O. Scully. *Quantum optics*. university press, Cambridge, 1997.
- [12] C. Cohen-Tannoudji, J. Dupont-Roc, and G. Grynberg. *Photons and Atoms—Introduction to Quantum Electrodynamics (Wiley Professional)*. 1997.

- [13] Y. Aharonov and D. Bohm. Significance of electromagnetic potentials in the quantum theory. *Physical Review*, 115, 1959.
- [14] J. Rammer. *Quantum transport theory*. Westview Press, 2004.
- [15] R. P. Feynman, R. B. Leighton, and M. Sands. The Feynman Lectures on Physics, Desktop Edition Volume I. *vol.*, 1, 2013.
- [16] P. Bharadwaj, B. Deutsch, and L. Novotny. Optical antennas. *Advances in Optics and Photonics*, 1:438–483, 2009.
- [17] M. I. Stockman. Nanoplasmonics: past, present, and glimpse into future. *Optics express*, 19:22029–22106, 2011.
- [18] M. I. Stockman. Quantum Nanoplasmonics,. *p*, pages 85–132.
- [19] J. E. Donehue, E. Wertz, C. N. Talicska, and J. S. Biteen. Plasmon-enhanced brightness and photostability from single fluorescent proteins coupled to gold nanorods. *The Journal of Physical Chemistry C*, 118:15027–15035, 2014.
- [20] D. A. Kalashnikov, Z. Pan, A. I. Kuznetsov, and L. A. Krivitsky. Quantum spectroscopy of plasmonic nanostructures. *Physical Review X*, 4, 2014.
- [21] L. Novotny and B. Hecht. *Principles of nano-optics*. university press, Cambridge, 2012.
- [22] Feizhi Ding, Emilie B. Guidez, Christine M. Aikens, and Xiaosong Li. Quantum coherent plasmon in silver nanowires: A real-time TDDFT study. *The Journal of chemical physics*, 140, 2014.
- [23] R. M. Stöckle, Y. D. Suh, V. Deckert, and R. Zenobi. Nanoscale chemical analysis by tip-enhanced Raman spectroscopy. *Chemical Physics Letters*, 318:131–136, 2000.
- [24] E. Bailo and V. Deckert. Tip-enhanced Raman scattering. *Chemical Society Reviews*, 37:921–930, 2008.
- [25] M. L. Brongersma and P. G. Kik. *Surface plasmon nanophotonics*. Springer, 2007.
- [26] S. Kühn, U. Håkanson, L. Rogobete, and V. Sandoghdar. Enhancement of single-molecule fluorescence using a gold nanoparticle as an optical nanoantenna. *Physical review letters*, 97, 2006.
- [27] L. V. Brown, X. Yang, K. Zhao, B. Zheng, P. Nordlander, and N. J. Halas. *Fan-Shaped Gold Nanoantennas above Reflective Substrates for Surface-Enhanced Infrared Absorption (SEIRA)*. *Nano letters*, 2015.
- [28] Claude Fabre, Vahid Sandoghdar, Nicolas Treps, and Leticia F Cugliandolo. *Quantum Optics and Nanophotonics*, volume 101. Oxford University Press, 2017.

- [29] A. Minovich, A. E. Klein, N. Janunts, T. Pertsch, D. N. Neshev, and Y. S. Kivshar. Generation and near-field imaging of Airy surface plasmons. *Physical review letters*, 107, 2011.
- [30] M. Aeschlimann, M. Bauer, D. Bayer, T. Brixner, F. J. G. de Abajo, W. Pfeiffer, M. Rohmer, C. Spindler, and F. Steeb. Adaptive subwavelength control of nano-optical fields. *Nature*, 446:301–304, 2007.
- [31] N. S. Abadeer, M. R. Brennan, W. L. Wilson, and C. J. Murphy. Distance and Plasmon Wavelength Dependent Fluorescence of Molecules Bound to Silica-Coated Gold Nanorods. *ACS nano*, 8:8392–8406, 2014.
- [32] R. Zhang, Y. Zhang, Z. C. Dong, S. Jiang, C. Zhang, L. G. Chen, L. Zhang, Y. Liao, J. Aizpurua, Y. Luo, J. L. Yang, and J. G. Hou. Chemical mapping of a single molecule by plasmon-enhanced Raman scattering. *Nature*, 498:82–86, 2013.
- [33] V. Myroshnychenko, J. Rodríguez-Fernández, I. Pastoriza-Santos, A. M. Funston, C. Novo, P. Mulvaney, L. M. Liz-Marzán, and F. J. G. de Abajo. Modelling the optical response of gold nanoparticles. *Chemical Society Reviews*, 37:1792–1805, 2008.
- [34] András Vukics, Tobias Grießer, and Peter Domokos. Elimination of the a-square problem from cavity qed. *Physical review letters*, 112(7):073601, 2014.
- [35] Ziad Ganim, Hoi Sung Chung, Adam W Smith, Lauren P DeFlores, Kevin C Jones, and Andrei Tokmakoff. Amide i two-dimensional infrared spectroscopy of proteins. *Accounts of chemical research*, 41(3):432–441, 2008.
- [36] Peter Hamm and Martin Zanni. *Concepts and methods of 2D infrared spectroscopy*. Cambridge University Press, 2011.
- [37] Oleksiy Roslyak, Benjamin P Fingerhut, Kochise Bennett, and Shaul Mukamel. Quasi-particle representation of coherent nonlinear optical signals of multi-excitons. *New Journal of Physics*, 15(8):083049, 2013.
- [38] Shaul Mukamel, Rafal Oszwaldowski, and Darius Abramavicius. Sum-over-states versus quasiparticle pictures of coherent correlation spectroscopy of excitons in semiconductors: Femtosecond analogs of multidimensional nmr. *Physical Review B*, 75(24):245305, 2007.
- [39] Vladimir Chernyak, Wei Min Zhang, and Shaul Mukamel. Multidimensional femtosecond spectroscopies of molecular aggregates and semiconductor nanostructures: The nonlinear exciton equations. *The Journal of chemical physics*, 109(21):9587–9601, 1998.
- [40] Wei Min Zhang, Vladimir Chernyak, and Shaul Mukamel. Multidimensional femtosecond correlation spectroscopies of electronic and vibrational excitons. *The Journal of chemical physics*, 110(11):5011–5028, 1999.
- [41] XI Ultrafast Phenomena. T. Elsaesser, J. Fujimoto, D. A. Wiersma, and W. Zinth, 1998.

- [42] Wim P de Boeij, Maxim S Pshenichnikov, and Douwe A Wiersma. On the relation between the echo-peak shift and brownian-oscillator correlation function. *Chemical physics letters*, 253(1-2):53–60, 1996.
- [43] GM D’Ázariano, U Leonhardt, and H Paul. Homodyne detection of the density matrix of the radiation field. *Physical Review A*, 52(3):R1801, 1995.
- [44] Wesley R Burghardt, Marcin Sikorski, Alec R Sandy, and Suresh Narayanan. X-ray photon correlation spectroscopy during homogenous shear flow. *Physical Review E*, 85(2):021402, 2012.
- [45] Shaul Mukamel and Saar Rahav. Ultrafast nonlinear optical signals viewed from the molecule’s perspective: Kramers–heisenberg transition-amplitudes versus susceptibilities. *Advances in atomic, molecular, and optical physics*, 59:223–263, 2010.
- [46] Edwin E Salpeter and Hans Albrecht Bethe. A relativistic equation for bound-state problems. *Physical Review*, 84(6):1232, 1951.
- [47] S Haroche. Fundamental systems in quantum optics. *Les Houches Summer School Session*, 53, 1992.
- [48] MS Skolnick, TA Fisher, and DM Whittaker. Strong coupling phenomena in quantum microcavity structures. *Semiconductor Science and Technology*, 13(7):645, 1998.
- [49] Vincenzo Savona, LC Andreani, P Schwendimann, and A Quattropani. Quantum well excitons in semiconductor microcavities: unified treatment of weak and strong coupling regimes. *Solid State Communications*, 93(9):733–739, 1995.
- [50] Paul R Berman. *Cavity quantum electrodynamics*. Academic Press, Inc., Boston, MA (United States), 1994.
- [51] Johannes Feist and Francisco J Garcia-Vidal. Extraordinary exciton conductance induced by strong coupling. *Physical Review Letters*, 114(19):196402, 2015.
- [52] Atef Shalabney, Jino George, J Hutchison, Guido Pupillo, Cyriaque Genet, and Thomas W Ebbesen. Coherent coupling of molecular resonators with a microcavity mode. *Nature communications*, 6, 2015.
- [53] Javier del Pino, Johannes Feist, and Francisco J Garcia-Vidal. Quantum theory of collective strong coupling of molecular vibrations with a microcavity mode. *New Journal of Physics*, 17(5):053040, 2015.
- [54] Atef Shalabney, Jino George, Hidefumi Hiura, James A Hutchison, Cyriaque Genet, Petra Hellwig, and Thomas W Ebbesen. Enhanced Raman Scattering from Vibro-Polariton Hybrid States. *Angewandte Chemie International Edition*, 54(27):7971–7975, 2015.

- [55] BS Simpkins, Kenan P Fears, Walter J Dressick, Bryan T Spann, Adam D Dunkelberger, and Jeffrey C Owrutsky. Spanning strong to weak normal mode coupling between vibrational and fabry–pérot cavity modes through tuning of vibrational absorption strength. *ACS Photonics*, 2(10):1460–1467, 2015.
- [56] Serge Haroche and Jean Michel Raimond. *Exploring the quantum*. Oxford Univ. Press, 2006.
- [57] Sanli Faez, Pierre Türschmann, Harald R Haakh, Stephan Götzinger, and Vahid Sandoghdar. Coherent interaction of light and single molecules in a dielectric nanoguide. *Physical review letters*, 113(21):213601, 2014.
- [58] Zhaorong Wang, Rahul Gogna, and Hui Deng. What is the best planar cavity for maximizing coherent exciton-photon coupling. *Applied Physics Letters*, 111(6):061102, 2017.
- [59] Zhenfeng Liu, Hanchi Yan, Kebin Wang, Tingyun Kuang, et al. Crystal structure of spinach major light-harvesting complex at 2.72 angstrom resolution. *Nature*, 428(6980):287, 2004.
- [60] Vladimir I Novoderezhkin, Miguel A Palacios, Herbert Van Amerongen, and Rienk Van Grondelle. Excitation dynamics in the lhci complex of higher plants: modeling based on the 2.72 Å crystal structure. *The Journal of Physical Chemistry B*, 109(20):10493–10504, 2005.
- [61] Vladimir Novoderezhkin, Alessandro Marin, and Rienk van Grondelle. Intra-and inter-monomeric transfers in the light harvesting lhci complex: the redfield–förster picture. *Physical Chemistry Chemical Physics*, 13(38):17093–17103, 2011.
- [62] Pavel Malý, J Michael Gruber, Rienk Van Grondelle, and Tomáš Mančal. Single molecule spectroscopy of monomeric lhci: experiment and theory. *Scientific reports*, 6:26230, 2016.
- [63] William P Bricker, Prathamesh M Shenai, Avishek Ghosh, Zhengtang Liu, Miriam Grace M Enriquez, Petar H Lambrev, Howe-Siang Tan, Cynthia S Lo, Sergei Tretiak, Sebastian Fernandez-Alberti, et al. Non-radiative relaxation of photoexcited chlorophylls: theoretical and experimental study. *Scientific reports*, 5, 2015.
- [64] Gabriela S Schlau-Cohen, Akihito Ishizaki, Tessa R Calhoun, Naomi S Ginsberg, Matteo Ballottari, Roberto Bassi, and Graham R Fleming. Elucidation of the timescales and origins of quantum electronic coherence in lhci. *Nature chemistry*, 4(5):389–395, 2012.
- [65] Darius Abramavicius, Benoit Palmieri, Dmitri V Voronine, Frantisek Sanda, and Shaul Mukamel. Coherent multidimensional optical spectroscopy of excitons in molecular aggregates; quasiparticle versus supermolecule perspectives. *Chemical reviews*, 109(6):2350–2408, 2009.

- [66] Jörg Megow, Beate Röder, Alexander Kulesza, Vlasta Bonačić-Koutecký, and Volkhard May. A mixed quantum–classical description of excitation energy transfer in supramolecular complexes: Förster theory and beyond. *ChemPhysChem*, 12(3):645–656, 2011.
- [67] VM Agranovich, M Litinskaia, and David G Lidzey. Cavity polaritons in microcavities containing disordered organic semiconductors. *Physical Review B*, 67(8):085311, 2003.
- [68] Galina Khitrova, HM Gibbs, F Jahnke, M Kira, and Stephan W Koch. Nonlinear optics of normal-mode-coupling semiconductor microcavities. *Reviews of Modern Physics*, 71(5):1591, 1999.
- [69] Daniele Sanvitto and Vladislav Timofeev. *Exciton Polaritons in Microcavities: New Frontiers*, volume 172. Springer Science & Business Media, 2012.
- [70] Eric R Bittner and Carlos Silva. Estimating the conditions for polariton condensation in organic thin-film microcavities. *The Journal of chemical physics*, 136(3):034510, 2012.
- [71] Steven T Cundiff, Travis Autry, Gaël Nardin, Daniele Bajoni, Aristide Lemaître, Sophie Bouchoule, and Jacqueline Bloch. Observation of the excitation ladder in a microcavity diode using multi-quantum coherent optical photocurrent spectroscopy. In *Nonlinear Optics*, pages NW3A–1. Optical Society of America, 2015.
- [72] Justyna A Ćwik, Peter Kirton, Simone De Liberato, and Jonathan Keeling. Excitonic spectral features in strongly coupled organic polaritons. *Physical Review A*, 93(3):033840, 2016.
- [73] KS Daskalakis, SA Maier, Ray Murray, Stéphane Kéna-Cohen, et al. Nonlinear interactions in an organic polariton condensate. *Nat. Mater*, 13(3):271–278, 2014.
- [74] David M Coles, Niccolo Somaschi, Paolo Michetti, Caspar Clark, Pavlos G Lagoudakis, Pavlos G Savvidis, and David G Lidzey. Polariton-mediated energy transfer between organic dyes in a strongly coupled optical microcavity. *Nature materials*, 13(7):712–719, 2014.
- [75] Justyna A Ćwik, Sahinur Reja, Peter B Littlewood, and Jonathan Keeling. Polariton condensation with saturable molecules dressed by vibrational modes. *EPL (Europhysics Letters)*, 105(4):47009, 2014.
- [76] Javier del Pino, Johannes Feist, and Francisco J Garcia-Vidal. Signatures of vibrational strong coupling in raman scattering. *The Journal of Physical Chemistry C*, 119(52):29132–29137, 2015.
- [77] Markus Kowalewski, Kochise Bennett, and Shaul Mukamel. Non-adiabatic dynamics of molecules in optical cavities. *The Journal of chemical physics*, 144(5):054309, 2016.

- [78] Markus Kowalewski, Kochise Bennett, and Shaul Mukamel. Cavity femtochemistry; manipulating nonadiabatic dynamics at avoided crossings. *The journal of physical chemistry letters*, 2016.
- [79] FC Spano. Optical microcavities enhance the exciton coherence length and eliminate vibronic coupling in j-aggregates. *The Journal of chemical physics*, 142(18):184707, 2015.
- [80] Semion K Saikin, Alexander Eisfeld, Stéphanie Valleau, and Alán Aspuru-Guzik. Photonics meets excitonics: natural and artificial molecular aggregates. *Nanophotonics*, 2(1):21–38, 2013.
- [81] David M Coles, Yanshen Yang, Yaya Wang, Richard T Grant, Robert A Taylor, Semion K Saikin, Alán Aspuru-Guzik, David G Lidzey, Joseph Kuo-Hsiang Tang, and Jason M Smith. Strong coupling between chlorosomes of photosynthetic bacteria and a confined optical cavity mode. *Nature communications*, 5, 2014.
- [82] James A Hutchison, Tal Schwartz, Cyriaque Genet, Eloïse Devaux, and Thomas W Ebbesen. Modifying chemical landscapes by coupling to vacuum fields. *Angewandte Chemie International Edition*, 51(7):1592–1596, 2012.
- [83] Xiaolan Zhong, Thibault Chervy, Shaojun Wang, Jino George, Anoop Thomas, James Hutchison, Eloïse Devaux, Cyriaque Genet, and Thomas Ebbesen. Non-radiative energy transfer via hybrid light-matter states. In *CLEO: Science and Innovations*, pages STh4Q–5. Optical Society of America, 2016.
- [84] Oleksiy Roslyak, Godfrey Gumbs, and Shaul Mukamel. Signatures of carrier multiplication in the frequency resolved fluorescence spectra from polaritons. *Journal of Modern Optics*, 57(19):2009–2019, 2010.
- [85] Kevin Hennessy, Antonio Badolato, M Winger, D Gerace, Mete Atatüre, S Gulde, S Fält, Evelyn L Hu, and A Imamoğlu. Quantum nature of a strongly coupled single quantum dot–cavity system. *Nature*, 445(7130):896–899, 2007.
- [86] AI Tartakovskii, DN Krizhanovskii, and VD Kulakovskii. Polariton-polariton scattering in semiconductor microcavities: Distinctive features and similarities to the three-dimensional case. *Physical Review B*, 62(20):R13298, 2000.
- [87] Brian L Wilmer, Felix Passmann, Michael Gehl, Galina Khitrova, and Alan D Bristow. Multidimensional coherent spectroscopy of a semiconductor microcavity. *Physical Review B*, 91(20):201304, 2015.
- [88] Gaël Nardin. Multidimensional coherent optical spectroscopy of semiconductor nanostructures: a review. *Semiconductor Science and Technology*, 31(2):023001, 2015.
- [89] N Takemura, Stephane Trebaol, MD Anderson, V Kohnle, Yoan Léger, DY Oberli, Marcia T Portella-Oberli, and B Deveaud. Two-dimensional Fourier transform spectroscopy of exciton-polaritons and their interactions. *Physical Review B*, 92(12):125415, 2015.

- [90] Felipe Herrera, Borja Peropadre, Leonardo A Pachon, Semion K Saikin, and Alán Aspuru-Guzik. Quantum nonlinear optics with polar J-aggregates in microcavities. *The Journal of Physical Chemistry Letters*, 5(21):3708–3715, 2014.
- [91] Camilla Pellegrini, Johannes Flick, Ilya V Tokatly, Heiko Appel, and Angel Rubio. Optimized effective potential for quantum electrodynamical time-dependent density functional theory. *Physical review letters*, 115(9):093001, 2015.
- [92] Michael Ruggenthaler, Johannes Flick, Camilla Pellegrini, Heiko Appel, Ilya V Tokatly, and Angel Rubio. Quantum-electrodynamical density-functional theory: Bridging quantum optics and electronic-structure theory. *Physical Review A*, 90(1):012508, 2014.
- [93] Johannes Flick, Michael Ruggenthaler, Heiko Appel, and Angel Rubio. Atoms and molecules in cavities: From weak to strong coupling in qed chemistry. *arXiv preprint arXiv:1609.03901*, 2016.
- [94] Jan A Leegwater and Shaul Mukamel. Exciton-scattering mechanism for enhanced nonlinear response of molecular nanostructures. *Physical Review A*, 46(1):452, 1992.
- [95] Francis C Spano and Shaul Mukamel. Cooperative nonlinear optical response of molecular aggregates: Crossover to bulk behavior. *Physical review letters*, 66(9):1197, 1991.
- [96] O Kühn, V Chernyak, and S Mukamel. Two-exciton spectroscopy of photosynthetic antenna complexes: Collective oscillator analysis. *The Journal of chemical physics*, 105(19):8586–8601, 1996.
- [97] Darius Abramavicius and Shaul Mukamel. Energy-transfer and charge-separation pathways in the reaction center of photosystem ii revealed by coherent two-dimensional optical spectroscopy. *The Journal of chemical physics*, 133(18):184501, 2010.
- [98] JJ Hopfield. Theory of the contribution of excitons to the complex dielectric constant of crystals. *Physical Review*, 112(5):1555, 1958.
- [99] Monique Combescot and Shiue-Yuan Shiau. *Excitons and Cooper pairs: two composite bosons in many-body physics*. Oxford University Press, 2015.
- [100] Travis Autry, Gael Nardin, Daniele Bajoni, Aristide Lemaître, Sophie Bouchoule, Jacqueline Bloch, and Steven Cundiff. Measurement of Nonlinear Polariton Dispersion Curves Reveals the Tavis-Cummings Quantum Ladder. In *CLEO: QELS_ Fundamental Science*, pages FW4B–7. Optical Society of America, 2015.
- [101] Yongbao Sun, Yoseb Yoon, Mark Steger, Gangqiang Liu, Loren N Pfeiffer, Ken West, David W Snoke, and Keith A Nelson. Polaritons are Not Weakly Interacting: Direct Measurement of the Polariton-Polariton Interaction Strength. *arXiv preprint arXiv:1508.06698*, 2015.
- [102] Andrea Alù, Mário G Silveirinha, Alessandro Salandrino, and Nader Engheta. Epsilon-near-zero metamaterials and electromagnetic sources: Tailoring the radiation phase pattern. *Physical Review B*, 75(15):155410, 2007.

- [103] Romain Fleury and Andrea Alù. Enhanced superradiance in epsilon-near-zero plasmonic channels. *Physical Review B*, 87(20):201101, 2013.
- [104] Hrishikesh Kelkar, Daqing Wang, Björn Hoffmann, Silke Christiansen, Stephan Götzinger, and Vahid Sandoghdar. A sub- λ 3 mode volume cantilever-based Fabry-Pérot microcavity. In *European Quantum Electronics Conference*, page EG_6_1. Optical Society of America, 2015.
- [105] Alexander Benz, Salvatore Campione, John F Klem, Michael B Sinclair, and Igal Brener. Control of Strong Light–Matter Coupling Using the Capacitance of Metamaterial Nanocavities. *Nano letters*, 15(3):1959–1966, 2015.
- [106] Zaizhi Lai, Nicholas K Preketes, Shaul Mukamel, and Jin Wang. Monitoring the folding of Trp-cage peptide by two-dimensional infrared (2DIR) spectroscopy. *The Journal of Physical Chemistry B*, 117(16):4661–4669, 2013.
- [107] Darius Abramavicius, Dmitri V Voronine, and Shaul Mukamel. Double-quantum resonances and exciton-scattering in coherent 2D spectroscopy of photosynthetic complexes. *Proceedings of the National Academy of Sciences*, 105(25):8525–8530, 2008.
- [108] Ravindra Venkatramani and Shaul Mukamel. Correlated line broadening in multidimensional vibrational spectroscopy. *The Journal of chemical physics*, 117(24):11089–11101, 2002.
- [109] Andrei Piryatinski, Vladimir Chernyak, and Shaul . Two-dimensional correlation spectroscopies of localized vibrations. *Chemical Physics*, 266(2):311–322, 2001.
- [110] Christian Greve, Nicholas K Preketes, Henk Fidder, Rene Costard, Benjamin Koeppel, Ismael A Heisler, Shaul Mukamel, Friedrich Temps, Erik TJ Nibbering, and Thomas Elsaesser. N–H stretching excitations in adenosine-thymidine base pairs in solution: pair geometries, infrared line shapes, and ultrafast vibrational dynamics. *The Journal of Physical Chemistry A*, 117(3):594–606, 2013.
- [111] Justyna A Cwik, Peter Kirton, Simone De Liberato, and Jonathan Keeling. Self-consistent molecular adaptation induced by strong coupling. *arXiv preprint arXiv:1506.08974*, 2015.
- [112] Hisaki Oka and Hajime Ishihara. Real-time analysis of the optical response of cavity bipolaritons: Four-wave mixing and dynamics of formation. *Physical Review B*, 78(19):195314, 2008.
- [113] Hisaki Oka and Hajime Ishihara. Highly efficient generation of entangled photons by controlling cavity bipolariton states. *Physical review letters*, 100(17):170505, 2008.
- [114] Oleksiy Roslyak, Godfrey Gumbs, and Shaul Mukamel. Two-Photon-Coincidence Fluorescence Spectra of Cavity Multipolaritons: Novel Signatures of Multiexciton Generation. *Nano letters*, 10(10):4253–4259, 2010.

- [115] Tomoyuki Hayashi and Shaul Mukamel. Two-dimensional vibrational lineshapes of amide III, II, I and A bands in a helical peptide. *Journal of molecular liquids*, 141(3):149–154, 2008.
- [116] Igor V Rubtsov, Jianping Wang, and Robin M Hochstrasser. Vibrational coupling between amide-I and amide-A modes revealed by femtosecond two color infrared spectroscopy. *The Journal of Physical Chemistry A*, 107(18):3384–3396, 2003.
- [117] Hui Deng, Hartmut Haug, and Yoshihisa Yamamoto. Exciton-polariton bose-einstein condensation. *Reviews of modern physics*, 82(2):1489, 2010.
- [118] Jacek Kasprzak, M Richard, S Kundermann, A Baas, P Jeambrun, JMJ Keeling, FM Marchetti, MH Szymańska, R Andre, JL Staehli, et al. Bose–Einstein condensation of exciton polaritons. *Nature*, 443(7110):409–414, 2006.
- [119] Johannes D Plumhof, Thilo Stöferle, Lijian Mai, Ullrich Scherf, and Rainer F Mahrt. Room-temperature Bose–Einstein condensation of cavity exciton–polaritons in a polymer. *Nature materials*, 13(3):247–252, 2014.
- [120] Markus Kowalewski, Giovanna Morigi, Pepijn WH Pinkse, and Regina de Vivie-Riedle. Cavity sideband cooling of trapped molecules. *Physical Review A*, 84(3):033408, 2011.
- [121] Johannes Feist, Javier Galego, and Francisco J Garcia-Vidal. Polaritonic chemistry with organic molecules. *ACS Photonics*, 2017.
- [122] Javier Galego, Francisco J Garcia-Vidal, and Johannes Feist. Cavity-induced modifications of molecular structure in the strong coupling regime. *arXiv preprint arXiv:1506.03331*, 2015.
- [123] Georg Rossbach, Jacques Levrat, Eric Feltn, Jean-François Carlin, Raphaël Butté, and Nicolas Grandjean. Impact of saturation on the polariton renormalization in iii-nitride based planar microcavities. *Physical Review B*, 88(16):165312, 2013.
- [124] Yongbao Sun, Yoseob Yoon, Mark Steger, Gangqiang Liu, Loren N Pfeiffer, Ken West, David W Snoke, and Keith A Nelson. Direct measurement of polariton-polariton interaction strength. *Nature Physics*, 2017.
- [125] P Cilibrizzi, H Ohadi, T Ostatnicky, A Askitopoulos, W Langbein, and P Lagoudakis. Linear wave dynamics explains observations attributed to dark solitons in a polariton quantum fluid. *Physical review letters*, 113(10):103901, 2014.
- [126] P Saurabh and S Mukamel. Quasiparticle representation of coherent nonlinear optical signals. *Quasiparticle representation of coherent nonlinear optical signals*, Submitted.
- [127] JC López Carreño, C Sánchez Muñoz, D Sanvitto, E del Valle, and FP Laussy. Exciting polaritons with quantum light. *Physical review letters*, 115(19):196402, 2015.
- [128] Zbigniew Ficek and Ryszard Tanaś. *Quantum-Limit Spectroscopy*. Springer, 2017.

- [129] R Houdré, JL Gibernon, P Pellandini, RP Stanley, U Oesterle, C Weisbuch, J OǎǎZ-Gorman, B Roycroft, and M Ilegems. Saturation of the strong-coupling regime in a semiconductor microcavity: Free-carrier bleaching of cavity polaritons. *Physical Review B*, 52(11):7810, 1995.
- [130] S Schmitt-Rink, DS Chemla, and DAB Miller. Theory of transient excitonic optical nonlinearities in semiconductor quantum-well structures. *Physical Review B*, 32(10):6601, 1985.
- [131] DS Chemla, J-Y Bigot, M-A Mycek, S Weiss, and W Schäfer. Ultrafast phase dynamics of coherent emission from excitons in gas quantum wells. *Physical Review B*, 50(12):8439, 1994.
- [132] Guang-Ri Jin and Wu-Ming Liu. Collapses and revivals of exciton emission in a semiconductor microcavity: Detuning and phase-space filling effects. *Physical Review A*, 70(1):013803, 2004.
- [133] A Imamoglu. Phase-space filling and stimulated scattering of composite bosons. *Physical Review B*, 57(8):R4195, 1998.
- [134] Yaroslav V Kartashov, Vladimir V Konotop, and Lluís Torner. Compactons and bistability in exciton-polariton condensates. *Physical Review B*, 86(20):205313, 2012.
- [135] Jacob Katriel and Maurice Kibler. Normal ordering for deformed boson operators and operator-valued deformed stirling numbers. *Journal of Physics A: Mathematical and General*, 25(9):2683, 1992.
- [136] LC Biedenharn. The quantum group $su_q(2)$ and a q -analogue of the boson operators. *Journal of Physics A: Mathematical and General*, 22(18):L873, 1989.
- [137] Felipe Herrera and Frank C Spano. Theory of nanoscale organic cavities: The essential role of vibration-photon dressed states. *arXiv preprint arXiv:1707.02992*, 2017.
- [138] Felipe Herrera and Frank C Spano. Dark vibronic polaritons and the spectroscopy of organic microcavities. *Physical Review Letters*, 118(22):223601, 2017.
- [139] Ahsan Zeb, Peter Kirton, and Jonathan Keeling. Exact states and spectra of vibrationally dressed polaritons. *ACS Photonics*, 2017.
- [140] Michel Gross and Serge Haroche. Superradiance: An essay on the theory of collective spontaneous emission. *Physics reports*, 93(5):301–396, 1982.
- [141] Robert H Dicke. Coherence in spontaneous radiation processes. *Physical Review*, 93(1):99, 1954.
- [142] Naotomo Takemura. On the physics of polariton interactions. 2016.
- [143] C Leroux, LCG Govia, and AA Clerk. Enhancing cavity qed via anti-squeezing: synthetic ultra-strong coupling. *arXiv preprint arXiv:1709.09091*, 2017.

- [144] Vladimir Y Chernyak, Prasoon Saurabh, and Shaul Mukamel. Non-linear non-local molecular electrodynamics with nano-optical fields. *The Journal of chemical physics*, 143(16):164107, 2015.
- [145] Pierre Nataf and Cristiano Ciuti. No-go theorem for superradiant quantum phase transitions in cavity QED and counter-example in circuit QED. *Nature communications*, 1:72, 2010.
- [146] Rubin J.L. Meyer J Tuszynski, J.A. and Kibler. M. Statistical mechanics of a q-deformed boson gas. *Physics Letters A*, 175(175):173–177, 1993.
- [147] Zhedong Zhang, Kochise Bennett, Vladimir Chernyak, and Shaul Mukamel. Utilizing microcavities to suppress third-order cascades in fifth-order raman spectra. *The Journal of Physical Chemistry Letters*, 8(14):3387–3391, 2017.

Appendix A

Supplementary for Chapter 3

A.1 Multimode Molecular Vibration Hamiltonian

We start with the Frenkel exciton Hamiltonian coupled to an infrared cavity [39, 65, 114, 52, 53, 54, 55],

$$\begin{aligned} H_0 &= \omega_c(\theta)a^\dagger a + \sum_i^m \omega_i b_i^\dagger b_i + \sum_{i \neq j}^m J_{ij} b_i^\dagger b_j \\ &- \sum_{ij}^m \frac{\Delta_{ij}}{2} b_i^\dagger b_j^\dagger b_i b_j + \sum_{i,j=1}^m \tilde{g}_i (a^\dagger b_i + b_i^\dagger a). \end{aligned} \quad (\text{A.1})$$

$\omega_c(\theta) = \omega_0 \left(1 - \frac{\sin^2(\theta)}{n_{eff}^2}\right)^{-1/2}$, is the angle-dependent cavity energy with $\omega_0 =$ being cavity cut-off energy (or maximum) and, θ the angle of incidence to the cavity mirrors. The number of oscillators is denoted by m . We set $m = 1$ for Amide-I vibrations, and $m = 2$ for Amide-I+II vibrations of a NMA molecule respectively (Fig. 3.1). n_{eff} is the effective intracavity refractive index. When the refractive indices of one of the two layers' of a Distributed

Bragg Reflector (DBR) Fabry-Perot is equal to the empty cavity refractive index n_c , say $n_c = (n_2 n_1)$, then $n_{eff} = \sqrt{n_1 n_2}$ [49]. ω_i is the exciton energy of i^{th} oscillator, J_{ij} is the scalar harmonic coupling between oscillators and Δ_{ij} is the anharmonicity due to vibrational exciton-exciton interaction [39, 65, 114].

Assuming a single mode cavity, we introduce the polariton creation (\hat{p}^\dagger) and annihilation (\hat{p}) operators,

$$\hat{p}_i = Ca + X_i b_i \quad \hat{p}_i^\dagger = C^* a^\dagger + X_i^* b_i^\dagger. \quad (\text{A.2})$$

The Hopfield coefficients, C and X_i , are normalized as $|C|^2 + \sum_{i=1}^n |X_i|^2 = 1$ [98] and the polariton operators follow bosonic commutation relations. The coefficients vectors $(C, X_1, \dots, X_n)^T$ are easily found as the eigenvectors of the effective Hopfield-Bogoliubov matrix [145],

$$\begin{pmatrix} \omega_c(\theta) & 2\tilde{g}_1 & \dots & \dots & 2\tilde{g}_m \\ 2\tilde{g}_1 & \omega_1 & 0 & \dots & 0 \\ \vdots & \vdots & \vdots & \dots & \vdots \\ 2\tilde{g}_m & 0 & 0 & \dots & \omega_m \end{pmatrix}. \quad (\text{A.3})$$

This allows us to rewrite Eq. (A.1) as weakly interacting polaritons,

$$H_{pol} = \sum_{kk}^{\mathcal{N}} \Omega_{kk} \hat{p}_k^\dagger \hat{p}_k - \sum_{kl}^{\mathcal{N}} \tilde{V}_{kl} \hat{p}_k^\dagger \hat{p}_l^\dagger \hat{p}_k \hat{p}_l. \quad (\text{A.4})$$

Here, Ω_{kk} are the eigenvalues of the $\mathcal{N} \times \mathcal{N}$ matrix in Eqn. A.3, where $\mathcal{N} = m + 1$. \tilde{V}_{kl} is the effective polariton anharmonicity. For non-zero order of coefficient C , \tilde{V}_{kl} vanishes, and simply reduces to $\tilde{V}_{kl} = \frac{\Delta_{kl}}{2} |X_k|^2 |X_l|^2$. The interaction with the probe field $\mathbf{E}(\mathbf{r}, t) = \sum_{i=1}^3 \mathcal{E}(t - t_i) e^{i\mathbf{k}_i \mathbf{r}_i - i\omega_i(t-t_i)} + c.c$ is given by,

$$H_{int} = - \sum_m \mu_m \mathbf{E}^*(\mathbf{r}, t) \hat{p}_m + H.c. \quad (\text{A.5})$$

where, μ_m first order polariton dipole moment. The total Hamiltonian is then simply, $H_{tot} = H_{pol} + H_{int}$.

A.1.1 The molecular vibrational single-polariton (MVP) and double-polariton (MVBP) manifolds:

The third order 2D cavity-mediated signal, depends only on the 1-polariton(MVP) and 2-polariton(MVBP) states. We next denote the state when polariton m is in the excited excited state by, $|m\rangle = \hat{p}_m^\dagger |0\rangle$ where, $|0\rangle$ is the ground state in polaritonic basis. MVP eigenstates $|e\rangle$ are related to $|m\rangle$ by following unitary transformation, $|e\rangle = \sum_m \phi_{me} |m\rangle$ with, energies $\epsilon_e (= \sum_{mn} \phi_{en} \Omega_{nm} \phi_{me})$ implicitly depending on incidence angle (θ) and the cavity coupling strength (\tilde{g}_i).

The MVBP manifold $|f\rangle$ (with dimension \mathbf{d}) can be similarly expanded as, $|f\rangle = \sum_{mn, m \geq n} \Phi_{mn, f} |mn\rangle$. The restriction $m \geq n$ reduces $\mathbf{d} = \mathcal{N}(\mathcal{N} + 1)/2$. The MVBP eigenenergies are given by,

$$\begin{aligned} \Omega_f = & \sum_{mn, m' n'} \Phi_{nm, f} \left(\delta_{mm'} \Omega_{nn'} + \Omega_{nn'} \delta_{mm'} \right. \\ & \left. + \delta_{mn'} \Omega_{nm'} + \Omega_{n'm} \delta_{mn'} \right) \Phi_{n'm', f} \end{aligned} \quad (\text{A.6})$$

The nomenclature for Amide-I ($m = 1$) and Amide-I+II ($m = 2$) vibrations of NMA coupled to single cavity mode in local and polariton basis along with single (SE) and double excited (DE) polariton states are given in Table. ???. Tuning the cavity coupling allows us to control spectral structures of the *MVP* and *MVBP* manifolds and is illustrated using DQC in the following section.

A.1.2 The DQC signal for molecular vibrational polaritons

Assuming four temporally-well separated pulses given by, $\mathcal{E}(\mathbf{r}, t) = \sum_{i=1}^4 \mathcal{E}(t-t_i) e^{i\mathbf{k}_i \mathbf{r}_i - i\omega_i(t-t_i)} + c.c.$, the DQC signal is generated in the phase-matching direction $\mathbf{k}_{III} = \mathbf{k}_1 + \mathbf{k}_2 - \mathbf{k}_3$ [107]. In terms of time delay t_i , is given by,

$$\mathcal{S}(\Omega_3, \Omega_2, t_1) = \int_0^\infty \int_0^\infty dt_2 dt_3 e^{i\Omega_3 t_3} e^{\Omega_2 t_2} \mathcal{S}^{\mathbf{k}_{III}}(t_1, t_2, t_3), \quad (\text{A.7})$$

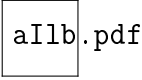
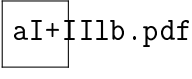
which can be expanded in vibrational molecular polariton eigenstates (Sec. A.1.1). Setting $t_1 = 0$ yields the expression for 2D signal,

$$\begin{aligned} \mathcal{S}(\Omega_3, \Omega_2, 0) &= \sum_{ee',f} \frac{1}{(\Omega_2 - \Omega_{fg} + i\gamma_{fg})} \\ &\quad \left[\frac{\mu_{e'f} \mu_{ge'} \mu_{fg} \mu_{ge}}{\Omega_3 - \Omega_{e'g} + i\gamma_{e'g}} \right. \\ &\quad \left. - \frac{1}{\mu_{ge'} \mu_{e'f} \mu_{fg} \mu_{eg}} \frac{1}{\Omega_3 - \Omega_{fe} + i\gamma_{fe}} \right]. \end{aligned} \quad (\text{A.8})$$

Note that the relevant eigenstates depend on the cavity coupling strengths (\tilde{g}) but have been neglected for clarity. μ_{ij} is the polariton transition dipole from states in manifold $j \rightarrow i$ while γ_{ij} is the respective dephasing.

A.2 Nomenclature

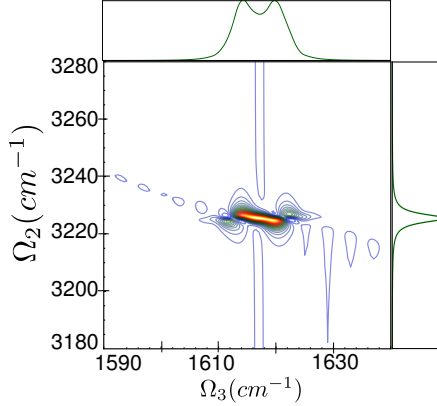
Table A.1: Nomenclature for eigenstates for Amide-I and Amide-I+Amide-II for NMA: ground state (G), singly excited states(SE) and doubly excited states (DE) in local and polariton basis. The cavity states for G, SE and DE are $|0\rangle$, $|1\rangle$ and $|2\rangle$ respectively.

Amide	Local basis				Polariton basis		
	G	SE	DE	Level scheme	G	SE	DE
I ($m = 1$)	$ g_a\rangle$	$ e_a\rangle$	$ f_a\rangle$	 aI1b.pdf	$ g\rangle$	$e_1 := e_a, 0\rangle$ $e_2 := g_a, 1\rangle$	$f_1 := e_a, 1\rangle$ $f_2 := g_a, 2\rangle$ $f_3 := f_a, 0\rangle$
I+II ($m = 2$)	$ g_a\rangle= g_b\rangle$	$ e_a\rangle; e_b\rangle$	$ f_a\rangle; f_b\rangle$	 aI+II1b.pdf	$ g\rangle$	$e_1 := g_a, e_b, 0\rangle$ $e_2 := e_a, g_b, 0\rangle$ $e_3 := g_a, g_b, 1\rangle$	$f_1 := g_a, e_b, 1\rangle$ $f_2 := g_a, f_b, 0\rangle$ $f_3 := e_a, e_b, 0\rangle$ $f_4 := e_a, g_b, 1\rangle$ $f_5 := f_a, g_b, 0\rangle$ $f_6 := g_a, g_b, 2\rangle$

A.3 Absorptive and dispersive parts of DQC

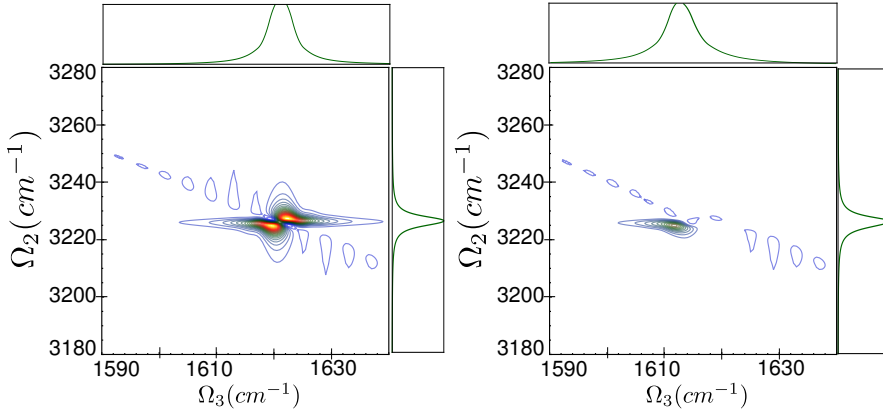
The absorptive (Im) and the dispersive (Re) parts of the DQC signals presented in main text are shown here. The doublets shown in the absorptive parts are due to anharmonicities.

A.3.1 Amide-I vibrations of NMA in IR cavity



Case I: No cavity Fig. A.1-A.2

Figure A.1: Imaginary part of DQC signals for Amide-I vibrations in NMA using Eq. A.8 and ladder diagrams (Fig. 3.2b): (a) $|\mathcal{S}_i(\Omega_3, \Omega_2, 0)|$ with resonance at $\Omega_{eg} = 1625\text{cm}^{-1}$, (b) $|\mathcal{S}_{ii}(\Omega_3, \Omega_2, 0)|$ with resonance at $\Omega_{fe} = 1617\text{cm}^{-1}$ and (c) $|\mathcal{S}(\Omega_3, \Omega_2, 0)|$ with resonances at $\Omega_{eg} = 1625\text{cm}^{-1}$ and $\Omega_{fe} = 1617\text{cm}^{-1}$. The linear projections along each axis is shown in green. For simplicity, cavity field vector \mathbf{e}_c is assumed to be mostly parallel to molecular vibrational transition dipole μ_m . Amide-I vibrations (ω_1) is resonant to cavity cutoff frequency $\omega_0 = 1625\text{cm}^{-1}$. The anharmonicity are assumed $\Delta_{11} = 15\text{cm}^{-1}$ (Table 3.1).



Case II: weak coupling regime with $\tilde{g} = 20\text{cm}^{-1}$ (Fig. A.3-A.4)

Figure A.4: Real part DQC signals using Eqn. A.8 and ladder diagrams (Fig. 3.2b): *Columns* (left-) $|\mathcal{S}_i(\Omega_3, \Omega_2, 0)|$ with resonance at Ω_{e1g} and Ω_{e2g} ; (middle-) $|\mathcal{S}_{ii}(\Omega_3, \Omega_2, 0)|$ with resonance at $\Omega_{f2,e2}, \Omega_{f2,e1}, \Omega_{f1,e2}, \Omega_{f3,e2}, \Omega_{f1,e1}, \Omega_{f3,e1}$; and (right-) $|\mathcal{S}(\Omega_3, \Omega_2, 0)|$ with respective resonances for Amide-I vibrations in NMA with cavity coupling *rows*: (a) 20cm^{-1} . The linear projections along each axis is shown in green. For simplicity, cavity field vector \mathbf{e}_c is assumed to be mostly parallel to molecular vibrational transition dipole μ_k . Amide-I vibrations (ω_1) is resonant to cavity cutoff frequency $\omega_0 = 1625\text{cm}^{-1}$. The anharmonicity are assumed $\Delta_{11} = 16\text{cm}^{-1}$ (Table 3.1))

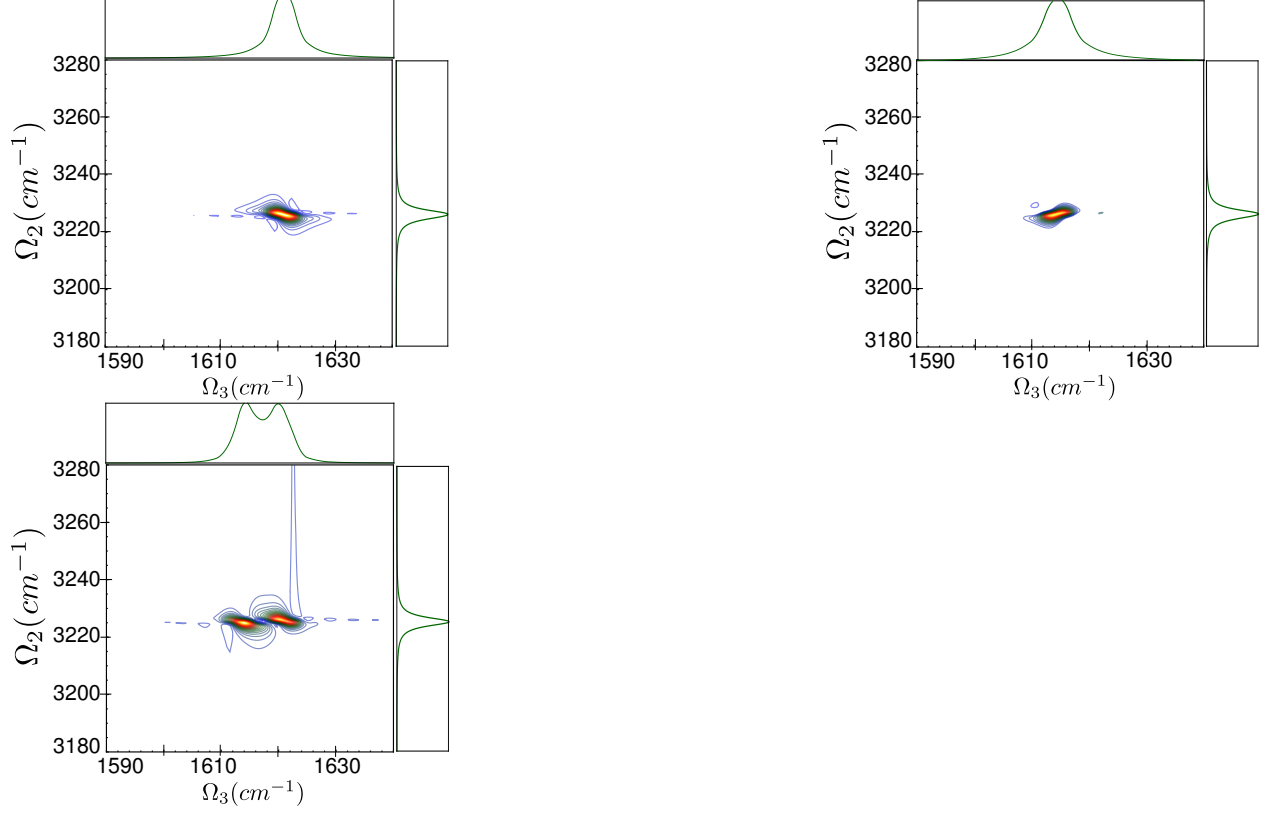


Figure A.2: Real part of DQC signals for Amide-I vibrations in NMA using Eq. A.8 and ladder diagrams (Fig. 3.2b): (a) $|\mathcal{S}_i(\Omega_3, \Omega_2, 0)|$ with resonance at $\Omega_{eg} = 1625\text{cm}^{-1}$, (b) $|\mathcal{S}_{ii}(\Omega_3, \Omega_2, 0)|$ with resonance at $\Omega_{fe} = 1617\text{cm}^{-1}$ and (c) $|\mathcal{S}(\Omega_3, \Omega_2, 0)|$ with resonances at $\Omega_{eg} = 1625\text{cm}^{-1}$ and $\Omega_{fe} = 1617\text{cm}^{-1}$. The linear projections along each axis is shown in green. For simplicity, cavity field vector \mathbf{e}_c is assumed to be mostly parallel to molecular vibrational transition dipole μ_m . Amide-I vibrations (ω_1) is resonant to cavity cutoff frequency $\omega_0 = 1625\text{cm}^{-1}$. The anharmonicity are assumed $\Delta_{11} = 15\text{cm}^{-1}$ (Table 3.1).

Case III: strong coupling regime with $\tilde{g} = 50\text{cm}^{-1}$ (Fig. A.5-A.6)

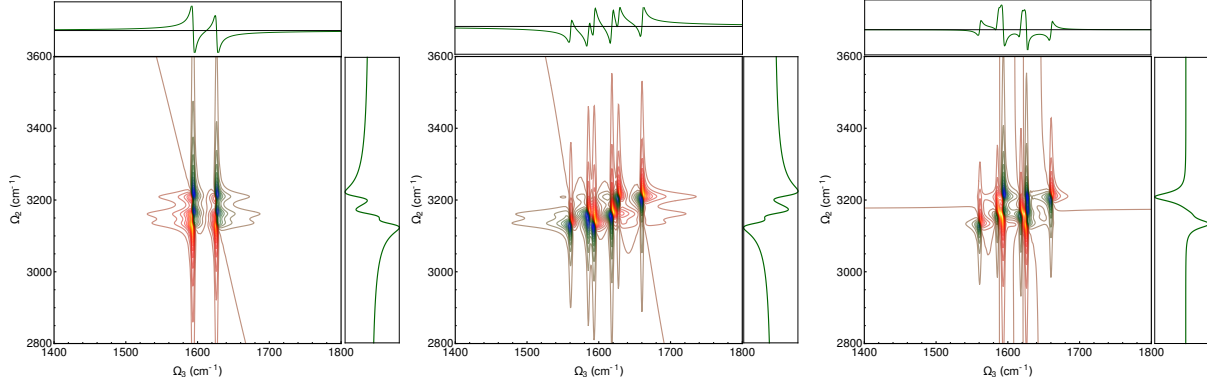
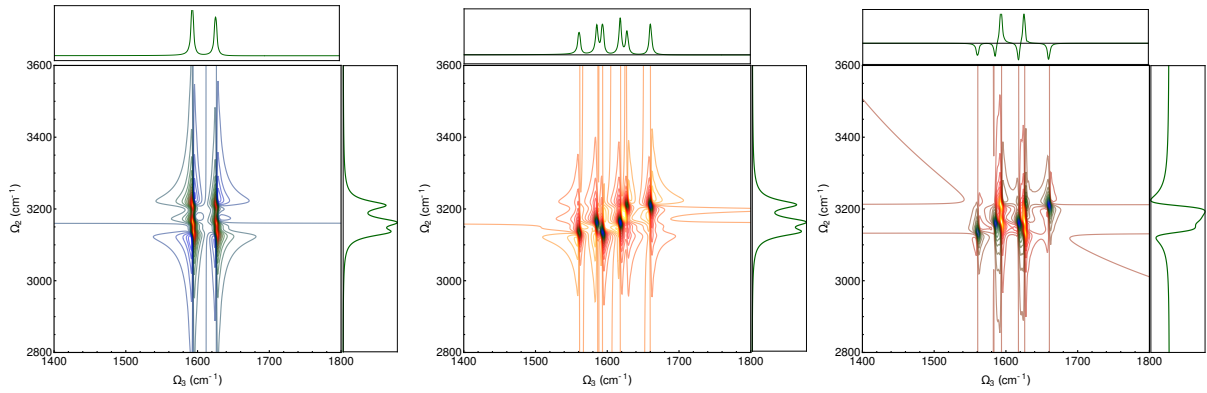


Figure A.3: Imaginary part DQC signals using Eqn. A.8 and ladder diagrams (Fig. 3.2b): *Columns* (left–) $|\mathcal{S}_i(\Omega_3, \Omega_2, 0)|$ with resonance at Ω_{e1g} and Ω_{e2g} ; (middle–) $|\mathcal{S}_{ii}(\Omega_3, \Omega_2, 0)|$ with resonance at $\Omega_{f2,e2}, \Omega_{f2,e1}, \Omega_{f1,e2}, \Omega_{f3,e2}, \Omega_{f1,e1}, \Omega_{f3,e1}$; and (right–) $|\mathcal{S}(\Omega_3, \Omega_2, 0)|$ with respective resonances for Amide-I vibrations in NMA with cavity coupling *rows*: (a) 20cm^{-1} . The linear projections along each axis is shown in green. For simplicity, cavity field vector \mathbf{e}_c is assumed to be mostly parallel to molecular vibrational transition dipole μ_k . Amide-I vibrations (ω_1) is resonant to cavity cutoff frequency $\omega_0 = 1625\text{cm}^{-1}$. The anharmonicity are assumed $\Delta_{11} = 16\text{cm}^{-1}$ (Table 3.1)



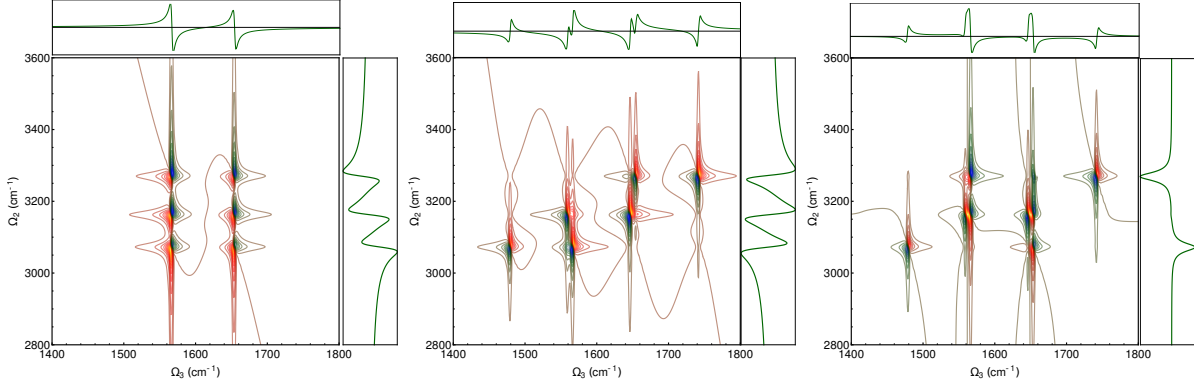


Figure A.5: Imaginary part DQC signals using Eqn. A.8 and ladder diagrams (Fig. 3.2b): *Columns* (left–) $|\mathcal{S}_i(\Omega_3, \Omega_2, 0)|$ with resonance at Ω_{e1g} and Ω_{e2g} ; (middle–) $|\mathcal{S}_{ii}(\Omega_3, \Omega_2, 0)|$ with resonance at $\Omega_{f2,e2}, \Omega_{f2,e1}, \Omega_{f1,e2}, \Omega_{f3,e2}, \Omega_{f1,e1}, \Omega_{f3,e1}$; and (right–) $|\mathcal{S}(\Omega_3, \Omega_2, 0)|$ with respective resonances for Amide-I vibrations in NMA with cavity coupling (a) 50cm^{-1} . The linear projections along each axis is shown in green. For simplicity, cavity field vector \mathbf{e}_c is assumed to be mostly parallel to molecular vibrational transition dipole μ_k . Amide-I vibrations (ω_1) is resonant to cavity cutoff frequency $\omega_0 = 1625\text{cm}^{-1}$. The anharmonicity are assumed $\Delta_{11} = 16\text{cm}^{-1}$ (Table 3.1)

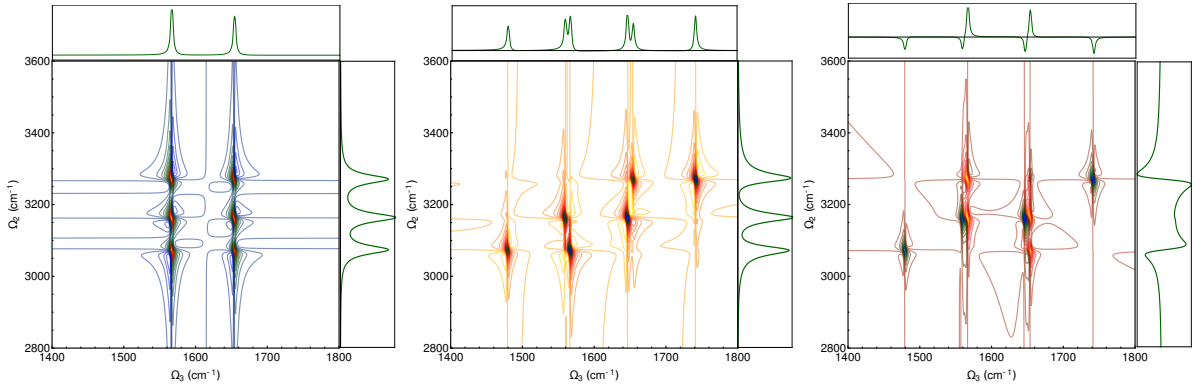


Figure A.6: Real part DQC signals using Eqn. A.8 and ladder diagrams (Fig. 3.1e): *Columns* (left–) $|\mathcal{S}_i(\Omega_3, \Omega_2, 0)|$ with resonance at Ω_{e1g} and Ω_{e2g} ; (middle–) $|\mathcal{S}_{ii}(\Omega_3, \Omega_2, 0)|$ with resonance at $\Omega_{f2,e2}, \Omega_{f2,e1}, \Omega_{f1,e2}, \Omega_{f3,e2}, \Omega_{f1,e1}, \Omega_{f3,e1}$; and (right–) $|\mathcal{S}(\Omega_3, \Omega_2, 0)|$ with respective resonances for Amide-I vibrations in NMA with cavity coupling *rows*: (a) 20cm^{-1} and (a) 50cm^{-1} . The linear projections along each axis is shown in green. For simplicity, cavity field vector \mathbf{e}_c is assumed to be mostly parallel to molecular vibrational transition dipole μ_k . Amide-I vibrations (ω_1) is resonant to cavity cutoff frequency $\omega_0 = 1625\text{cm}^{-1}$. The anharmonicity are assumed $\Delta_{11} = 16\text{cm}^{-1}$ (Table 3.1)

A.4 Amide-I+II of NMA in IR cavity

case II: weak coupling regime with $\tilde{g} = 10\text{cm}^{-1}$ (Fig. A.7-A.8)

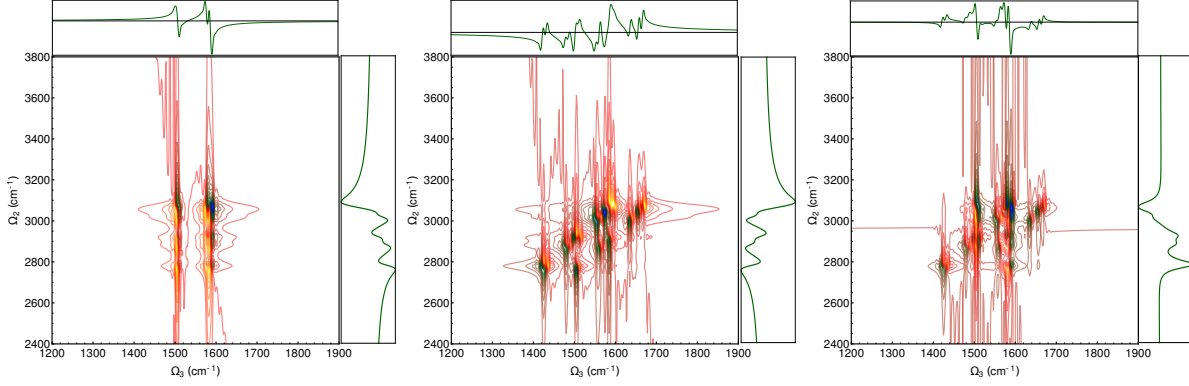
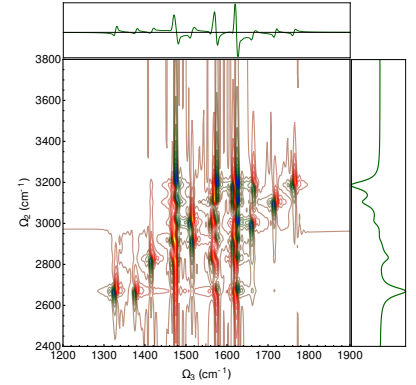


Figure A.7: Imaginary part of DQC signals for Amide-I+II vibrations in NMA using Eq. A.8 and ladder diagrams (Fig. 1e in main text): *Columns* : (left-) $|\mathcal{S}_i(\Omega_3, \Omega_2, 0)|$ with resonance at $\Omega_{e_{1g}}, \Omega_{e_{2g}}$ and $\Omega_{e_{3g}}$; (middle-) $|\mathcal{S}_{ii}(\Omega_3, \Omega_2, 0)|$ with resonance at $\Omega_{f_{1e_3}} \approx \Omega_{f_{1e_2}}, \Omega_{f_{3e_4}} \approx \Omega_{f_{4e_2}}, \Omega_{f_{2e_3}} \approx \Omega_{f_{2e_2}}, \Omega_{f_{1e_1}}, \Omega_{f_{3e_3}} \approx \Omega_{f_{3e_2}} = \Omega_{f_{4e_1}} = \Omega_{f_{6e_3}}, \Omega_{f_{6e_2}}, \Omega_{f_{5e_3}}, \Omega_{f_{2e_1}}, \Omega_{f_{5e_2}}, \Omega_{f_{3e_1}}, \Omega_{f_{6e_1}}, \Omega_{f_{5e_1}}$ and (right-) $|\mathcal{S}(\Omega_3, \Omega_2, 0)|$ with respective resonances with cavity couplings (*rows*) at 10cm^{-1} along Ω_3 , while peaks at $\Omega_{f_{1g}}, \Omega_{f_{2g}}, \Omega_{f_{3g}}, \Omega_{f_{4g}}, \Omega_{f_{5g}}$ and $\Omega_{f_{6g}}$ along Ω_2 . The linear projections along each axis is shown in green. For simplicity, cavity field vector \mathbf{e}_c is assumed to be mostly parallel to molecular vibrational transition dipole μ_m . Amide-I vibrations (ω_1) is resonant to cavity cutoff frequency $\omega_0 = 1625\text{cm}^{-1}$ and $\omega_2 = 1540\text{cm}^{-1}$. The anharmonicity are assumed $\Delta_{11} = 15\text{cm}^{-1}$ and $\Delta_{22} = 11\text{cm}^{-1}$ (Table 3.1)



case III: strong coupling regime with $\tilde{g} = 60\text{cm}^{-1}$ (Fig. A.9-A.10)

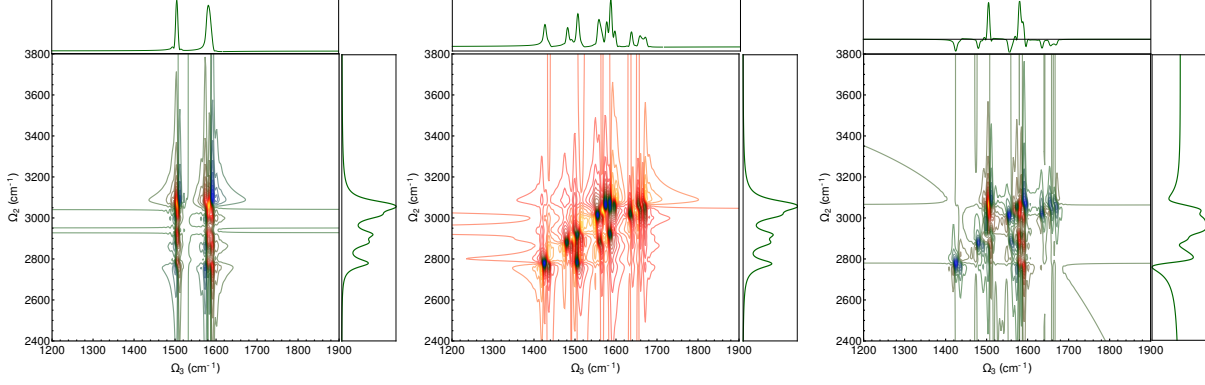
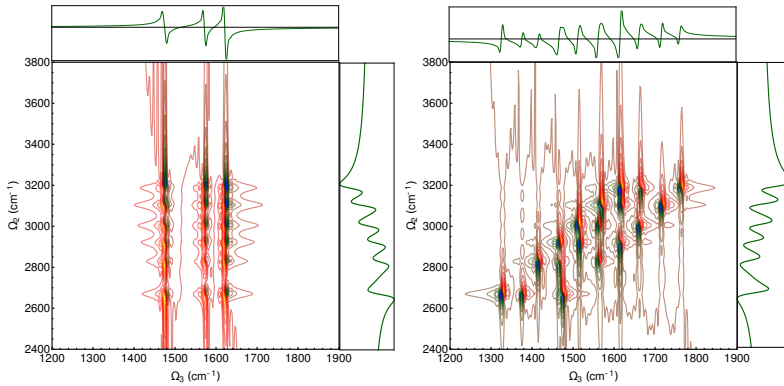


Figure A.8: Real part of DQC signals for Amide-I+II vibrations in NMA using Eq. A.8 and ladder diagrams (Fig. 3.1e): *Columns* : (left-) $|\mathcal{S}_i(\Omega_3, \Omega_2, 0)|$ with resonance at $\Omega_{e_{1g}}, \Omega_{e_{2g}}$ and $\Omega_{e_{3g}}$; (middle-) $|\mathcal{S}_{ii}(\Omega_3, \Omega_2, 0)|$ with resonance at $\Omega_{f_{1e_3}} \approx \Omega_{f_{1e_2}}, \Omega_{f_{3e_4}} \approx \Omega_{f_{4e_2}}, \Omega_{f_{2e_3}} \approx \Omega_{f_{2e_2}}, \Omega_{f_{1e_1}}, \Omega_{f_{3e_3}} \approx \Omega_{f_{3e_2}} = \Omega_{f_{4e_1}} = \Omega_{f_{6e_3}}, \Omega_{f_{6e_2}}, \Omega_{f_{5e_3}}, \Omega_{f_{2e_1}}, \Omega_{f_{5e_2}}, \Omega_{f_{3e_1}}, \Omega_{f_{6e_1}}, \Omega_{f_{5e_1}}$ and (right-) $|\mathcal{S}(\Omega_3, \Omega_2, 0)|$ with respective resonances with cavity couplings at 60cm^{-1} along Ω_3 , while peaks at $\Omega_{f_{1g}}, \Omega_{f_{2g}}, \Omega_{f_{3g}}, \Omega_{f_{4g}}, \Omega_{f_{5g}}$ and $\Omega_{f_{6g}}$ along Ω_2 . The linear projections along each axis is shown in green. For simplicity, cavity field vector \mathbf{e}_c is assumed to be mostly parallel to molecular vibrational transition dipole μ_m . Amide-I vibrations (ω_1) is resonant to cavity cutoff frequency $\omega_0 = 1625\text{cm}^{-1}$ and $\omega_2 = 1540\text{cm}^{-1}$. The anharmonicity are assumed $\Delta_{11} = 15\text{cm}^{-1}$ and $\Delta_{22} = 11\text{cm}^{-1}$ (Table 3.1) .

Figure A.9: Imaginary part of DQC signals using Eqn. A.8 and ladder diagrams (Fig. 1e in maintext):(a) $\mathcal{S}_i(\Omega_3, \Omega_2, 0)$ with resonance at $\Omega_{e_{1g}}, \Omega_{e_{2g}}$ and $\Omega_{e_{3g}}$ (b) $\mathcal{S}_{ii}(\Omega_3, \Omega_2, 0)$ with resonance at $\Omega_{f_{1e_3}} \approx \Omega_{f_{1e_2}}, \Omega_{f_{3e_4}} \approx \Omega_{f_{4e_2}}, \Omega_{f_{2e_3}} \approx \Omega_{f_{2e_2}}, \Omega_{f_{1e_1}}, \Omega_{f_{3e_3}} \approx \Omega_{f_{3e_2}} = \Omega_{f_{4e_1}} = \Omega_{f_{6e_3}}, \Omega_{f_{6e_2}}, \Omega_{f_{5e_3}}, \Omega_{f_{2e_1}}, \Omega_{f_{5e_2}}, \Omega_{f_{3e_1}}, \Omega_{f_{6e_1}}, \Omega_{f_{5e_1}}$ and (c) $\mathcal{S}_i(\Omega_3, \Omega_2, 0)$ with respective resonances for Amide-I+II vibrations in NMA with cavity coupling 20cm^{-1} along Ω_3 , while peaks at $\Omega_{f_{1g}}, \Omega_{f_{2g}}, \Omega_{f_{3g}}, \Omega_{f_{4g}}, \Omega_{f_{5g}} = \Omega_{f_{6g}}$ along Ω_2 in (a)-(c). The linear projections along each axis is shown in green. For simplicity, cavity field vector \mathbf{e}_c is assumed to be mostly parallel to molecular vibrational transition dipole μ_k . Amide-I vibrations (ω_1) is resonant to cavity cutoff frequency $\omega_0 = 1625\text{cm}^{-1}$ and $\omega_2 = 1510\text{cm}^{-1}$. The anharmonicity are assumed $\Delta_{11} = 16\text{cm}^{-1}$ and $\Delta_{22} = 24\text{cm}^{-1}$ (Table 3.1).



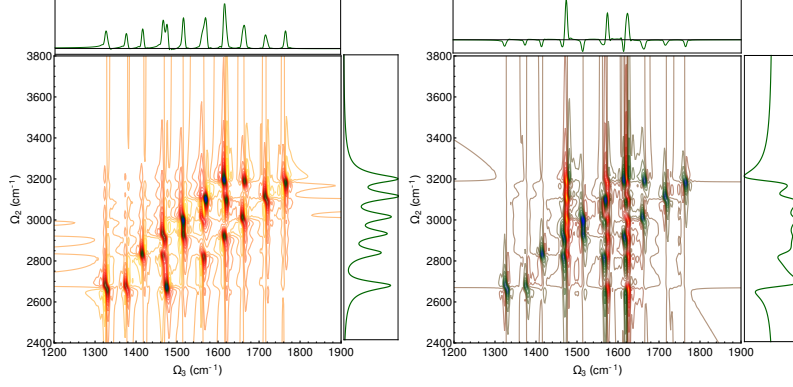
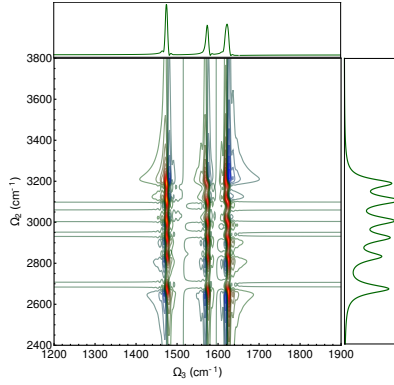
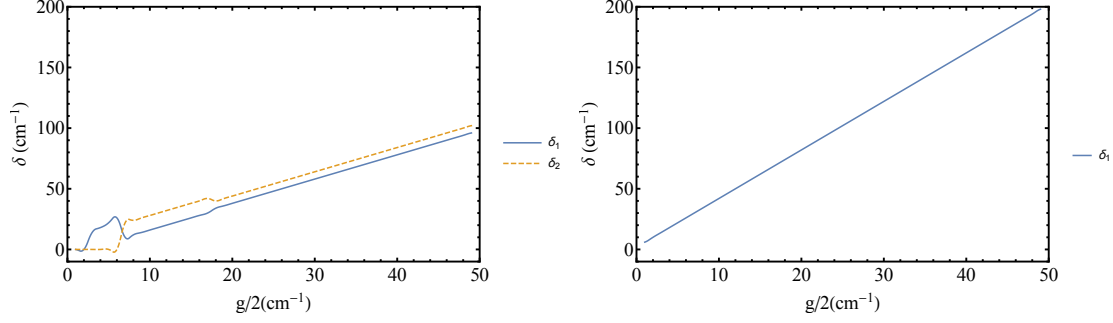


Figure A.10: Real part of DQC signals using Eqn. A.8 and ladder diagrams (Fig. 3.2b):(a) $\mathcal{S}_i(\Omega_3, \Omega_2, 0)$ with resonance at Ω_{e_1g} , Ω_{e_2g} and Ω_{e_3g} (b) $\mathcal{S}_{ii}(\Omega_3, \Omega_2, 0)$ with resonance at $\Omega_{f_1e_3} \approx \Omega_{f_1e_2}$, $\Omega_{f_3e_4} \approx \Omega_{f_4e_2}$, $\Omega_{f_2e_3} \approx \Omega_{f_2e_2}$, $\Omega_{f_1e_1}$, $\Omega_{f_3e_3} \approx \Omega_{f_3e_2} = \Omega_{f_4e_1} = \Omega_{f_6e_3}$, $\Omega_{f_6e_2}$, $\Omega_{f_5e_3}$, $\Omega_{f_2e_1}$, $\Omega_{f_5e_2}$, $\Omega_{f_3e_1}$, $\Omega_{f_6e_1}$, $\Omega_{f_5e_1}$ and (c) $\mathcal{S}_i(\Omega_3, \Omega_2, 0)$ with respective resonances for Amide-I+II vibrations in NMA with cavity coupling 20cm^{-1} along Ω_3 , while peaks at $\Omega_{f_1g}, \Omega_{f_2g}, \Omega_{f_3g}, \Omega_{f_4g}, \Omega_{f_5g} = \Omega_{f_6g}$ along Ω_2 in (a)-(c). The linear projections along each axis is shown in green. For simplicity, cavity field vector \mathbf{e}_c is assumed to be mostly parallel to molecular vibrational transition dipole μ_k . Amide-I vibrations (ω_1) is resonant to cavity cutoff frequency $\omega_0 = 1625\text{cm}^{-1}$ and $\omega_2 = 1510\text{cm}^{-1}$. The anharmonicity are assumed $\Delta_{11} = 16\text{cm}^{-1}$ and $\Delta_{22} = 24\text{cm}^{-1}$ (Table 3.1).





A.5 Peak splitting for Amide-I vibrations of NMA in optical cavity

Using the nomenclature $\delta_1 = \omega_{f_2e_2} - \omega_{f_1e_1}$, $\delta_2 = \omega_{f_2e_2} - \omega_{f_1e_1}$, $\delta_1 = \omega_{f_2e_2} - \omega_{f_1e_1}$, $\delta_1 = \omega_{f_2e_2} - \omega_{f_1e_1}$ and $\delta_1 = \omega_{f_2e_2} - \omega_{f_1e_1}$ the peak splitting for Amide-I vibrations of NMA in optical cavity is shown in Fig.1a of main text.

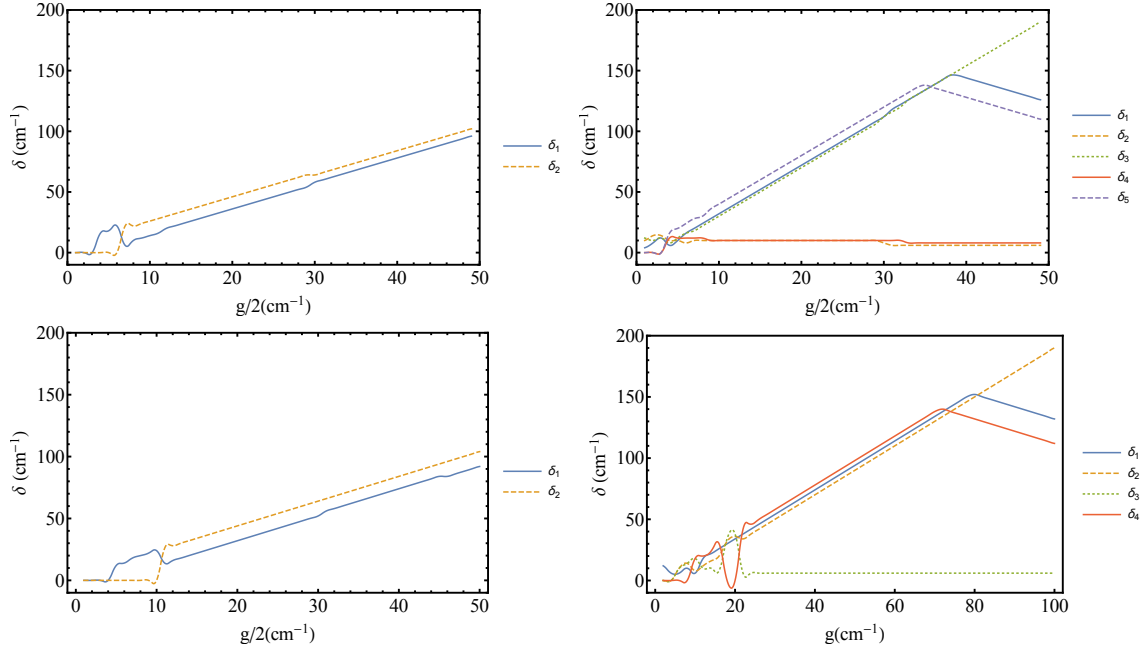
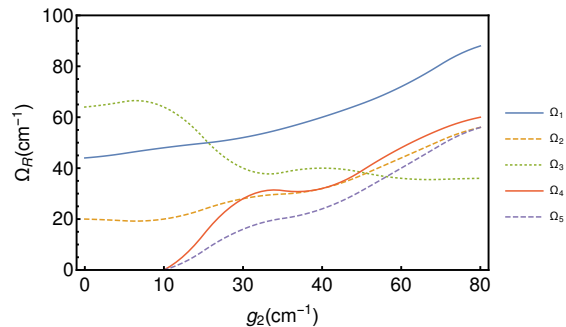


Figure A.11: Rabi splitting for nearest peaks in Fig. A.1-A.5. The nomenclature used is as follows, $\delta_1 = \omega_{f_2e_2} - \omega_{f_1e_1}$, $\delta_2 = \omega_{f_2e_2} - \omega_{f_1e_1}$, $\delta_1 = \omega_{f_2e_2} - \omega_{f_1e_1}$, $\delta_1 = \omega_{f_2e_2} - \omega_{f_1e_1}$ and $\delta_1 = \omega_{f_2e_2} - \omega_{f_1e_1}$



A.6 Peak splitting for Amide-I+II vibrations of NMA in optical cavity

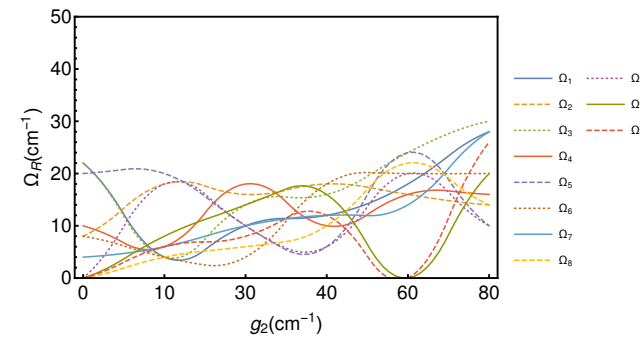
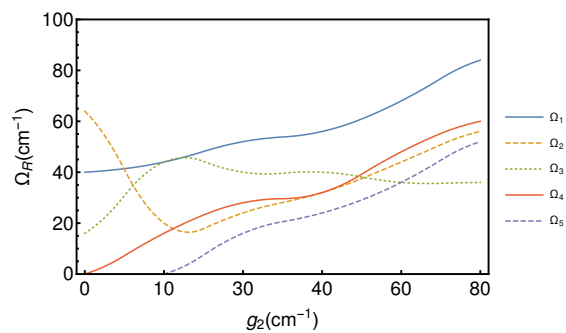
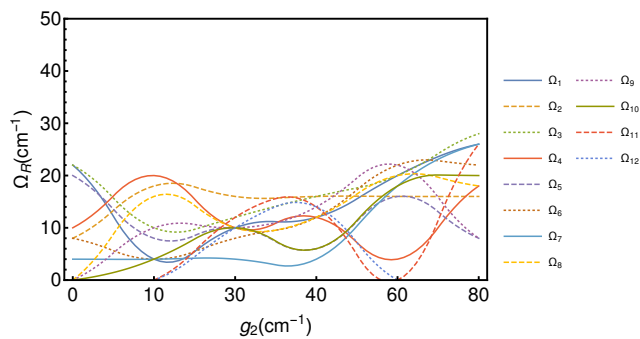
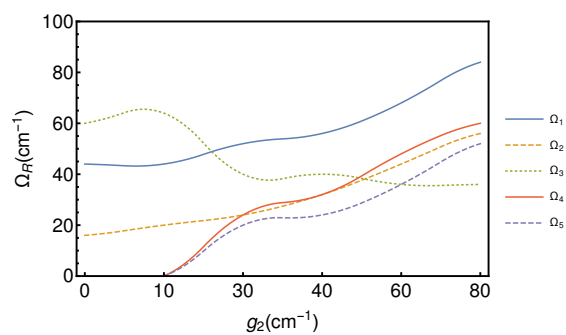
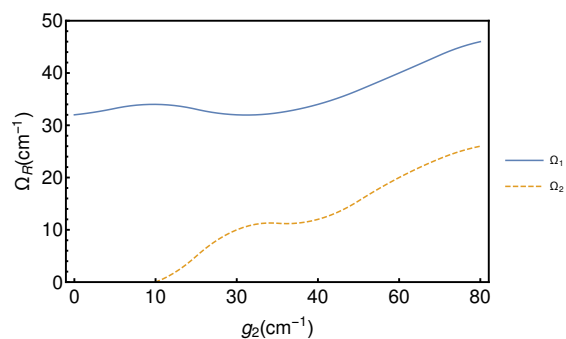


Figure A.12: Rabi splitting for nearest peaks for Amide-I+II of NMA in single mode cavity corresponding to Fig. A.7-A.9.

Appendix B

Supplementary to Chapter 4

B.1 Introduction

Usually bosonic commutation relations are imposed for molecular polaritons imposes bosonic commutation relations for polariton creation(annihilation) operators, i.e., $[\hat{p}_i^\dagger, \hat{p}_j] = \delta_{ij}$ where, $\hat{p}_i^\dagger(\hat{p}_j)$ are polariton creation (annihilation) operators for modes i and j respectively. This constraint allows for usual predictions anharmonicities of vibrational molecular polaritons [9], as well as electronic spectroscopic measurements for single molecules confined in sub-wavelength optical cavities and in controlling other physical and chemical properties of molecules.

This constraint on the commutation relation fails when the one incorporates the non-bosonic nature of exciton-exciton interactions for molecules in the optical cavity. The molecular polariton hamiltonian including the polariton-polarion interaction term is given by (c.f.2),

$$H_p(g) = \sum_i^N \Omega_i(g) \hat{p}_i^\dagger \hat{p}_i + \sum_{ij,kl}^N \tilde{V}_{ij,kl}(g) \hat{p}_i^\dagger \hat{p}_j^\dagger \hat{p}_k \hat{p}_l, \quad (\text{B.1})$$

where, $\Omega_i(g)$ is the coupling dependent eigenenergies of sites i in the polariton manifold, and $\tilde{V}_{ij,kl}(g)$ is polariton-polariton interaction term. It suffices to split the second term in Eqn. (B.1) in terms of onsite interaction terms ($i = j = k = l$) and two site interaction ($i = k, j = l$) to capture essential physics. Thus, our model hamiltonian for interacting molecular polaritons is simplified to,

$$\begin{aligned}
H_p(g) &= \sum_i^N \Omega_i(g) \hat{p}_i^\dagger \hat{p}_i + \sum_i^N \tilde{\Delta}_i(g) \hat{p}_i^\dagger \hat{p}_i^\dagger \hat{p}_i \hat{p}_i \\
&+ \sum_{ij}^N \tilde{K}_{ij}(g) \hat{p}_i^\dagger \hat{p}_j^\dagger \hat{p}_i \hat{p}_j
\end{aligned} \tag{B.2}$$

¹ In this letter, we first modify Eqn (B.1) to include the effect of of derive the structure of polariton-polariton interaction term in the molecular polariton hamiltonian when we release the constraint of operators being bosonic, but instead treat them as q -deformed. We then use the collective polariton oscillator method developed in Chapter 2 to directly measure the effects of the polariton-polariton scattering as we vary cavity coupling g and the deformation parameter α . In this letter, we will study how the energy terms are modified due to manybody interactions of the q - deformed polaritons. For simplicity, we will restrict ourselves to the correction due to interacting polaritons when $N_i = 1$. The solution to this issue unfolds in three steps: a) finding the exact change in the nonlinear term in the molecular polariton hamiltonian, b) finding the exact g dependence on the q , and, c) direct measurement of this effect using quasiparticle representation of multidimensional spectroscopy for molecular polaritons.

As shown in the schematic within (Fig 1.2, the cavity photon is confined along k_z direction allowing the resulting polariton to be two dimensional at most. This allows us to recast,

¹For $N > 5$ there is no closed analytical form for either $\Omega_i(g)$ or $\tilde{V}_{ij,kl}(g)$ and we must resort to numerical methods.

$\tilde{V}_{ij,kl}(g)$ which differs from exciton-exciton interaction $U_{ij,kl}$ by the transformation, $\tilde{V}_{ij,kl}(g) = U_{ij,kl}X_k^*X_l^*X_mX_n$, with Hopfield coefficients X_m (for mode $m \in \{i, j, k, l\}$).

B.1.1 Modification on energy terms dues to q

We start with interacting polariton Hamiltonian where we use $\hat{\pi}_i^\dagger(\hat{\pi}_i)$ as deformed polariton creation (annihilation) operators,

$$H = \sum_i \Omega_i \hat{\pi}_i^\dagger \hat{\pi}_i + \frac{1}{2} \sum_{\langle i,j \rangle} \tilde{V}_{ij,ij} \hat{\pi}_i^\dagger \hat{\pi}_j^\dagger \hat{\pi}_i \hat{\pi}_j + \frac{1}{2} \sum_i \tilde{U}_{ii,ii} \hat{\pi}_i^\dagger \hat{\pi}_i^\dagger \hat{\pi}_i \hat{\pi}_i, \quad (\text{B.3})$$

where, Ω_i is the energy of the i^{th} polariton branch, $\tilde{V}_{ij,ij}$ is the two-site polariton interactions at sites i and j and $\tilde{U}_{ii,ii}$ is on-site polariton-polariton interaction for site i . For simplicity, we only consider on site interaction term, and derive exact expressions for the changes on $\tilde{U}_i \equiv \tilde{U}_{ii,ii}$ as cavity coupling g is varied which in term changes the deformation parameter q . We explore the effects of the changing number of polaritons in each branch and measure Double Quantum Coherence using quasiparticle description of the signal described in Chapter 2 to reveal the exact breaking point of the cooperativity that often scales as \sqrt{N} . To express the third term in Eqn. (B.3), we need to rewrite it using Eqn. (B.25). By substituting $k = 2$ we can establish the relation between the normal ordered polartion operators and functions of polariton number \hat{N}_i .

$$\sum_i \tilde{U}_i \hat{\pi}_i^\dagger \hat{\pi}_i^\dagger \hat{\pi}_i \hat{\pi}_i = \sum_{m=1}^2 \tilde{U}_i \hat{S}(2, m, \hat{N}_i) [\hat{N}_i]^m, \quad (\text{B.4})$$

where, $\hat{N}_i = \hat{\pi}_i^\dagger \hat{\pi}_i$, and

$$\hat{S}(2, m, \hat{N}_i) = q^{-1} q^{-(2-m)\hat{N}_i} \xi(2, m). \quad (\text{B.5})$$

$\xi(2, m)$ has properties of Stirling number of first kind. We thus have,

$$\sum_i \tilde{U}_i \hat{\pi}_i^\dagger \hat{\pi}_i^\dagger \hat{\pi}_i \hat{\pi}_i = \sum_{m=1}^2 \tilde{U}_i q^{-1} q^{-(2-m)\hat{N}_i} \xi(2, m) [\hat{N}_i]^m. \quad (\text{B.6})$$

Replacing $[\hat{N}_i]^m$ with proper q-analytical form gives us,

$$\sum_i \tilde{U}_i \hat{\pi}_i^\dagger \hat{\pi}_i^\dagger \hat{\pi}_i \hat{\pi}_i = \sum_i \xi(2, 1) \tilde{U}_i \hat{\pi}_i^\dagger \hat{\pi}_i^\dagger \hat{\pi}_i \hat{\pi}_i q^{(\hat{N}_i)+1} [\hat{N}_i] + \sum_i \xi(2, 2) \tilde{U}_i [\hat{N}_i]^2. \quad (\text{B.7})$$

We next substitute operator form of Eqn. (B.11) in Eqn. (B.7) for $[\hat{N}_i]$ in the first term of Eqn. B.7 to get,

$$\sum_i \xi(2, 1) \tilde{U}_i \hat{\pi}_i^\dagger \hat{\pi}_i^\dagger \hat{\pi}_i \hat{\pi}_i q^{(\hat{N}_i)+1} [\hat{N}_i] = \sum_i \tilde{U}_i \frac{\log[q]}{q^2} \hat{N}_i (\coth[\alpha] - 1) \{ \hat{N}_i \log[q] + 1 \} \quad (\text{B.8})$$

where, we used $\xi(2, 1) = -1$ and substituted $q \rightarrow e^{-\alpha}$ and then expanded Eqn. (B.7) upto second order in \hat{N}_i to incorporate doubly excited state information. Similar treatment to the second term in Eqn. (B.7) gives,

$$\sum_i \xi(2, 2) \tilde{U}_i [\hat{N}_i]^2 = - \sum_i \tilde{U}_i \hat{N}_i^2 [\alpha] \log[q] \quad (\text{B.9})$$

because $\xi(1, 1) = 1$. Now collecting the terms with linear and quadratic dependence in \hat{N}_i gives us following simplified form for the on-site polariton-polariton interaction terms so that we can use ratio of \hat{U}_i/g as dimensionless structure parameter to quantify q .

$$\sum_i \tilde{U}_i \hat{\pi}_i^\dagger \hat{\pi}_i^\dagger \hat{\pi}_i \hat{\pi}_i = \sum_i \tilde{U}_i \frac{\log[q]}{q^2} (\coth[\alpha] - 1) \hat{N}_i - \sum_i \tilde{U}_i \log[q] \hat{N}_i^2 \left[(\coth[\alpha] - 1) \frac{\log[q]}{q^2} + [\alpha] \right] \quad (\text{B.10})$$

B.2 Useful relations for q-deformed algebras

Majority of physics literature and quantum groups on q - analysis uses following bracketed number (operator),

$$[x]_i = \frac{q^{x_i} - q^{-x_i}}{q - q^{-1}}. \quad (\text{B.11})$$

A straightforward realization of such deformed algebra can be achieved using representations spanned by Fock space on which the deformed polariton creation (annihilation) ($\hat{\pi}^\dagger, \hat{\pi}$) operators are defined with following general form,

$$\hat{\pi}_i |n\rangle_i = \sqrt{[n]_i} |n-1\rangle_i \quad \hat{\pi}_i^\dagger \sqrt{[n+1]_i} |n+1\rangle_i \quad (\text{B.12})$$

$$\hat{\pi}_i^\dagger \hat{\pi}_i |n\rangle_i = \hat{N}_i |n\rangle_i = n |n\rangle_i. \quad (\text{B.13})$$

Furthermore, a simple algebra shows that,

$$\hat{\pi}_i^\dagger \hat{\pi}_j = \delta_{ij} [\hat{N}_i] \quad \hat{\pi}_j \hat{\pi}_i^\dagger = \delta_{ij} [\hat{N}_i + 1]. \quad (\text{B.14})$$

Out of convinience we can choose to have following reording relation for the deformed polaritons,

$$\hat{\pi}_i \hat{\pi}_j^\dagger - q^{-1} \hat{\pi}_j^\dagger \hat{\pi}_i = \delta_{ij} q^{\hat{N}_i} \quad (\text{B.15})$$

For general deformation, an for arbitrary power (k) of polariton number operators \hat{N}_i , we hvae following generalized commutation relation,

$$[\hat{\pi}^k, \hat{\pi}^\dagger] = \delta_{ij} \phi(k, \hat{N}_i) \hat{\pi}^{k-1}, \quad (\text{B.16})$$

where $\phi(k, \hat{N}_i)$ is bounded for $k > 1$ and is given by,

$$\phi(k, \hat{N}_i) = \frac{1}{q - q^{-1}} = [k] q^{-\hat{N}_i}. \quad (\text{B.17})$$

For arbitrary power of polariton number, \hat{N}_i , we have,

$$[\hat{N}_i]^m = \sum_{k=1}^m (\hat{\pi}^\dagger)^k \hat{S}(m, k, \hat{N}_i), \hat{\pi}_i^k. \quad (\text{B.18})$$

due to [Kibler] [135]. Here, $\hat{S}(m, k, \hat{N}_i)$ is operator values Stirling number with following recursion relation,

$$\hat{S}(m + 1, k, \hat{N}_i) = q^{k-1} \hat{S}(m, k - 1, \hat{N}_i + 1) + \hat{S}(m, k, \hat{N}_i)[k]. \quad (\text{B.19})$$

Clearly, $\hat{S}(m, k, \hat{N}_i)$ depends on \hat{N}_i which implies that Eqn. B.19 is not normally ordered. In order to explain the polariton-polariton scattering terms we wish to have the quadratic interaction terms normally ordered. In order to do so, a simple decomposition of the operator valued Stirling number into product of Stirling number of second kind $\hat{S}^{(2)}(m, k)$ and a function of number operator can be achieved. It takes the following form,

$$\hat{S}(m, k, \hat{N}_i) = q^{k(k-1)/2} q^{-(m-k)\hat{N}_i} \hat{S}^{(2)}(m, k) \quad (\text{B.20})$$

We further have following recursion relation,

$$\hat{S}^{(2)}(m + 1, k) = q^{-(m-k+1)} \hat{S}^{(2)}(m, k - 1) + k \hat{S}^{(2)}(m, k), \quad (\text{B.21})$$

bounded by unity at $\hat{S}^{(2)}(1, 1)$. Finally in order to express $(\hat{\pi}^\dagger)^k (\hat{\pi})^k$ in normal order in terms of $[\hat{N}_i]$ so that we can see exact dependence of $[\hat{N}_i]$ on polariton-polariton terms. To do so, we need following relations of q-analog numbers,

$$[a + b] = q^b ([a] + q^{-a} [b]) \quad (\text{B.22})$$

$$[b] = (-1)^{-b}[b] \quad (\text{B.23})$$

$$[a - b] = q^{(-b)}([a] - q^{-1(a-b)}[b]). \quad (\text{B.24})$$

Using Eqns (B.16)–B.22, we get,

$$(\hat{\pi}_i^\dagger)^k (\hat{\pi}_i)^k = \sum_{m=1}^k \hat{S}(k, m, \hat{N}_i) [\hat{N}_i]^m \quad (\text{B.25})$$

We further note that,

$$(\hat{\pi}_i^\dagger)^{k+1} (\hat{\pi}_i)^{k+1} = \hat{\pi}_i^k [\hat{N}_i] \hat{\pi}_i^k = (\hat{\pi}_i^\dagger)^k (\hat{\pi}_i)^k [\hat{N}_i - k] \quad (\text{B.26})$$

And,

$$\hat{S}(k + 1, m, \hat{N}_i) = q^{-k} \hat{S}(k, m - 1, \hat{N}_i) - q^{-(\hat{N}_i + k)} \hat{S}(k, m, \hat{N}_i). \quad (\text{B.27})$$

We next introduce \hat{N}_i independent Stirling number to get,

$$\hat{S}(k, m, \hat{N}_i) = q^{-k(k-1)/2} q^{-1(k-m)\hat{N}_i} \xi(k, m), \quad (\text{B.28})$$

where,

$$\xi(k+1, m) = \xi(k, m-1) - q^k [k] \xi(k, m) \quad (\text{B.29})$$

Unfortunately, the exponential dependence on \hat{N}_i for the operator values Stirling number, we cannot express the normal ordered polariton operators as polynomials of \hat{N}_i but have been able to write them as function of \hat{N}_i . Furthermore, the orthonormality of the transformations used is satisfied by following condition,

$$\sum_{m=1}^k \xi(k, m) (q^{-k'(k'-m)} \hat{S}^{(2)}(m, k')) = \delta(k, k') \quad (\text{B.30})$$

B.3 Thermal distribution of q-deformed polaritons

In Chapter ??, we detailed the methods of observing effects of q-deformed polariton-polariton scattering and its effects in singly and doubly excited states. We then used, quasiparticle method developed in Chapter 2 to compute the double quantum coherence signal. In order to connect this thesis to already well established nonlinear spectroscopy developed in [10], we need to first be able to compute initial density matrix at thermal equilibrium $\rho_0(t_0)$. Once we have this, we can use Eqn.5.2 in [10].

We start with defining polaritons as q -deformed bosons $(\hat{\pi}^\dagger, \hat{\pi})$ with following commutation relations,

$$[N_i, \hat{\pi}_i^\dagger] = \hat{\pi}_i^\dagger \quad [N_i, \hat{\pi}_i] = -\hat{\pi}_i \quad (\text{B.31})$$

$$\hat{\pi}_i^\dagger \hat{\pi}_j = \delta_{ij} \quad \hat{\pi}_j \hat{\pi}_i^\dagger = \delta_{ij} [N_i + 1], \quad (\text{B.32})$$

where the bracket numbers $[x]$ (or operators) are defined using q -analogs given by,

$$[x] = \frac{q^x - q^{-x}}{q - q^{-1}}. \quad (\text{B.33})$$

An geometrically more rigorous way to realize deformed algebras would be to replace the Lie algebra acting on usual bosonic operators with Hopf algebra which could provide a more intricate structural understanding of the deformed polaritons. We choose a simpler route by assuming the polaritons as quasiparticles as done in seminal work by [146].

We wish to establish a thermal distribution for non-interacting (weakly-interacting) polaritons and calculate the expected number of polaritons for two dimensions which is most relevant for molecular polaritons confined in optical cavities where strong coupling regimes are easily achievable [50, 147].

To this end, we start with a simple non-interacting deformed polariton hamiltonian,

$$H = \sum_i \Omega_i \hat{\pi}_i^\dagger \hat{\pi}_i, \quad (\text{B.34})$$

where i^{th} polaritons are indexed by i . We have incorporated the chemical potentials μ_i (that depend on deformation parameter q) in energies Ω_i itself for simplicity. We next define the mean occupation number as exponents on the deformation parameter q ,

$$q^{\sigma f_i} = \frac{1}{\mathcal{Z}} \langle e^{-\beta H} q^{\sigma N_i} \rangle. \quad (\text{B.35})$$

Here, $\langle \dots \rangle$ denotes the thermal expectation value, $\mathcal{Z} = e^{-\beta H}$, and $\beta = \frac{1}{K_b T}$ with K_b as boltzman constant and T as temperature for $\sigma \in \{-1, +1\}$

Upon using the defination of bracket numbers Eqn B.33 and properties in Eqn B.31 we get,

$$[f_i] = \frac{1}{\mathcal{Z}} \langle e^{-\beta H} [N_i] \rangle. \quad (\text{B.36})$$

. In case where the mapping between the usual Hopfield coefficients and q -deformation parameters exists, it is easy to see that only the cases when $q \in R^+$ is physically relevant. In case that $q \in S^1$, topological deformation may be possible allowing for more complex physics for molecular polaritons.

Restricting ourselves to domain of positive real numbers R^+ , using cyclic property of trace and repeated use of Eqn B.31 allows us to write a recursive relation for $[f_i]$ as,

$$[f_i + 1] = [f_i] \cosh[\log[q]] + \cosh[f_i \log[q]] \quad (\text{B.37})$$

and,

$$[f_i] = \frac{\cosh[f_i \log[q]]}{\exp[\beta H] - \cosh[\log[q]]} \quad (\text{B.38})$$

In the limit, $q \rightarrow 1$ Eqn. B.37 tends to usual bosonic distribution, $\frac{1}{e^{\beta H} - 1}$. For our purposes,

$$f_i = \frac{1}{\log[q]} \tanh^{-1} \left[\frac{\sinh[\log[q]]}{e^{\beta H} - \cosh[\log[q]]} \right] \quad (\text{B.39})$$

It can be seen that f_i exhibits multiplicative inversion symmetry, i.e., $f_i(q) = f_i(q^{-1})$. Thus, it suffices to chose either $q > 1$ or $0 < q < 1$ without losing physics. Though upon calculations in terms of Hopfield coefficients, $q < 1$, choice of $q > 1$ guarantes series convergence.

$$f_i = \sum_{j=1}^{\infty} \frac{1 - \exp[-2j \log[q]]}{2j \log[q]} \exp[-j\beta(\Omega_i - \mu_0)], \quad (\text{B.40})$$

where, μ_0 is the chemical potential of undeformed polariton. Since, $\Omega_i - \mu_0 >$ is always satisfied, the series converges when $q > 1$.

In order to compute the thermal density we need to promote the sum (in Eqn. B.40 to an integral weighted by continuum energy ω ,

$$J_i = \int_0^{\infty} \omega^i f(\omega) d\omega. \quad (\text{B.41})$$

For, $i > -1$, we have,

$$\begin{aligned}
 J_i &= \Gamma(i+1)\beta^{-(i+1)}s(n+1), \\
 s(n+1) &= \frac{1}{2\log[q]} \sum_{j=1}^{\infty} \frac{1}{j^{i+2}} \frac{1 - \exp[-2j\log[q]]}{2j\log[q]} \exp[-j\beta(\Omega_i - \mu_0)].
 \end{aligned} \tag{B.42}$$

Where, Γ is Euler gamma function. For undeformed chemical potential $\mu_0 \leq 0$ and $q > 1$ the series expansion $s(i+1)$ always converges.

We are now in position to define the thermal density ρ_0 for two dimensional molecular polariton based on deformed commutation relations [146],

$$\rho_0 = 2d\sqrt{\pi}\Gamma(2)^{-1}\beta^{-1}m_p s(1), \tag{B.43}$$

where, d is the degeneracy and m_p is the effective polariton mass. This appendix provides connection between the current thesis and multidimensional spectroscopic techniques formulated by [10] using the density matrix formulation. Eqn B.43 provides as an initial distribution of polariton density matrix at thermal equilibrium.